

PDF hosted at the Radboud Repository of the Radboud University Nijmegen

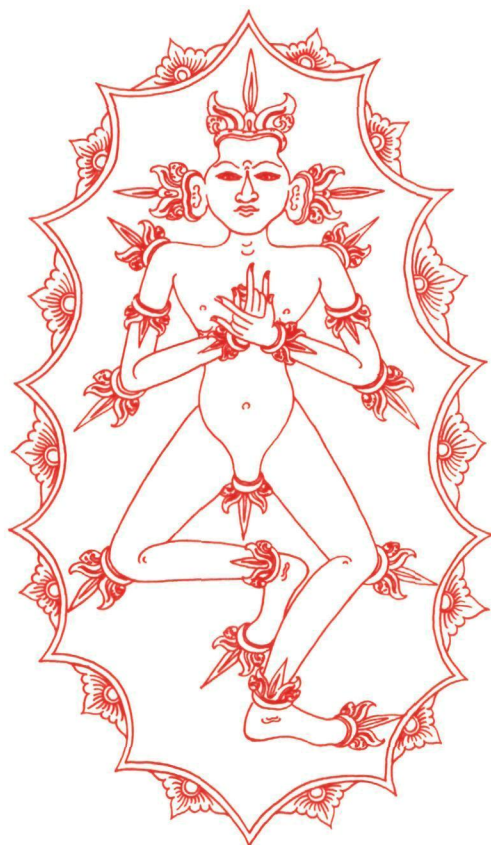
The following full text is a publisher's version.

For additional information about this publication click this link.

<http://hdl.handle.net/2066/114123>

Please be advised that this information was generated on 2017-03-14 and may be subject to change.

COMBUSTION DIAGNOSTICS
AT ATMOSPHERIC PRESSURES
USING A TUNABLE EXCIMER LASER



Michel Versluis

**COMBUSTION DIAGNOSTICS
AT ATMOSPHERIC PRESSURES
USING A TUNABLE EXCIMER LASER**

Cover : Symbolic male figure with flames emanating from his body, represents Sanghyang Widi, the supreme being. This figure is carved on top of many Balinese temple shrines and appears on an endless variety of magic amulets

**COMBUSTION DIAGNOSTICS
AT ATMOSPHERIC PRESSURES
USING A TUNABLE EXCIMER LASER**

een wetenschappelijke proeve op het gebied van
de Natuurwetenschappen

PROEFSCHRIFT

ter verkrijging van de graad van doctor
aan de Katholieke Universiteit Nijmegen,
volgens besluit van het College van Decanen
in het openbaar te verdedigen
op maandag 28 september 1992,
des namiddags te 3.30 uur precies

door

ANDREAS MICHAEL VERSLUIS

geboren op 6 september 1963
te Nieuwer Amstel

Promotor : Prof. Dr. J. Reuss

Copromotores : Dr. J.J. ter Meulen
Dr. W.L. Meerts
Dr. G. Meijer

'Improvisation is more important than knowledge'

Albert Einstein

Dankwoord

Dit proefschrift sluit een enorm plezierige tijd op de afdeling Molecuul- en Laserfysica van de Katholieke Universiteit Nijmegen af. Alle medewerkers van deze afdeling wil ik daar dan ook hartelijk voor bedanken.

Door Peter Verhoeve ingewijd in de geheimen van lasers en moleculen in het ver infrarood, ervoer ik de eerste sensaties van de experimentele fysica. Graag bedank ik ook mijn promotor, Jorg Reuss, voor zijn fijnzinnige begeleiding in, vooral, het mentale vlak. Hans ter Meulen, uitstekend docent, al vanaf mijn eerste jaren in Nijmegen, en Leo Meerts, een onmisbaar manager en een computer communicatie specialist bij uitstek, hebben een belangrijk aandeel gehad in de realisering van dit project. Gerard Meijer, in de eerste jaren al vanuit Californie coach-end, eenmaal in Nijmegen niet te stuiten in werklust, enthousiasme en eigenwijsheid, heeft me de laatste twee jaar de juiste weg gewezen. Ik wil Dave Parker bedanken voor de vele discussies over tralies en voor het kritisch doorlezen van vele manuscripten.

In de afgelopen vier jaar van wetenschappelijk onderzoek werd ik bijgestaan door drie leergierige jonge honden. Giel Berden, Maarten Boogaarts en Robert Klein-Douwel hebben een belangrijke steen bijgedragen aan dit proefschrift. Het tijdig afronden van Giel's afstudeerverslag verdient een extra compliment.

Geen experimentele opstelling werkt zonder technici en electronici. John Holtkamp, Frans van Rijn, Eugène van Leeuwen en Cor Sikkens verdienen een grote pluim voor hun bijdragen aan het vlammenproject. De quick-service, de glasblazerij en de grote werkplaats bedank ik voor vele spoedklussen die ingeroosterd konden worden. De afdeling Illustratie en Fotografie hebben een belangrijk aandeel gehad in het tot stand komen van de figuren in dit proefschrift. Het tandem Derksen/Kasman is ongekend en onmisbaar voor experimentele fysici. Ferry, voor alle moeite heel erg bedankt en bapak Rob, saya mengucapkan banyak² terima kasih dan mudah²an sampai ketemu kembali.

Van de KEMA bedank ik graag Ad Braam en Wiggert de Jongh voor het succesvol verlopen van ons gezamenlijk project aan de grote gasvlam. Ik bewonder de inzet van Bert Thus. Philip de Goey en René Quax van de TU Eindhoven wil ik bedanken voor hun bijdragen in de eindfase van dit project. Jaap Hoornstra van de ECN heb ik leren kennen als een nieuwsgierig man. Met plezier heb ik samen met hem gewerkt.

Viel habe ich gelernt von Peter Andresen und seinen Mitarbeitern. Die guten Zeiten im Max Planck Institut für Stromungsforschung und im Laser Laboratorium Gottingen werde ich nicht leicht vergessen.

Huize Acacia is niet meer, maar de gedachten leven voort Het was een voorrecht er te wonen
Een onmisbare afwisseling voor lasers en vlammen

Zelfs mijn ouders en mijn zussen hebben op hun wijze bijgedragen aan verbrandingsonderzoek met afstembare excimeer lasers José, de grootste vlam in mijn leven, is een onmisbare schakel geweest in het tot stand komen van dit proefschrift

Dit onderzoek maakt onderdeel uit van het research programma van de Stichting voor Fundamenteel onderzoek der Materie (FOM) en wordt gesteund door de Stichting voor de Technische Wetenschappen (STW) welke tot doel heeft technisch-wetenschappelijk onderzoek en de toepassing daarvan te bevorderen FOM en STW zijn onderdeel van de Nederlandse Organisatie voor Wetenschappelijk Onderzoek (NWO), welke dit onderzoek door financiële steun mogelijk heeft gemaakt

Contents

1	Laser-based combustion diagnostics, an introduction	11
1 1	Emission spectroscopy and intrusive techniques	12
1 2	Laser-based techniques	14
1 2 1	Scattering techniques	14
1 2 2	Coherent Anti Stokes Raman Scattering	16
1 2 3	Laser-Induced Fluorescence	17
1 2 4	Degenerate Four Wave Mixing Techniques	17
1 3	Laser-induced fluorescence	20
1 3 1	Rate equations	21
1 3 2	Laser induced fluorescence in the high density limit	23
1 3 3	Temperature measurements via laser induced fluorescence	25
1 4	Outline	26
2	Diagnostics with a tunable excimer laser	29
2 1	General	30
2 2	Experimental setup	32
2 2 1	Tunable excimer laser system	32
2 2 2	Laser beam transportation and sheet construction	38
2 2 3	Fluorescence detection systems	39
2 2 4	Burner systems	49
2 3	The molecular spectroscopy of transient combustion species studied with a tunable ArF and KrF excimer laser	52
2 4	Temperature determinations via OH LIPF	59
2 4 1	Required information	60
2 4 2	Rotational-level dependent predissociation	62
2 4 3	Comparison of predissociation rates	64
3	Frequency calibration in the ArF laser tuning range using laser-induced fluorescence of NO	67
3 1	Introduction	68
3 2	Experimental Setup	69
3 3	Results and Discussion	72
3 4	Summary	74

4	Intra-cavity C atom absorption in the ArF laser tuning range	79
5	Laser-induced fluorescence imaging in a 100 kW natural gas flame	83
5 1	Introduction	84
5 2	Experimental Setup	86
5 2 1	100 kW burner	86
5 2 2	Laser system	86
5 2 3	Calibration flame	88
5 2 4	Detection system	88
5 2 5	Triggering	88
5 3	Results	89
5 3 1	Small scale burner experiments	89
5 3 2	100 kW burner experiments	92
5 4	Summary	96
6	Degenerate four-wave mixing with a tunable excimer laser to detect combustion gases	97
6 1	Introduction	98
6 2	DFWM in forward geometry	98
6 3	Experimental	100
6 4	Results and Discussions	101
6 4 1	Molecular spectra	101
6 4 2	DFWM-FG pressure dependence	101
6 4 3	DFWM-FG laser power dependence	106
6 4 4	Application to combustion environments	107
6 5	Summary	107
7	Future outlook	109
	References	111
	Samenvatting	119
	Curriculum Vitae	121
	Publications	123

Chapter 1

Laser-based combustion diagnostics; an introduction

Various old and new techniques used in combustion diagnostics are discussed as an introduction to more detailed studies embodied in this thesis. In particular, pulsed laser-based techniques and their major advantages and drawbacks are summarized. The laser-induced fluorescence technique is treated in more detail. Laser-induced fluorescence at atmospheric pressures is discussed and basic considerations concerning temperature measurements are given. An outline of the thesis concludes Chapter 1.

Fire, and especially the striking of fire from flint stones, received great interest already from scientists in the prehistoric millennia. Flames and fires have always been worshipped for their devastating and at the same time impressive effects. Fire has disinfecting properties and supplies us with large amounts of heat energy. A flame is one of the best visible chemical processes where thousands of chemical reactions take place, shrouding the understanding of flames in mystery for so many time (and in a way still doing it). The scientific research of flames started in the medieval centuries with the rise of the mining industries and was dictated by an engineering point of view. Many centuries later, in the early 1900, flame research also covered atomic and molecular spectroscopy. The fundamental aspects of spectrometric studies was emphasized and flames were used mainly since they are excellent producers of special molecules.

It is in the last two decades, after the awareness of diminishing fossil fuel supplies and possible pessimistic ecological scenarios, such as the environmental acidification and the greenhouse effect, that combustion diagnostics has received a new scientific impulse from both the fundamental and the applied field. The spectroscopy and dynamics of flame molecules are now used to understand the combustion process and chemical reaction models are developed to accurately model the flames and explosions. The models require quantitative information on species concentration, flame temperatures and flow velocities with a high spatial and temporal resolution. Several diagnostic techniques, measuring these parameters, have been developed over the years. Laser-based techniques are of particular interest as they have active control over the measured quantities and because of their non-intrusive properties. As an example, nowadays lasers allow the visualization of nitric oxide formation and fuel combustion in internal combustion engines [1], processes in the past mainly investigated by trial and error methods.

Laser-based techniques are used more and more in the diagnostics of combustion processes. Many different techniques exist and every technique has its own particular merits and demerits. This chapter summarizes some commonly used and also recently introduced techniques. Almost all techniques utilize the presence of molecules in flames. Consequently it is of utmost importance that the fundamental molecular spectroscopy and the fundamental molecular dynamics is studied in great detail.

1.1 Emission spectroscopy and intrusive techniques

Emission spectroscopy has been used to study combustion processes from as early as 1930 on [2]. In these experiments the light emitted by flames is dispersed by a prism or grating spectrometer and from the observed spectra information is obtained on the rotational, vibrational and electronic properties of the molecules from which these spectra originate. Combustion diagnostics using this technique is complicated for several reasons. The molecules might be produced into their excited state by complex chemical reactions. They undergo many collisions, which quench their fluorescence emission. The molecules experience dissociation processes and may not emit light at all. Moreover, mostly only specific radicals with a high transition dipole moment are observed.

This makes the combustion process very difficult to model

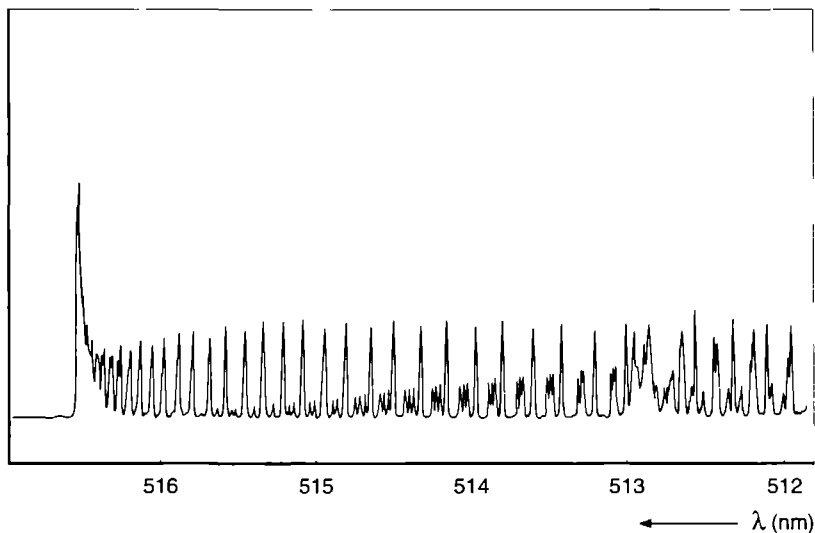


Figure 1.1 : The dispersed fluorescence emitted by C_2 molecules in a methane/air flame. The Swan-bands, with a band-head at 517 nm, were first recorded already in 1857.

Sodium atoms are added in some cases to study the absorption and emission processes in flames. With the so-called line-reversal method [3] temperature determinations are performed. This method requires a long sampling time, however, and structural information is lost usually. Moreover the sodium intrudes into the combustion process with unpredictable effects. Infrared radiation thermometry, or pyrometry, measures the absorption lines of e.g. CO_2 and H_2 vibrational transitions. Here problems arise how to determine the emissivity of the flame and to find a good frequency band-pass filter in front of the detector.

Probes can be inserted in flames. Thermo-couples are used to determine the temperature of the flue gas of the flame. The physical properties of thermo-couples have been studied for some time now. A thermo-couple consists of a thin platinum wire (diameter 75 - 200 μm) and are economical. The use of thermo-couples is limited, however, because of their melting temperatures (at maximum 1760 K for Pt/Rh wire). In the flame thermo-couples experience a net heat transfer and this affects the temperature measured. The thermo-couple radiates to the colder surroundings of the flame, and the flame in its turn has a strong heat convection toward the couple. Mantles around the flame more or less prevent this heat exchange. Suction

pyrometers solve the problem of heat transfer. Here, the flue gas is extracted from the flame via a small pipe, where a thermo-couple is installed. Suction pyrometers are more suited for larger type flames, because of their larger dimensions. A calibration curve is required for most types of suction pyrometers. The pyrometers have more fundamental problems, such as the catalytic reaction of flame radicals with the platinum (which can be coated) and the suction flux (should it be isokinetic or extremely fast).

Thermo-couples and suction pyrometers are inserted intrusively in the flames. The temperature measured is apparently different from the one measured without inserting a probe. The flow fields are changed and the flame is locally cooled.

1.2 Laser-based techniques

From the preceding section the need for non-intrusive techniques is evident. Lasers offer this non-intrusive property. With pulsed lasers the state distribution of the molecules is determined on a nanosecond time scale. For all laser techniques it is important to understand the fundamental spectroscopy of the molecules under investigation. In addition, every laser-based detection technique comes with a set of advantages, disadvantages, exceptions, warnings, inaccuracies, impossibilities, etcetera. The common techniques used in combustion diagnostics will be discussed below.

1.2.1 Scattering techniques

One of the first things observed when passing a laser beam through a flame is the elastic scattering of the laser light. Scattering occurs off single gas-phase molecules and off soot particles or fuel droplets. When the diameter of the scattering particle is small compared to the laser wavelength the term Rayleigh scattering is used. Scattering of larger particles is called Mie scattering. Rayleigh and Mie scattered laser light have the same wavelength as the incident light. Light can also scatter off at a different wavelength. This scattering process is called Raman scattering. A frequency shift, corresponding to an energy separation in the ground state of the molecules, is observed. Raman scattering is an intrinsically weak scattering process, but once stimulated (by Stimulated Raman Scattering (SRS) [see section 2.2.1] or by Coherent Anti-Stokes Raman Scattering (CARS) [see section 1.2.2]) the signals can become very strong. Applications of Rayleigh and Raman scattering in combustion diagnostics are briefly discussed below.

Rayleigh Scattering Techniques

Rayleigh scattering is used to quantitatively determine the temperature distribution in a flame. The observed signal is directly proportional to the density of the scattering species. Rayleigh scattering is also proportional to the effective differential Rayleigh cross section, which is calculated directly from the molecular gas composition in the area of interest and the individual

molecular differential Rayleigh cross sections of the major combustion species. The Rayleigh cross section has a $1/\lambda^4$ wavelength dependence, which makes the deep UV excimer lasers very well suited for Rayleigh scattering imaging if compared with visible pulsed lasers. Moreover, the polarization inducing the scattering effect grows with decreasing wavelengths for most major combustion species. When applying this technique, flames must be soot- and droplet-free. Then, the observed scattering signal is proportional to the total molecular density. When dealing with premixed open air flames, where the pressure is 1 bar over the entire flow field, the temperature distribution is calculated using the ideal gas law. As a reference the temperature is calibrated using the Rayleigh scattering signal from room temperature air on the sides of the flame. In diffusion flames the distribution of unburned hydrocarbons is visualized, because of their very high Rayleigh cross section. Temperature distributions are not calculated in these flames because of the lack of the molecular species concentration information.

Rayleigh scattering, and also Raman scattering, is not subject to saturation effects. Ten times more laser light induces ten times more scattering light. This makes the experimental data easier to interpret compared to other laser-based diagnostic techniques such as CARS and LIF. The Rayleigh scattering technique has many problems with stray light rejection, however. Another serious problem is induced fluorescence. With the narrow-band excimer laser this problem is avoided. The tunable KrF excimer laser is used in most cases, because of its high power and relatively small number of fluorescence lines within its gain profile. The tunable ArF excimer laser has smaller problems with diffuse stray light. A detailed description of the application of Rayleigh scattering with tunable excimer lasers in flames is found in ref [4].

Spontaneous Raman Scattering

Spontaneous Raman scattering is a very interesting diagnostic technique for combustion processes. It offers the possibility to measure the temperature and all major species concentrations simultaneously. The technique has an easy approach, since the signals are directly proportional to the number density of the probed species and consequently the concentrations can be calibrated in a straightforward manner. Moreover, the costs of the experimental equipment needed for a spontaneous Raman scattering setup are relatively low. Spontaneous Raman scattering is of special interest when short wavelengths are available. Raman scattering has the same λ^{-4} wavelength dependence as the Rayleigh scattering described above. In addition, the Raman scattering cross section is increased further, for molecules which absorb in the near UV, by resonant enhancement.

Spontaneous Raman scattering with broadband excimer lasers has been used for some time. In the UV studies, particularly, the laser-induced fluorescence interferences complicated the identification of the spectra, due to the lack of spectral resolution. To minimize the LIF interferences and to improve the spectral resolution, a narrowband KrF laser is used. The KrF laser, with OH and O₂ resonances in its gain profile, is tuned to a region where no absorptions occur.

Shirley [5] measures H_2 and H_2O Raman spectra, of interest in the exhaust in rocket engines (specifically at the exit plane of the space shuttle main engine), successfully with little LIF interferences. Densities are detected quantitatively with a 7 % uncertainty. A higher injection locking efficiency of the tunable excimer, decreasing the few percent of broadband laser output inducing the interfering fluorescence, would improve the selectivity. Cheng et al. [6], on the other hand, uses the very thing of broadband emission to excite OH in their supersonic flames and measures the Raman spectrum simultaneously. An extensive study of their experiments on spontaneous Raman scattering in combination with LIF of OH with a narrowband KrF excimer laser is described in detail in ref [6].

1.2.2 Coherent Anti-Stokes Raman Scattering

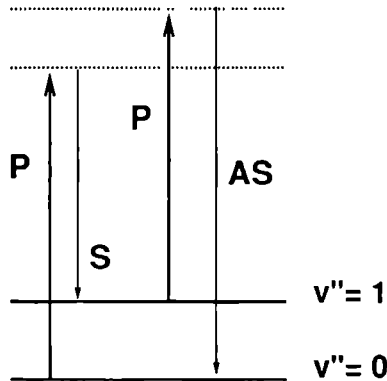


Figure 1.2 : The principle of Coherent Anti-Stokes Raman Scattering.
P = pump beam, S = Stokes beam, AS = Anti-Stokes (CARS) beam

Spontaneous Raman scattering, though its experimental simplicity, is outvied by a non-linear Raman technique which delivers much larger signal strengths and instantaneous sampling times. The technique of Coherent Anti-Stokes Raman Scattering (CARS) [7] enhances the blue scattered Raman signal by several orders of magnitude. The CARS technique combines high spectral resolution, time and spatial resolution and allows studies in media difficult to access [8]. In the CARS technique (see fig. 1.2) the Stokes scattered signal of the pump beam with frequency ω_p is stimulated by a coherent laser beam with frequency ω_s . A second scattering process of again the

pump beam from the vibrationally excited level generates, through a non-linear four-wave mixing process of the three incoming beams, a coherent Anti-Stokes signal beam with a frequency ω_{as} . The CARS technique is most powerful in N_2 thermometry. CARS signals of minority species are very weak when compared with fluorescence techniques. CARS is used in many varieties of pump geometries and detection schemes with broadband and/or pure rotational versions, summarized in ref. [9]. The CARS technique is rather complicated in its experimental setup and in particular in its signal interpretation. Special computer codes, containing saturation effects and frequency shift compensations, are used to interpret the observed scattering signals. The CARS signal depends quadratically on the probed state distribution and sometimes suffers from a disturbing non-resonant background which influences the temperatures calculated. Nonetheless, CARS, up to now and under very special conditions, offers the possibility for quantitative single-shot single-point temperature measurements via N_2 Anti-Stokes Raman scattering.

1.2.3 Laser-Induced Fluorescence

Laser-induced fluorescence (LIF) is an attractive alternative to CARS for its experimental simplicity. Molecules are electronically excited by the narrowband laser and the induced fluorescence has a linear correlation with the density of the molecules in the initial ground state. LIF is monitored perpendicular to the laser beam. It can also be monitored in two dimensional planes. Section 1.3 treats the LIF technique in more detail.

1.2.4 Degenerate Four-Wave Mixing Techniques

Four-wave mixing is a non-linear process where three coherent beams interact in a dispersive medium forming a fourth coherent signal beam. Four-wave mixing is among others used for the generation of VUV radiation and for spectroscopic detection [10]. The best known four-wave mixing process is CARS, discussed above. The signal is increased by several orders of magnitude when the three (and automatically four) beams are degenerate in frequency. This technique is called degenerate four-wave mixing and will be discussed below.

Degenerate Four-Wave Mixing

The technique of degenerate four-wave mixing (DFWM) is a form of optical phase conjugation. It was discovered just recently that this technique could be applied to molecular gas-phase absorption spectroscopy. DFWM is best explained in its so-called grating picture. Two parallel or counter-propagating coherent beams are crossed having a small crossing angle. Interference of the two beams creates an oscillating pattern of ventral segments and nodes. When the beams are tuned to an absorption line of the molecule under investigation a spatial distribution of ground state and excited state molecules is formed, a grating. To illustrate this make a transparent copy of the adjacent page or use the transparency supplied with this thesis and cover the wave fronts

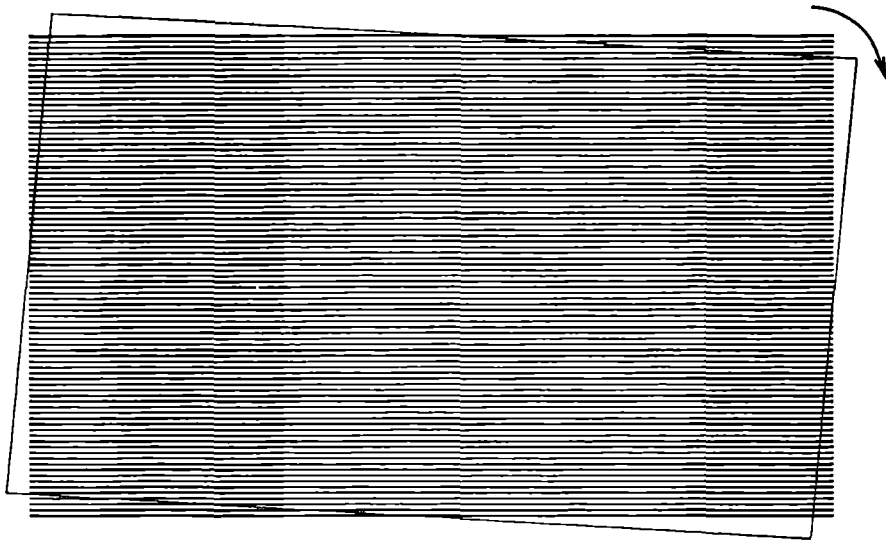


Figure 1.3 Wave fronts of a coherent laser beam. Rotate the transparency as indicated to form a grating.

drawn in fig. 1.3. Now rotate the transparency as indicated and watch the grating being formed. Note that a larger angle indeed increases the groove spacing. A third coherent laser beam can be Bragg scattered off the grating. The grating, and consequently the scattered beam, is only present when a molecular absorption occurs and therefore the signal beam reflects the absorption spectrum of the molecules absorbing in the focal point or plane.

DFWM is a very sensitive technique. The signal comes out as a coherent beam and consequently remote detection can be performed. The signal beam is passed through narrow pinholes and straylight problems are drastically reduced. DFWM requires very low laser intensities, typically μ Joules, in order to work. DFWM is used in different configurations. The phase-conjugate DFWM and the DFWM in forward geometry will be discussed in more detail below.

Phase conjugate DFWM

In the phase conjugate DFWM setup (see fig. 1.4) the grating is set up by two counter-propagating beams. The probe beam can be incident under an arbitrary angle, because the phase-matching condition for four-wave mixing is fulfilled for all angles. The signal beam is phase conjugate with the probe beam. The four-wave mixing in the phase conjugate setup is an instantaneous process. Only very few velocity groups in the probe region are used to form the signal beam. The phase conjugate DFWM is indeed a sub-Doppler and collision-free technique. Because low laser intensities are required the grating-forming laser beams can be transformed

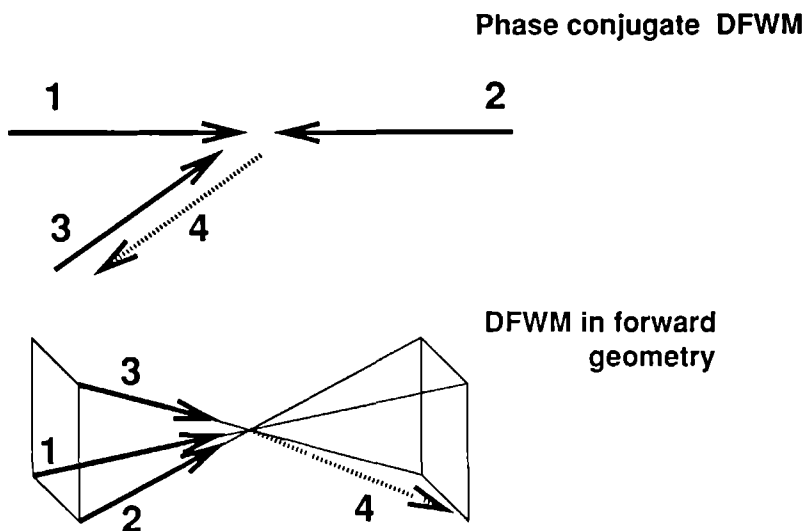


*Figure 14 Degenerate Four Wave Mixing (DFWM) in two configurations
Top Phase conjugate DFWM Bottom DFWM in forward geometry*

into a sheet allowing two dimensional DFWM with a high temporal and spatial resolution. The probe beam is widened to a large circular beam and the phase conjugate signal beam is monitored with an unintensified CCD camera.

Important future applications of the phase conjugate DFWM technique probably lies in the infrared region of the spectrum [11], probing molecular vibrational transitions. Molecules such as CH, CH₄ and CO₂, so far difficult to observe in fluorescence and ionization, can be visualized with coherent single-mode infrared sources, such as opto-parametric oscillators (OPO's).

A problem complicating DFWM in complex gas mixtures such as flames, is the fact that all absorbing molecules are detected. Especially at higher frequencies the molecular spectra become more and more congested. Too high laser powers should be avoided because of a non-resonant background which is not observed at low laser powers. Beam steering destroys the DFWM signals in media with large pressure gradients. The latter problem is overcome when phase conjugate mirrors are used for the beams generating the grating.

Degenerate Four-Wave Mixing in forward geometry

The schematic configuration for DFWM in forward geometry is also indicated in fig 1 4 Two of the three beams set up a grating which in its turn is probed by the third The angle between the beams is chosen such that the Bragg condition (or phase matching condition) is fulfilled DFWM in forward geometry has been used for a decade now to study molecules in the solid state and liquid phase Recently the technique has been applied to gas phase molecules Different experimental setup can be used An easy and direct way of performing DFWM in forward geometry is to use a mask in the beam profile and to focus the three beams with a single lens [12] The beams can also be combined with prisms and optical delay lines This setup allows temporal dependence experiments DFWM in forward geometry has been applied to combustion processes by Fayer et al [13] We have studied several combustion species using DFWM in forward geometry with a tunable excimer laser Chapter 6 treats the DFWM technique in forward geometry in more detail

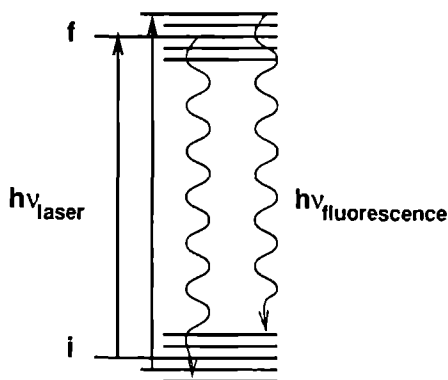


Figure 1 5 Laser-induced fluorescence

1.3 Laser-induced fluorescence

The laser-induced fluorescence (LIF) technique is a widespread sensitive diagnostic technique It is a method to quantitatively measure single quantum state distributions at low densities

Laser-induced fluorescence is a two step process holding generally the following equation

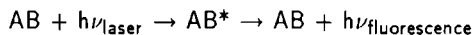


Figure 1.5 shows the basic concept of the laser-induced fluorescence technique. A molecule is excited by a laser photon with an energy $h\nu_{\text{laser}}$ from an initial state i , with a density n_i , to an electronically excited state f , with a density n_f . The induced fluorescence intensity F is proportional to the density of state i , $F \propto n_i$. When tuning the laser in frequency an LIF spectrum is measured. Molecules in different rotational states absorb laser photons at different frequencies, yielding different fluorescence intensities. From this the total state distribution, i.e. the relative population density in the different vibrational and rotational states, of the specific molecule is determined. The laser induced fluorescence is emitted to different energy levels lying below the excited level. A variety of frequencies is therefore observed. It is for this reason that the sensitivity of the laser-induced fluorescence technique is increased even more, because the fluorescence can be observed away from the laser line against a zero background level. An important advantage of the laser-induced fluorescence technique is its application in two-dimensional imaging. The laser beam is transformed into a thin sheet of laser light and fluorescence is observed from the region where the sheet intersects the flame. The fluorescence is imaged onto an image intensifier and two-dimensional maps of the molecule under investigation are collected digitally.

The LIF technique is used in many applications, such as in fundamental molecular beam spectroscopy of cold radicals and their van der Waals complexes, in crossed beam collision dynamics studies yielding information on the integral state-to-state collision cross sections, in photodissociation dynamics probing the dissociation product state distribution and in recent years also in combustion diagnostics to analyze the gas composition and temperature. Laser-induced fluorescence is also used to monitor the turbulent explosion in an internal combustion engine and to study the temperature distributions occurring during the re-entry of space shuttles into the atmosphere.

1.3.1 Rate equations

The laser-induced fluorescence technique works well in the low laser power and low density regime, in the so-called linear limit. However, at atmospheric pressures and at higher laser powers, deviations are found of the linear correspondence between the fluorescence and the state distribution of the state from which the molecule is excited. Laser-induced fluorescence can be very well modelled by the rate equations. It gives a quantitative description of the absorption and emission processes. In figure 1.6 a rate equation model is shown. Here, σI represents the rate for absorption and stimulated emission. A represents the rate for spontaneous emission and L is the sum of the rates of all losses in the excited state. The spontaneous emission to the same initial state has been ignored in this model. L contains, among others, the rates for collisional

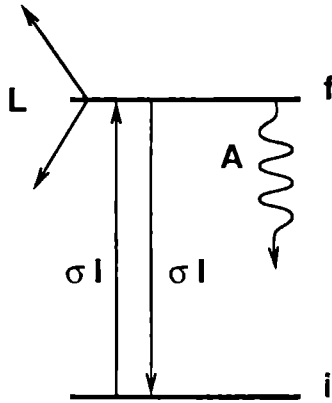


Figure 1.6 · The different rates when applying the laser-induced fluorescence technique.

quenching, predissociation and ionization The rate equation model supplies us with two coupled homogeneous linear equations

$$\frac{dn_f}{dt} = \sigma I n_i - \sigma I n_f - A n_f - L n_f \quad (1.1)$$

$$\frac{dn_i}{dt} = \sigma I n_f - \sigma I n_i \quad (1.2)$$

The rate equations are solved to give n_i and n_f as a function of time The total emitted fluorescence is given by the integral over time of the spontaneous emission rate times the population in the excited level f

$$F = \int_0^{\infty} A \cdot n_f(t) dt \quad (1.3)$$

assuming the excitation started at $t=0$ Some simple calculations show that in the linear limit ($\sigma I < A + L$) the fluorescence obeys the following expression

$$F \propto \frac{A}{A + L} \cdot n_i \quad (1.4)$$

The proportionality factors depend mainly on the intensity and the bandwidth of the laser At low densities, where no collisions take place during the radiative lifetime of the excited state

($L < A$), a known density n , in a cell e.g., calibrates this constant. It must be noted that this procedure is a little more complicated for atoms and radicals than it is for stable molecules, which are easily contained in a calibration cell. The ratio $A/(A+L)$ is called the Stern-Vollmer factor.

1.3.2 Laser-induced fluorescence in the high density limit

As we have seen in the previous section LIF is a quantitative diagnostic technique when applied to experiments at low density. The Stern-Vollmer factor is constant and independent of collisions and the fluorescence is directly proportional to the density of the probed state. At higher pressures collisions are introduced in the fluorescence process. Electronically excited molecules lose their energy in collisions, ionize or react with other species. The collisional quenching rate Q , and consequently the Stern-Vollmer factor $A/(A+Q)$, is very difficult to quantify. It depends on the density of all collision partners, their collisional cross-section and also on the surrounding temperature. For a complicated gas composition the total quenching rate of the laser-excited molecules is the sum over the individual quenching rates times the corresponding state distribution of the quenching species. In an internal combustion engine, for example, the quenching rate has an extreme space and time dependence of the density (of more than 25 different species) and temperatures. Here, neither rate constants nor densities nor temperatures are known. Quenching is, to conclude, an elusive loss channel, which one would like to get around.

Fortunately, some alternatives are available. The quenching can be eliminated if other loss channels are larger. An example of such a case is the one where a strong predissociation of the molecule under investigation dominates all other loss channels. The Stern-Vollmer factor $A/(A+Q+P)$, with P the predissociation rate, is approximately A/P . The fluorescence is determined by molecular parameters only and is independent of the object under investigation. If the predissociation rate is known, quantitative density measurements are possible. The predissociation process can be very fast. It must be noted that one single molecule either predissociates or fluoresces. The fluorescence occurs only during the predissociation lifetime, which is typically in the sub-nanoseconds range. In this time the excited molecule does not experience collisions. Despite the large loss in fluorescence, the method, called laser-induced predissociative fluorescence (LIPF), is still very sensitive. More important however, it offers the possibility for collision-free spectroscopy at atmospheric pressures.

The high density limit is best explained with the $A^2\Sigma^+ \leftarrow X^2\Pi$ transition of the OH radical as an example. In figure 1.7 an energy diagram is shown for two cases of OH excitation. On the left-hand side of figure 1.7 the conventional $0 \leftarrow 0$ transition is excited at 308 nm. On the right-hand side OH molecules are excited via the $3 \leftarrow 0$ transition at 248 nm. The fluorescence lifetime of the electronically excited state is approximately $1 \mu\text{s}$ ($A = 10^6 \text{ s}^{-1}$). The $v'=0$ level is far off the curve crossing with the repulsive states responsible for the predissociation in the

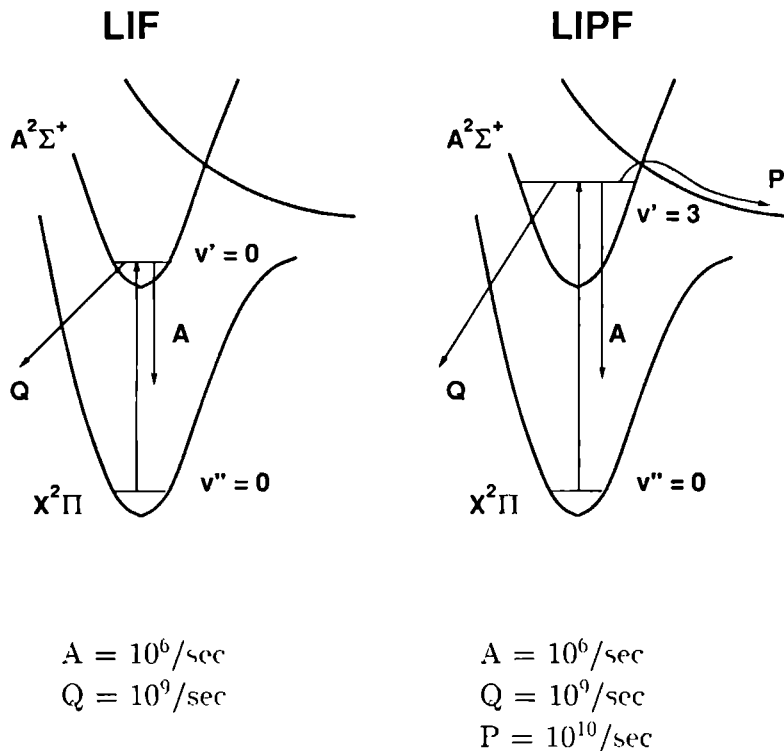


Figure 17 The OH radical excited via the LIF and the LIPF technique

$A^2\Sigma^+$ state. The transition is rather weak and since the predissociation is absent, the quenching rate dominates the fluorescence observed, so that not only a loss of 10^3 in fluorescence photons is observed but also the state distributions can not be determined quantitatively.

When OH is excited via the $3 \leftarrow 0$ transition at 248 nm a strong predissociation loss channel is introduced. The predissociation lifetime is of the order of 100 ps ($P = 10^{10} \text{ s}^{-1}$), an order of magnitude larger than the collisional quenching rate at atmospheric pressures ($Q = 10^9 \text{ s}^{-1}$). The Stern-Vollmer factor is determined by parameters of the molecule under investigation only. The factor reduces to 10^{-4} , but the intense KrF excimer laser compensates for this loss in sensitivity. When the predissociation rates for the different rotational lines in the electronically excited state are known, quantitative density and temperature determinations are possible. This is discussed in section 2.4 of the thesis.

The collisional quenching rate can be eliminated also by saturating the transition when we

deal with a clean two level system. Both the fluorescence and the quenching go back into the initial ground state level. Shortly after starting the saturating laser pulse the population of the initial state is divided over the ground and excited states. Molecules are pumped up and down by the laser photons. Because no losses are involved the density remains unchanged and the fluorescence is constant and independent of Q . A clean two level system is, for example, found when exciting Na atoms with a broad laser. In molecules, however, only a very small fraction of the fluorescence and the quenching goes back to the initial ground state. Both channels are clearly a loss and when the rate equations are solved for high laser powers ($\sigma I > A + Q$) the expression for the total emitted fluorescence still contains the Stern-Vollmer factor $A/(A+Q)$, which makes quantitative density measurements as difficult as in the linear limit setup.

1.3.3 Temperature measurements via laser-induced fluorescence

The density in a given quantum state n_l in thermal equilibrium is given by the Boltzmann distribution

$$n_l = n \quad f_l = n \quad (2J_l + 1) \quad \frac{\epsilon \tau p \left(\frac{-E_l}{kT} \right)}{Z} \quad (1.5)$$

f_l is the fractional population in the ground state of the molecule. Z is the sum over all different fractional populations

$$Z = \sum_m (2J_m + 1) \quad \epsilon \tau p \left(\frac{-E_m}{kT} \right) \quad (1.6)$$

The temperature is calculated from the ratio n_1/n_2 of the densities of two ground state levels using the equation above. Some simple algebra shows

$$T = \frac{\Delta E}{k \ln \left(\frac{2J_1 + 1}{2J_2 + 1} \frac{n_2}{n_1} \right)} \quad (1.7)$$

Here, ΔE is the energy difference $E_2 - E_1$ in the ground state of the molecule. k is the Boltzmann constant. The temperature is thus calculated from the relative population of the ground state levels, which in turn is calculated from the relative fluorescence signals with the appropriate calibration factors (laser power, line intensities, predissociation rates, etc.). In section 2.4 we use the above equations to calculate temperatures for an adiabatic methane/air flame.

We conclude this section with a remark on the accuracies obtained when applying laser-induced fluorescence diagnostics techniques to temperature measurements. With the first derivative of R , the ratio n_1/n_2 , and with equation 1.1, we find for the error in the temperature T

$$\frac{\Delta T}{T} = \frac{k \Gamma}{\Delta E} \quad \frac{\Delta R}{R} \quad (1.8)$$

The relative uncertainty in the calculated temperature is determined by the relative uncertainty $\Delta R/R$ of the density ratio, or actually of the fluorescence signals and their calibration factors. A small energy difference ΔE introduces large errors. Therefore, the rotational lines must be chosen in such a way that their ground state levels lie apart at a reasonably far energy distance. The errors increase with increasing temperatures. The measurement has to be much more accurate at higher temperatures when a fixed error is required over a reasonably large temperature range. As an example the hydroxyl radical again, excited by the KrF excimer laser at 248 nm. The $R_1(15)$ and $P_1(8)$ rotational lines are used, which have a ground state energy separation of approximately 3000 cm^{-1} . At a temperature of 2000 K this corresponds to an uncertainty of 100 K in the absolute temperature when a 10 % uncertainty in the ratio R is assumed. The accuracy in the temperature measurement is improved by taking more rotational lines.

A final word on the quenching problems. For temperature measurements, since only the density ratio R is needed, quenching is a smaller problem compared to density measurements, because only the difference in quenching is important. Quenching problems are completely eliminated in temperature determinations when the molecules are excited to the same upper level from different ground state levels. Molecules can be excited via a pair of P and R rotational lines. The ground state levels lie very closely together, however, resulting in a low temperature accuracy. The rotational lines can be chosen to start from different vibrational states and to end at the same upper level in the electronically excited state with consequently a large energy separation ΔE between the probed energy levels. It is, however, by no means clear that the vibrational energy distribution is thermal and can be used to determine temperatures. Quenching problems remain very difficult to eliminate.

1.4 Outline

Following the introduction on laser-based diagnostic techniques in combustion in this chapter, we continue with a description of the molecular spectroscopy of combustion species studied with a tunable ArF and KrF excimer laser (Chapter 2), prefaced with a description of the regular experimental setup. Here, the tunable excimer laser and the 2-D imaging system are explained in detail. Chapter 2 is concluded with a description how to quantitatively measure temperatures and densities using the LIPF technique. It treats the problems of rotational level dependent predissociation of the electronically excited OH radicals and the fast energy redistribution in the ground state at atmospheric pressures. Section 2.4 deals with the problems still to solve in the future.

Chapter 3 describes the frequency calibration in the ArF laser tuning range using laser-induced fluorescence of nitric oxide. The calibration spectrum is measured with a frequency doubled and Raman-shifted dye laser system and with the tunable ArF excimer laser. This chapter gives a nice example of the use of the excimer laser in the amplified oscillator mode, described in section

2.2.1 . Chapter 4 describes the occurrence of an intra-cavity absorption, caused by metastable carbon atoms in the discharge of the ArF excimer laser. The absorption causes a lack of tunable and narrowband laser radiation over a region of 5 to 10 cm^{-1} . The intra-cavity absorption has a direct consequence for the interpretation of the photodissociation dynamics of carbon monoxide at 193 nm.

The previous chapters are mainly focussed on the fundamental aspects of spectroscopy. A direct application-oriented experiment is presented in Chapter 5, where we have studied the flame of a 100 kW natural gas burner. We have determined NO and OH field distributions in a flame with a diameter of 40 cm and with a length of nearly two meters. The problems encountered with the use of the VUV radiation of the ArF laser in the hot surroundings of the flame are described. The images obtained in this flame show the turbulent character of the combustion process and show that care has to be taken when interpreting any kind of temperature measurements in these type of flames.

In Chapter 6 degenerate four-wave mixing technique with a tunable excimer laser is applied to combustion gases. Several very weak (two-photon or spin-forbidden) transitions are measured with the DFWM technique in forward geometry with a very high sensitivity. Many spectra are measured with an ordinary photo diode. The dependence of the DFWM signals on various experimental parameters, such as pressure and laser power, is determined. Finally, in Chapter 7 the outlook to the near future is described briefly. The progress in the development in the field of, especially CCD-chips and electronic cameras, is enormous and some new designs will be discussed as a final remark of this thesis.

Chapter 2

Diagnostics with a tunable excimer laser

A detailed description of the experimental setup for two-dimensional laser-induced fluorescence imaging with a tunable excimer laser is given. The tunable ArF and KrF excimer laser is discussed in detail and special modifications for spectroscopic applications are reported. The burners used in our studies are described. The molecular spectroscopy of combustion species studied with the tunable excimer laser is summarized. The chapter ends up with a discussion of how to determine temperatures and densities via laser-induced predissociative fluorescence of the OH radical. Rotational level dependent predissociation and other structural problems are discussed.

2.1 General

Since their invention in the seventies, excimer lasers have been used for many applications and spectroscopic studies in the UV and VUV spectral region. The ArF and F₂ laser are used in ionization experiments because of their high energy photons of 6.4 and 7.9 eV, respectively. The XeCl and KrF excimer lasers are used to pump UV dye lasers directly (without the need for frequency-doubling) and with a high repetition rate. Many studies involve the XeF excimer laser for its picosecond Fourier-limited pulses.

A new class of experiments with excimer lasers started in the early eighties with line-narrowed excimers (primarily developed for lithographic purposes) and later continuously tunable excimer lasers. The first spectroscopic studies of room temperature O₂ [14] and H₂ [15] were soon followed by new two-photon excitation spectra of H₂O [16] and flame studies of OH [17] and hot O₂ [17, 18], all experiments done with the spectral bright tunable excimer lasers. The linewidth decreased and the spectroscopic properties of the laser improved after some years of tinkering. The initial oscillator setup with mirrors and seven beam expanding prisms was replaced by a grating-based setup where three prisms are now commonly used. An improved discharge cavity design concerned particularly the tunable ArF laser, resulting in new flame and cell spectra of NO [19] and CO [20]. The tunable excimer lasers supply us still with new (SiF [21], HCN [22]) and uninterpreted (O₂⁺ [23]) spectra of a variety of molecules. Table 2.1, on the adjacent page, summarizes the molecules of importance in combustion identified so far with the use of tunable excimer (or their Raman shifted) laser light.

Spectroscopic studies with the tunable excimer laser involve laser-induced fluorescence (LIF), resonance enhanced multiphoton ionization (REMPI), degenerate four-wave mixing (DFWM) and Rayleigh and Raman scattering experiments. In this chapter the experimental setup for the detection of laser-induced fluorescence from flames with a tunable KrF and ArF excimer laser is treated. Special attention is given to two-dimensional imaging of fluorescence with highly-sensitive electronic cameras.

A schematic representation of an experimental setup for two-dimensional imaging of fluorescence is shown in figure 2.1. The setup shown here is the common one used in our laboratory. The different parts of the experimental setup will be discussed in section 2.2 below. First, the excimer laser will be treated, followed by a detailed description of the electronic camera detection system. Several burner systems will be discussed. Then, this chapter deals with the spectroscopy of the molecules listed in table 2.1. This chapter concludes with a discussion how to quantitatively determine temperatures using laser-induced predissociative fluorescence of the hydroxyl (OH) radical.

Molecule	Transition	Excitation	Reference
OH	$A^2\Sigma^+ (v'=0) \leftarrow X^2\Pi (v''=0)$	XeCl	[24]
	$A^2\Sigma^+ (v'=2) \leftarrow X^2\Pi (v''=0)$	KrF S(2)	[25]
	$A^2\Sigma^+ (v'=3) \leftarrow X^2\Pi (v''=0)$	KrF	[17]
NO	$A^2\Sigma^+ (v'=3) \leftarrow X^2\Pi (v''=0)$	ArF	[26]
	$B^2\Pi (v'=7) \leftarrow X^2\Pi (v''=0)$	ArF	[19]
	$D^2\Sigma^+ (v'=0) \leftarrow X^2\Pi (v''=1)$	ArF	[19]
O ₂	$B^3\Sigma_u^- (v'=4) \leftarrow X^3\Sigma_g^- (v''=0)$	ArF	[14]
	$B^3\Sigma_u^- (v'=7) \leftarrow X^3\Sigma_g^- (v''=1)$	ArF	[14]
	$B^3\Sigma_u^- (v'=10,11) \leftarrow X^3\Sigma_g^- (v''=2)$	ArF	[18]
	$B^3\Sigma_u^- (v'=5) \leftarrow X^3\Sigma_g^- (v''=3)$	ArF S(1)	[27]
	$B^3\Sigma_u^- (v'=14,15,16,17) \leftarrow X^3\Sigma_g^- (v''=3)$	ArF	[18]
	$B^3\Sigma_u^- (v'=7,8) \leftarrow X^3\Sigma_g^- (v''=4)$	ArF S(1)	[27]
	$B^3\Sigma_u^- (v'=0,1) \leftarrow X^3\Sigma_g^- (v''=6)$	KrF	[17]
	$B^3\Sigma_u^- (v'=2) \leftarrow X^3\Sigma_g^- (v''=7)$	KrF	[17]
CO	$a^3\Pi (v'=2) \leftarrow X^1\Sigma_g^+ (v''=0)$	ArF	[20]
	$B^1\Sigma_g^+ (v'=0) \leftarrow X^1\Sigma_g^+ (v''=0)$	ArF S(2)	[20]
H ₂ O	$\tilde{C}^1B_1 \leftarrow \tilde{X}^1A_1$	KrF	[28]
H ₂	$E, F^1\Sigma_g^+ (v'=6) \leftarrow X^1\Sigma_g^+ (v''=0)$	ArF	[15]

Table 2.1 : Combustion species detected with tunable excimer lasers.
S(i) = the *i*-th order Stokes Raman shifted excimer laser.

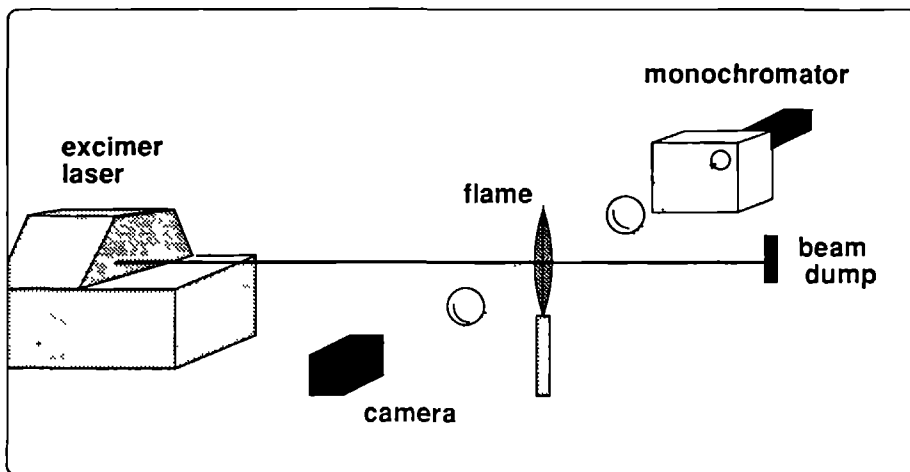


Figure 2.1 The standard experimental setup for laser-induced fluorescence imaging in flames with a tunable excimer laser. A high quality quartz objective usually replaces the lens in front of the camera.

2.2 Experimental setup

2.2.1 Tunable excimer laser system

Tunable excimer lasers are pulsed lasers with a high spectral brightness emitting laser light in the ultra-violet region. A pre-ionized rare gas/halogen gas sample contained between two parallel electrodes is discharged and excimers are formed by electron collisions. Excimers (excited dimers) are molecules that have a bound electronically excited state but have a dissociative ground state. Lasing action is possible since a population difference is automatically maintained as the lifetime of the bound state is much longer in comparison with the lifetime of the dissociative ground state. A typical potential curve for an excimer is given in figure 2.2. Examples of excimers are Kr_2^* , Ar_2^* and Xe_2^* .

Another class of excimers consists of heteronuclear excited complexes (exciplexes). Excited atoms having a closed electronic shell in the ground state, resemble alkali metal atoms. These excited atoms form strong ionic bonds with the halogens. Some known examples of these exciplexes are Ar^*F , Kr^*F , Xe^*Cl , Xe^*F and Kr^*Cl . Excimer lasers are very powerful pulsed lasers. They are often used as pump lasers for tunable dye lasers, because of their homogeneous energy distribution over the laser beam cross section and their high repetition rate. A XeCl

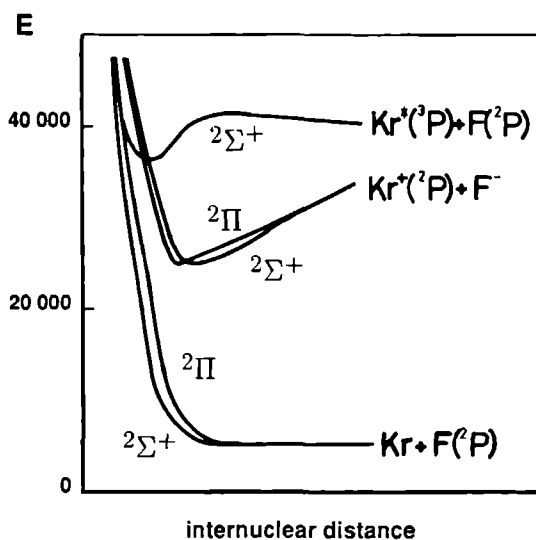


Figure 2.2 Potential curves for the valence and ionic states of Kr^*F

excimer laser, for instance, can deliver 3.0 Joule in a 15 ns pulse at a repetition rate of 40 Hz. Excimers emit radiation in a broad wavelength region, typically 1 nm. Because of their spectral broad laser emission excimer lasers are very well suited for the generation of femtosecond pulses. The green $\text{C} \leftarrow \text{A}$ lasing transition of the XeF laser (bandwidth 100 nm), for instance, has a Fourier limit of only 1 femtosecond. An injection seeded KrF laser (248 nm) delivers an output energy of 8 mJ in a 350 fs laser pulse. The excimer lasers can be frequency-narrowed and are tunable within their gain profiles. The tunable KrF excimer laser, for example, has a linewidth of 0.2 cm^{-1} . The spectral brightness of the tunable excimer laser, defined as the total energy/ $\text{cm}^2\text{cm}^{-1}$, exceeds that of conventional dye lasers by several orders of magnitude in this wavelength region. The most common tunable excimer lasers are the ArF (193 nm), KrF (248 nm) and XeCl (308 nm) excimer laser.

A schematic drawing of the tunable excimer laser is shown in figure 2.3. The laser is shown in its commercially delivered configuration. The laser consists of two discharge cavities, where one cavity acts as an oscillator and the other cavity acts as an amplifier. A discharge between two electrodes is ignited in the oscillator cavity containing a pre-ionized gas mixture of a rare gas ($\text{Ar}, \text{Kr}, \text{Xe}$), a halogen (F_2, Cl_2) and a buffer gas (He, Ne). The resonator of the oscillator cavity is set up by a reflection grating (Gr) and a partly reflective mirror (M1). The frequency selective

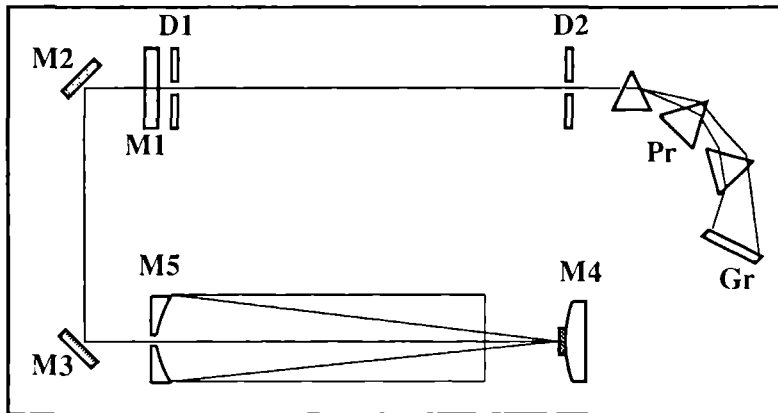


Figure 2.3 The tunable excimer laser in its commercially delivered setup

elements are the grating and an intra-cavity iris diaphragm (D1). Three prisms (Pr) expand the small laser beam to fully utilize the area of the grating. A second diaphragm (D2) helps to align the oscillator beam and does not affect the lasing action of the oscillator. The laser beam is dispersed by the grating and its reflection is projected on the iris diaphragm. By changing the angle of incidence at the grating (by tilting the grating with a micrometer screw) different parts of the laser spectrum can be selected and amplified. Mirror M1 transmits a part of the generated narrowband oscillator beam. Two coated aluminum mirrors (M2 and M3) direct the oscillator beam to the amplifier cavity. The amplifier cavity is equipped with unstable resonator optics. It consists of a convex 'meniscus' mirror (M4) and a concave fully reflective mirror (M5). This configuration is also called a Cassegrain resonator, since it resembles the astronomical Cassegrain telescope mount. The oscillator beam is injected into the amplifier cavity through a small hole in mirror M5. Mirror M4 has a special reflective coating in its center to reflect the narrowband oscillator beam. The oscillator beam is expanded and made parallel by the concave mirror. As the oscillator beam traverses through the amplifier cavity it locks the stimulated emission generated by the amplifier cavity discharge to the pre-selected oscillator frequency.

The mirrors M4 and M5 set up a cavity on their own. The amplifier cavity has broadband laser action when not injected by narrowband oscillator radiation. Even when the full power of the oscillator is pumped into the amplifier cavity, the laser output will contain a certain broadband underground. This underground increases with decreasing oscillator power. The ratio

laser		ArF	KrF
wavelength	[nm]	193	248
pulse energy (max)	[mJ]	100	250
averaged power (max)	[W]	8	20
bandwidth,FWHM	[cm^{-1}]	0.5	0.2
tuning range	[cm^{-1}]	200	160
locking efficiency	[%]	90	90
divergence, full angle (50 % of the energy)	[mrad]	0.2	0.2
beam dimensions, h \times w	[mm^2]	21 \times 4	21 \times 5
pulse width	[ns]	13	17

Table 2.2 The specification for the tunable ArF and KrF excimer lasers (Lambda Physik EMG 150 MSCT) as specified by the manufacturer

between the narrowband part of the laser output and the total intensity is called the locking efficiency. We have checked the locking efficiency by dispersing a part of the laser beam in a double monochromator (Spex 1401-08) with a resolution of 5 cm^{-1} . On the left-hand side of figure 2.4 the spectrum of the broadband laser radiation is seen. In the middle the spectrum of the narrowband laser radiation is shown. A broadband underground is indeed observed. The broadband part of the laser radiation induces fluorescence, which is mainly observed on the outer sides of the tuning range where the oscillator loses its locking control on the amplifier cavity. The broadband radiation-induced fluorescence complicates the spectroscopic results obtained. With the tunable ArF laser, after three hours of operation the locking efficiency is mostly dropped down to 40%, due to decreasing oscillator power. The gas filling of the laser has to be refreshed to regain its specified output power and locking efficiency. As remarked before, mirror M4 has a special reflective coating in its center to reflect the narrowband oscillator beam. The coating does not transmit the center part of the widened laser beam, therefore generating a small hole in the beam cross section. The lack of laser intensity in, for instance, the middle of a laser sheet causes confusing two-dimensional images. At ArF laser operation this problem is less pronounced, because the oscillator beam is reflected by the 4% reflectivity of an uncoated quartz meniscus lens. The specifications for the tunable ArF and KrF EMG 150 MSCT excimer laser, as specified by the manufacturer, are listed in table 2.2.

Many of the problems discussed above are solved by rearranging the optics in both the oscillator and the amplifier. In the so-called amplified oscillator mode of the laser, the output lacks the broadband underground and the laser energy is homogeneously distributed over the

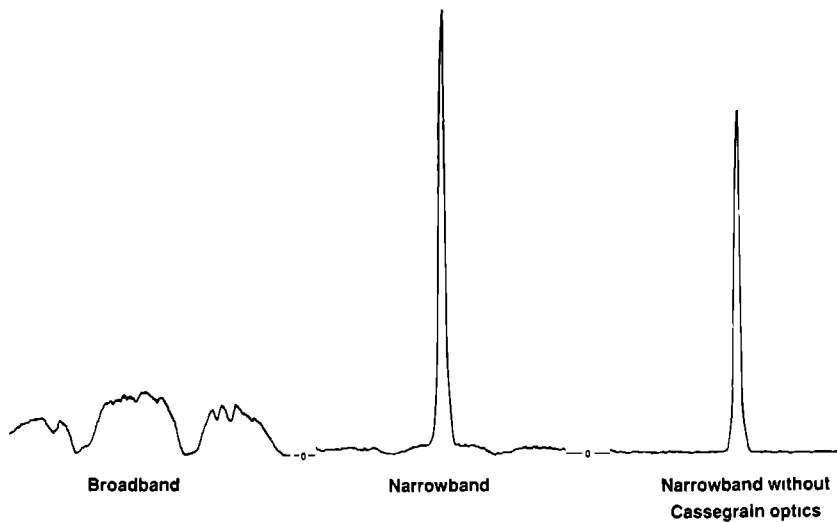


Figure 24 The dispersed output of the tunable excimer laser. Left the broadband output. Middle the laser output when Cassegrain optics are used. Right the laser output in the amplified oscillator mode.

beam profile. Figure 2.5 shows the laser in its new mode. Both diaphragms (D1 and D2) in the oscillator and the unstable resonator optics (M4 and M5) in the amplifier are removed. The oscillator beam now has the dimensions of an ordinary excimer laser beam and is directed in a single pass through the amplifier discharge. The amplifier discharge is not encapsulated by resonator mirrors and has no laser action when not injected by the oscillator beam. The dispersed laser spectrum is shown in the right-hand side of figure 2.4. No broadband underground is observed in this setup. The amplified oscillator mode has clear advantages for spectroscopic applications (lack of underground) and for two dimensional imaging purposes (lack of center intensity dip). Of course, a price must be paid for the reconstruction of the laser. The laser power drops to approximately 50 mJ (half of the original energy) for ArF laser operation and to 225 mJ (almost unchanged) for KrF laser operation. In addition, the laser beam becomes much more divergent, which has negative consequences for focusing purposes, such as Raman shifting. In the course of all experiments both setups are used throughout each other, depending on the specific application. Degenerate four-wave mixing in forward geometry, for instance (see Chapter 6), is not possible with the laser in the amplified oscillator mode. In contrary, the intra-cavity C-atom absorption in the ArF laser tuning range (see Chapter 4) would not have been observed.

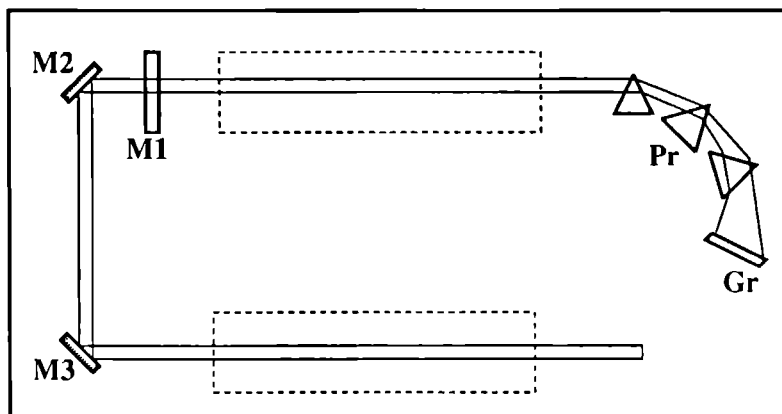


Figure 2 5 The tunable excimer laser in its amplified oscillator mode

with the laser in its commercially delivered configuration

An obvious disadvantage of the tunable excimer laser is its limited tuning range. In wavelength units the tuning range is more or less 1 nanometer for all tunable excimers. The stimulated Raman scattering (SRS) technique offers the possibility to shift the gain profiles of the excimers to other UV regions. Briefly, stimulated Raman scattering is a process where the spontaneous Raman scattering is stimulated coherently to a vibrationally excited level of the Raman-active gas. The frequency of the incident laser light is frequency-shifted several thousands of wavenumbers, corresponding to the difference in vibrational energy in the molecule under consideration.

We have studied the SRS of the tunable ArF excimer laser in hydrogen (H_2). Molecular hydrogen has a Raman shift of 4155 cm^{-1} . We have experimented with different cell and lens configurations. A soft focus in a 100 cm cell turned out to be the best setup to generate the first (S_1) and second (S_2) order Stokes beams at 210 nm and 230 nm, respectively. A saturation of the SRS signals, at 3 and 7 bars respectively, is observed for both components. The stability of the S_1 and S_2 beam is comparable to that of the fundamental laser beam. The components are separated by a Pellin-Broca prism. We have observed very high Stokes components. Even a yellowish green laser beam is observed, which corresponds to the eighth order Stokes beam at 542 nm. We have checked the spectroscopic properties of the second order Stokes beam

by measuring the Q-branch of the two-photon $B^1\Sigma_g^+ (v'=0) \leftarrow X^1\Sigma_g^+ (v''=0)$ CO excitation spectrum [29]. The laser-induced fluorescence is visible by eye as a green discharge in the focus in the cell. Kim et al. [27] have measured new oxygen resonances with the first order Raman shifted tunable ArF laser. Ketterle et al. [25] have measured OH at 277 nm with the first order Stokes beam of a tunable KrF laser. We achieve to get approximately 5% of the fundamental energy into the S_1 or S_2 beams. In particular, in the region above 215 nm, pulsed dye lasers, especially those systems which are injection seeded by a continuous-wave ring dye laser, have a much larger spectral density, because of their higher energy per pulse and their smaller bandwidth. Below 215 nm the use of SRS of a tunable ArF excimer laser offers interesting spectroscopic possibilities, surely since other Raman gases, such as D_2 or CH_4 , can be taken into account. Moreover, the vacuum ultra-violet region can be reached easily by generating several Anti-Stokes beams.

A final word on the maintenance of the tunable excimer laser. As mentioned before, the laser action of the tunable ArF excimer laser is very critical. It takes some time to learn about the peculiarities of the laser. The MgF_2 windows, sealing the discharge cavities, have to be repolished after each month of operation, because metal vapors are deposited on them. The gas mixture has to be warm for optimal performance. We never cool the laser head, when working at 10 Hz repetition rate. After refreshing the gas filling it takes some time for the gas mixture to warm up. The tunable KrF excimer laser acts sort of, as an antipole. Lasing action can be achieved with a piece of white paper. Care should be taken when aligning the KrF laser, since laser action is achieved on almost any reflecting surface. The gas filling of the KrF laser has to be refreshed only once every three or four days. It is known that chlorine- and fluorine-containing excimer lasers can hardly be interchanged. This is even more critical for tunable excimer lasers. It is worthwhile to notice that changes from ArF to KrF affect the discharge conditions to some extent. The discharges of both excimers burn differently on the electrodes. The electrodes lose their optimum shape for the specific excimer and the discharge burns irregularly. This problem mainly concerns the operation of, again, the tunable ArF laser. The instability of the discharge results in an increase of the bandwidth of the ArF laser. We started with a bandwidth of 0.35 cm^{-1} , and now, three years later, we end up with a bit more than 1.2 cm^{-1} , mainly caused by the fact that we now use only two beam-expanding prisms in the oscillator cavity. New electrodes can be installed to regain the quoted specifications. Up to now, we have no experiences with the tunable XeCl excimer laser.

2.2.2 Laser beam transportation and sheet construction

The laser light is directed toward the flame or other object under investigation. In most cases it is sufficient to pass the laser beam (dimension $5 \text{ mm} \times 25 \text{ mm}$) through the flame without focussing. For imaging purposes the laser beam is converted into a laser sheet by cylindrical lenses. We have worked with different lens configurations, mostly with two cylindrical lenses.

($f = 40$ mm and 15 mm) reducing the width of the laser beam from 5 mm to $250 \mu\text{m}$. The height of the laser sheet remains unaltered at 25 mm. The power density increases by an order of magnitude. If higher power densities are required a spherical lens is used to focus the laser photons in or just behind the flame. A tight focus in the area of interest is mostly avoided because of problems concerning the easily ignited breakdown in air, which disturbs the experiments. With a spherical lens enormous energy densities are available. For KrF, for instance, with a 150 mm spherical lens power densities up to $50 \text{ TW}/\text{cm}^2$ are achieved. In some applications very large laser sheets are required. We have obtained slightly diverging laser sheets with a height of 20 cm near the focal point by using a combination of a cylindrical lens ($f = 300$ mm) and a negative spherical lens ($f = -200$ mm). The laser sheet is remarkably thin, approx. $150 \mu\text{m}$.

2.2.3 Fluorescence detection systems

The laser-induced fluorescence is collected in a direction perpendicular to the laser beam. The detection of Rayleigh scattering, peaked collinear with the laser beam and a large precursor at atmospheric pressures, is very much reduced in this setup. Two detection schemes are available. First, a monochromator-based photo-multiplier detection scheme with a high detection efficiency and important properties to study the spectroscopy of molecules. Second, a two-dimensional imaging system producing single-shot 2D maps of the molecules and radicals under investigation. Both detection schemes will be discussed in more detail below.

Monochromator-based PMT detection

The fluorescence is focused onto the entrance slit of a 0.25 m monochromator with a 50 mm diameter Suprasil I lens. In most cases a $f = 100$ mm lens and a 1:1 image is used. The monochromator is then placed at a distance of approx. 40 cm. The transmitted photons are detected by a photo-multiplier. The slits of the monochromator are fixed at a width of $100 \mu\text{m}$, resulting in a resolution of approx. 1 nm. The detected signal is time-averaged in a boxcar integrator and displayed on a fast digital oscilloscope. The gate of the boxcars is usually set to 30 ns, as the LIF signal appears essentially during the laser pulse, due to either the predissociation of the molecule or the quenching of the fluorescence. The averaged signal is recorded on a strip chart recorder. The advantages of using a monochromator-based detection scheme are numerous. First, the monochromator acts as a very narrow bandpass filter, rejecting Rayleigh (and other) scattering and the laser-induced fluorescence of other species in the flame. It also prevents room light and strong emission light from the flame (OH^* , CH^* , C_2^*) to be detected. Second, by scanning a dispersion spectrum the monochromator-based detection scheme helps to assign the spectroscopic features of the molecules that do fluoresce. When scanning a dispersion spectrum, the excitation laser is fixed and the induced fluorescence is dispersed by the monochromator. In this way the branching and the decay channels of the electronically excited state can be

unraveled supplying us with the unique spectroscopic information (a molecular fingerprint) of the vibrational structure of the electronic ground state of the molecule under investigation

2D imaging system

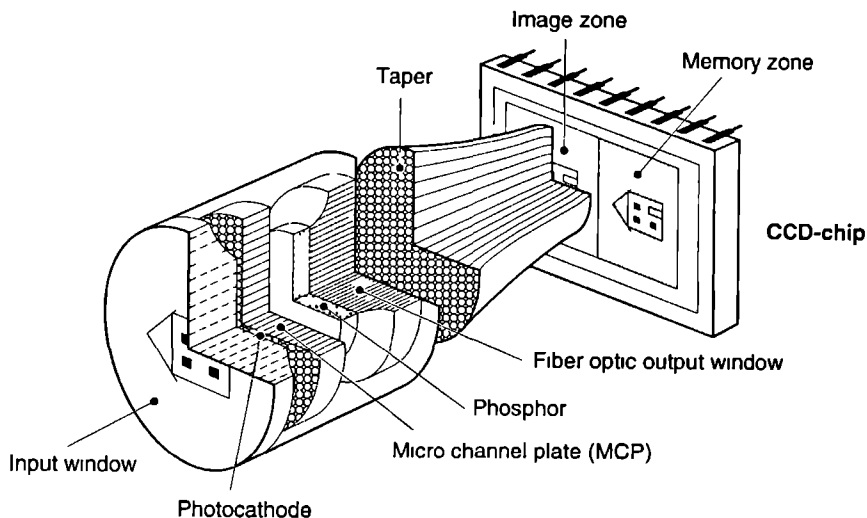


Figure 2.6 An impression of the camera system [30]. A CCD video chip is coupled to the phosphor screen of an image intensifier via a fiber optic taper.

We have constructed a two-dimensional imaging system to detect fluorescence photons generated in a thin laser sheet. An impression of the camera system is shown in figure 2.6. The 2D imaging system is basically constructed of a CCD camera attached to the phosphor screen of an image intensifier. The connection between the intensifier and the video chip is accomplished by a fiber-optic taper. For sharp focusing a UV transparent objective is placed in front of the image intensifier. The CCD camera is connected to a digital image processing unit. This unit digitizes the analog 50 Hz video output. With special software the collected data are acquired and image processing is applied. False-color images are represented on-line on a RGB color monitor. The different parts of the camera system are discussed in more detail in the following.

1. Quartz objective

For sharp focusing a special quartz objective is used. By using normal lenses the images

are blurred and small details are invisible. With the objective images as sharp as $100\ \mu\text{m}$ are easily resolved. The objective is transparent from 200-900 nm and has a focal length of 105 mm. A diaphragm is present in the lens system to increase the depth of field of the images. Sharp focussing is possible over the $\infty - 0.35\ \text{m}$ range. In the experiments described here the diaphragm was always opened and consequently the depth of field was completely determined by the thickness of the laser sheet. In the wavelength region around 200 to 250 nm, a transmission of 70 percent is achieved. Because of the small opening of the lens system (diameter 25 mm), the objective is not well suited for extreme low light level detection. Here, one has to make a compromise between signal to noise ratio and resolution of the image. The objective is attached to the imaging system with a C-type bayonet mount and can therefore be easily removed. Special glass and/or interference filters can be installed in a filter holder in front of the lens system

2. Image intensifier

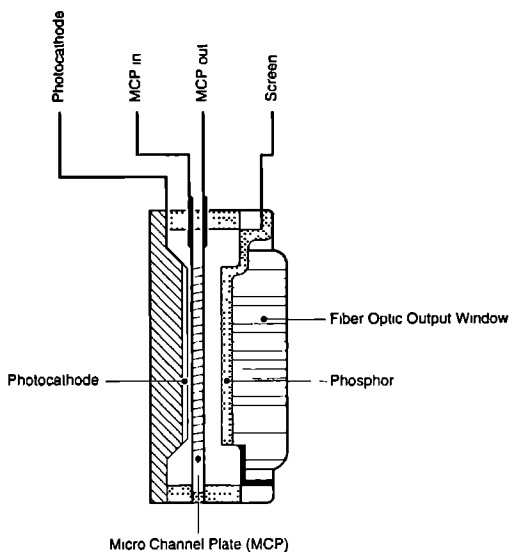


Figure 2.7 : A cross section of an image intensifier. A photocathode ejects photo-electrons and these are amplified by the MCP. The phosphor screen shows the intensified image.

Image intensifiers are light amplifiers which preserve the original image. Image intensifiers are used in many low light level detection applications, such as in medicinal microscopy, astronomical

telescopes and in night vision equipment. An image intensifier is schematically shown in figure 2.7. The intensifier consists of a photocathode (similar to the cathodes of a photomultiplier tube), one or two multichannel plates (MCP) and a phosphor screen. Incident photons are converted into so-called photo-electrons with a given quantum efficiency, in the UV region usually about 8 percent. The image intensifier is gateable by applying a reverse potential between the cathode and the input of the MCP. Gating times as low as 5 ns are obtained for our image intensifier. The photo-electrons are amplified, sometimes as much as 10^6 times, in the multichannel plates. These electrons are then pulled toward the phosphor screen. Here the electrons are converted into photons again. The electrons light up a green phosphorescence for a typical duration of 25 msec, depending on the type of the phosphor screen.

The use of a gated image intensifier is important for several reasons. First, the small number of fluorescence photons have to be amplified. In this way the fluorescence is amplified to such a level that it is now detectable by camera or eye. Second, up to now no video camera systems are available that are able to detect ultra-violet photons directly. In this way the conversion from the UV to the visible (green) is accomplished. Third, video rate cameras work on a sampling time of 16 (US) or 20 msec (Europe). By using an image intensifier the short-lifetime fluorescence (typical lifetime 10 ns) is converted to long-lived phosphorescence (25 ms). The video cameras have sufficient time to detect the fluorescence signal. Finally, the image intensifiers are gateable. This means that the intensifier is only opened at the specific moment when the fluorescence is induced. This reduces the continuous emission light of the object to 6 or more orders of magnitude. The fluorescence is basically collected from a dark object. There are different ways to monitor the phosphor screen of the image intensifier. The phosphorescence can be detected by eye if the room lights are dimmed out. Mostly the phosphor screen is monitored by a CCD camera. The camera allows for image processing and video recording of the phosphor screen.

3 The fiber-optic taper

To match the image on the phosphor screen (diameter 18 mm) onto the chip of the video camera (dimension 9×11 mm), a special configuration is needed. In the early days a simple $f = 100$ mm lens was used to image the phosphorescence onto the chip. Because of spherical aberration problems, some resolution is lost in this configuration. A more direct coupling of the intensifier onto the camera is accomplished with a fiber-optic taper. The taper consists of more than 10^5 fibers and is directly coupled onto the fiber-optics of the phosphor screen, which is already supplied by the manufacturer. The taper reduces the image to the appropriate size. On the camera-side, the taper is also directly coupled to the fiber-optics of the CCD chip, also supplied by the manufacturer. Special immersion oil improves the contact between the two surfaces. The taper also seals the video chip, which is continuously monitoring the phosphor screen, from light leaking through the camera housing.

4 *The CCD video chip*

A CCD video chip monitors the phosphorescence, which is transmitted by the fiber-optic taper. The photo-sensitive layer of the chip contains 390×295 pixels, arranged in a rectangle. An identical, but covered, layer is found next to the first layer. After illumination the image is transferred from the first to the second chip according to the frame transfer principle. From here the image is read out by the electronics of the camera installed shortly behind the chip. Chip and electronics cover only a volume of $3 \text{ cm} \times 2 \text{ cm} \times 1.5 \text{ cm}$. The camera can not be triggered externally and therefore it monitors the phosphor screen continuously. We have used a trick to control the adjustments of the sampling time of the camera and the gating time of the image intensifier. This is discussed in section Triggering. The read-out time of the transfer-chip is slightly less than 20 ms. This is called fast, as 250 kByte of information is transferred in this period. A lot of read-out noise is introduced in this way. The camera can be switched to a slow-scan mode. In this mode the transfer chip is read in 0.3 seconds, thereby eliminating the read-out noise. In this case electronic noise is gaining importance. The shot noise can be drastically reduced by cooling the chip with a Peltier element. In all our experiments so far we did not work in the slow-scan mode, nor did we cool the video chip. In our research of the 100 kW burner, discussed in Chapter 5, Peltier cooling would have led to a longer observation time, because of the heating of the camera system. Progress in the field of video chips is enormous. After one year a camera system is already considered old-fashioned. Some new developments are discussed in Chapter 7.

5 *Image processing hardware*

The analog signal of the CCD camera is digitized in a frame grabber (Matrox PIP-1024) installed in a, 25-MHz Intel 80386 micro-processor-based, personal computer. The frame grabber re-arranges the imported image in a frame buffer containing 512×512 pixels. The dynamical range of the image processing board is at an 8-bits level, sufficient for video rate images containing the read-out noise discussed above.

6 *Image processing software*

We have developed special software to control the image processing board and many other features of our experiment. The program, called MTX, is written in the programming language Microsoft Fortran and Microsoft C with the help of special software libraries supplied with the imaging board. With the software we have access to the digitizers (to set the gain and offset), we control the output signals (color tables, spectra) and we have the ability to select a various number of special functions (averaging, pixel read out, contrast enhancement and many others). Images are snapped from the input signal and stored in the frame buffer of the imaging board. The software has access to this buffer and single images can be processed in many ways (such

as pixel addition, kernel averaging, smoothing and line/column pixel value display) The buffer allows storage of 4 different images The software has the option for two-picture operations, such as subtraction, division and more complicated Boltzmann-plot-like calculations A detailed description of the MTX program can be found in ref [31] Two special option, of interest for combustion diagnostics, will be discussed here in more detail *Spectrum* and *TempPlot*

Spectrum

The software option *Spectrum* offers the possibility to scan molecular excitation spectra with the electronic camera A rectangle in the field of vision of the camera is selected and the pixel values in the rectangle are read out and added while the laser is scanned The image processing board takes snapshots continuously (but synchronized to the experiment, see section synchronization and timing on page 47) For a fast data acquisition these images are directly transported to the expanded EMM memory of the computer Here the fast C-routines act upon the images The sum of the pixel values is entered in a computational array and displayed on the computer monitor The sum can be averaged over several laser shots When scanning the laser a spectrum is built on the screen The spectrum is automatically rescaled when needed The spectrum can be plotted on a plotter or laser printer The stored spectra can be processed Among others they can be divided enlarged interfering peaks can be removed smoothed and many more Scanning spectra this way is very user friendly When a gas is contained in a cell and the (resonant) laser is passed through the cell the camera immediately detects the fluorescence induced The next thing to do is to select the area of interest and to start scanning the laser Compare this with the difficulties met when trying to image an invisible fluorescence signal onto the entrance slit of a monochromator under the correct angles, especially when the laser beam is focused Though this option does not supply us with detailed spectroscopic information on the spectral characterization of the fluorescence (as is obtained with a monochromator based setup), fluorescence filtering in front of the camera already teaches us the major decay channels of the molecule under study An example of a spectrum measured with this function is shown in figure 5 4

TempPlot

The option *TempPlot* is developed to determine two-dimensional temperature distributions in flames The temperature is calculated from the fluorescence intensities of two rotational transitions in OH (see section 1 4 3 and 2 4) using eqn 1 5 The fluorescence fields are measured two-dimensionally in a 512×512 matrix The calculation in eqn 1 5 has to be carried out for every single pixel The Stern-Vollmer factors and the energy difference in the ground state ΔE are asked for in the MTX program For high speed calculation the images are again transported to the EMM memory, now in blocks of 8×8 pixels Here fast C-routines make the Boltzmann calculation The result is written into the memory and after finishing transported back to the

frame buffer. The total calculation time is not more than 2 minutes. Though this option looks sort of trivial, it is really easier said than done. Particularly, handling the small pixel values in a picture-to-picture division requires some thoughts in advance. In section 2.4 some results using this option are found.

7 *Supplementary standard experimental equipment*

The monochrome images delivered by the CCD camera can be stored on a VHS video recorder. The video recorder is a very useful way of storing large amounts of information (corresponding to approximately 20 Mbyte per second), directly. Analog storage has to be applied, however, which results in a loss of information in the images when acquired at a later time. The specific details concerning the problems of data storage on a video recorder are described in ref. [31].

Some additional output devices accompany the computer network. Processed images are plotted on a Paint-jet color printer. A 4-pen color plotter plots selected spectra. The software controlling the plot and print routines is implemented in the *MTX image processing program*.

8 *Optical multi-channel analyzer (OMA)*

The electronic camera system can be installed behind the monochromator of which the exit slit has been removed. The fluorescence passing the entrance slit of the monochromator is imaged onto the photocathode of the image intensifier after being dispersed by the grating. In this way a dispersion spectrum is recorded in a single laser shot. The complete spectroscopic information, both in absorption and in emission, is now obtained by a single scan of the excitation laser. The resolution is determined by the combination of the fringe spacing of the grating, the width of the entrance slit and the row density at the CCD chip. In our setup the resolution of 0.7 nm is determined by the 100 μm width of the entrance slit.

Calibration of the electronic camera system

Before any measurements can be carried out the performance of the electronic camera system has to be tested. The linearity of the camera system has to be checked and the response of the camera when a certain amount of photons are incident has to be calibrated. The calibration is performed with a HeNe laser attenuated with grey filters. A $f = 42$ mm lens increases the diameter of the laser beam to fit the size of the image intensifier. In this setup two variables can be varied: (a) the number of photons incident on the photocathode; (b) the gain of the image intensifier. (a) is varied by using different grey filters or by varying the gating time of the image intensifier; (b) is varied by varying the bias voltage of the image intensifier. The response of the camera system as the number of photons is varied is shown in figure 2.8a.

Here the number of photons is varied by using different grey filters. We have measured at three different gain voltages. We find a linear relationship between the number of photons and

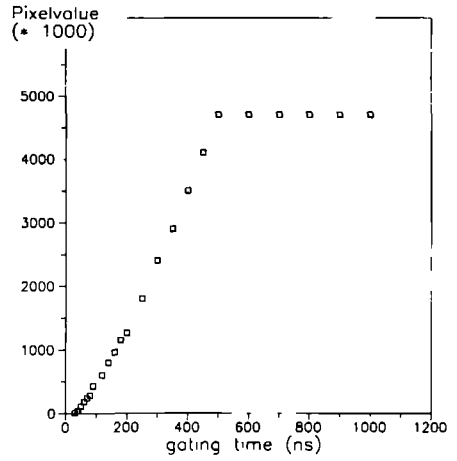
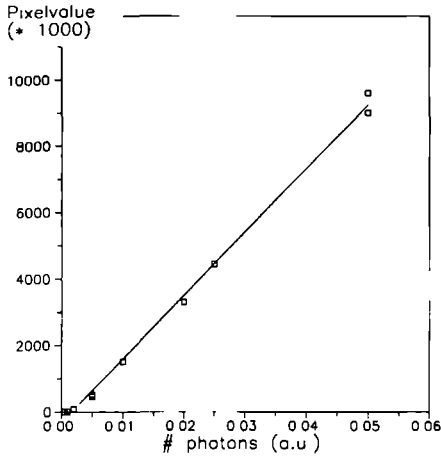


Figure 2.8a(left) and 2.8b(right) : Calibration of the electronic camera system. Left : Different grey filters are used. Right : The gating time is varied.

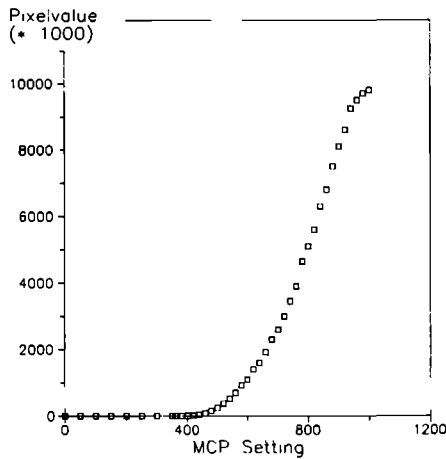


Figure 2.8c : Calibration of the electronic camera system. The gain of the image intensifier is varied.

the total number of pixel values measured with the camera system. In figure 2.8b the gating time is varied at a MCP setting of 800. Here we also find a linear correspondence between number of photons and the sum of the pixel values. Note that the image intensifier can not be gated longer than 500 ns. Finally in figure 2.8c the response of the camera system is shown as the gain of the image intensifier is varied. Between 700 and 900 the number of pixel values grows more or less linearly with the applied MCP voltage. Therefore this region is selected for our experiments. As observed in figure 2.8c it is hardly of any use to turn the camera to the maximum gain as the MCP saturates at these high amplification factors.

To determine the relationship between the pixel value measured by the camera system and the number of photo-electrons, we measure the power of the HeNe laser with a calibrated photodiode. We measure a power of 2 mW at 632 nm. This corresponds to 6.4×10^{15} photons/s. With a 2% transmission grey filter and a gating time of 200 ns, the number of photo-electrons generated is 2×10^6 . A quantum efficiency of 8% is assumed. The camera system records 3×10^6 counts at a MCP setting of 800. This means that with our electronic camera system we are able to detect single photo-electrons. Moreover, the camera is linear in a large range, which makes the unit suited for quantitative spectroscopy and for 2D imaging.

Synchronization and timing

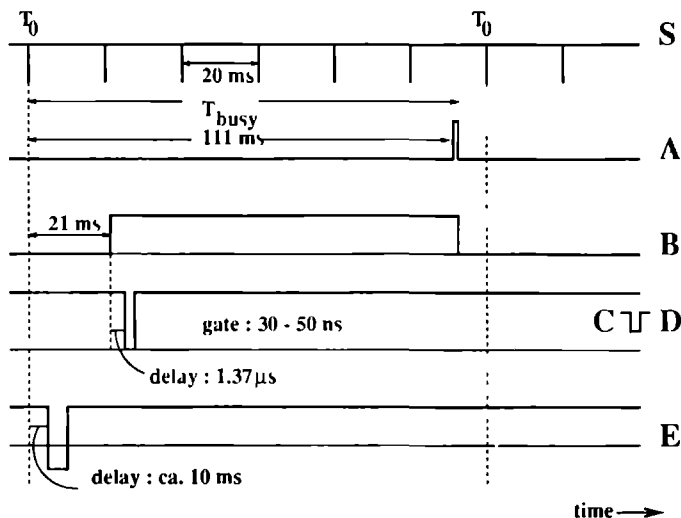


Figure 2.9 The timing diagram of the experiment

The main role in the synchronization and timing is claimed by the pulse/delay generator

The pulse generator determines which apparatus receives a trigger pulse at what given time. This is schematically shown in figure 2.9 and 2.10. The bars are electronically connected to the different experimental apparatus with the appropriate time delay. The CCD camera (1) can not be triggered externally. Therefore the complete experiment is locked to the internal synchronization pulses of the video chip. The communication between video chip, computer (2) and RGB monitor (3) is accomplished in the Matrox image processing unit, installed in one of the computer slots. The unit can be locked to the internal computer synchronization or to the external camera or video synchronization. The image processing unit sends the selected sync-pulse to the RGB monitor. Here, the synchronization pulse is extracted. In this way the internal video rate camera cycle is available indirectly by the external sync-mode of the Matrox image processing unit.

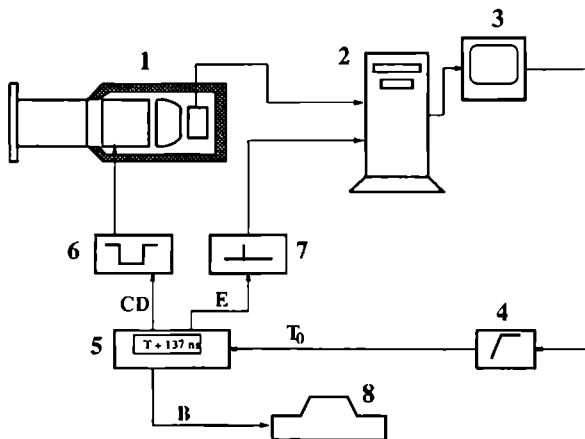


Figure 2.10 The pulse/delay generator controls the neural network of the experiment. The numbers are explained in the text.

An image on the RGB monitor is built up of so-called half-images. A half-image is displayed in either the even or the odd rows. One cycle ($= 20$ ms) later the next half-image is displayed in the alternate rows. The synchronization pulse of the monitor is a complex high-frequency pulse containing the information and trigger pulses for every row to fill. It also contains the 50 Hz trigger pulse for the monitor to start a new half-image at the left-hand upper corner of the screen. This latter trigger pulse is extracted from the high frequency synchronization pulse by means of a frequency filter (4). The 50 Hz trigger pulse (S in figure 2.9) is used to trigger the pulse/delay generator (5) and determines the reference time T_0 for all other trigger pulses.

It is now possible to snap images at the same time in every camera cycle. This is important for averaging collected data. The Matrox image processing board does not have an option to average images on board. This is the main reason for developing the timing diagram described above. It takes some time for the computer to transfer an image from the imaging board to the EMM memory of the computer, where all images are added for averaging. A frequency of 50 Hz is therefore not realistic. The sync-frequency has to be divided. This problem is solved by using a special feature of the pulse/delay generator. The pulse generator does not accept a new trigger pulse before the longest delay time plus $800 \mu\text{s}$ has elapsed. This time is called T_{busy} (see figure 2.9). We select a relatively long delay time for channel A, sufficient for the computer to read out the frame buffer of the image processing board. The value of 111 ms ($= 5 \times 20 \text{ ms} + 1 \text{ ms}$, recording every sixth frame) is selected for most of the applications. With this value the experiment runs at a repetition rate of slightly more than 8 Hz. The computer needs a trigger to start reading out this frame buffer. A separate simple pulse generator (7) triggered by the T_0 pulse, sends a pulse to a data port (COM2) of the computer. The software controlling the imaging board reacts on this special trigger pulse. It turns out that the computer needs time (several milliseconds) to start taking a snapshot. Therefore the computer trigger pulse (pulse E) has to be given before firing the laser and opening the image intensifier. The firing of the laser (8) is controlled by trigger pulse B, delayed 21 ms with respect to T_0 . Finally the image intensifier has to be opened and closed at the correct moment. We need two delay channels for this, trigger C is delayed with respect to trigger B (i.e. the time delay for the laser to fire after receiving its trigger pulse approx. $1.4 \mu\text{s}$) and trigger D is delayed with respect to trigger C determining the corresponding gating time (30 - 50 ns). The delay times have to be adjusted some times during an experiment. The delay time between trigger B and C is the most critical due to thermal effects. All data are collected in either the even rows or the odd rows. By changing the value of T_{busy} to e.g. 131 ms ($= 6 \times 20 \text{ ms} + 1 \text{ ms}$, recording every seventh frame), the data will appear in alternating rows.

2.2.4 Burner systems

In our experiments we have utilized burners of designs with different fuels with different dimensions and constructed for different applications. They are summarized and discussed briefly below.

1 Regular type burners

In the laboratory three regular type burners are used. First, probably the most common burner, the Bunsen burner. The Bunsen burner burns a premixed methane (or natural gas) / air mixture. The air is mixed at the base of the burner. When the air supply is blocked a sooty flame burns on the burner head. The stoichiometry can be varied only roughly. The Bunsen burner is used as a calibration flame, rather than for quantitative spectroscopy because of its

instability. Second, an oxy-acetylene welding torch, with a rather high combustion temperature is used. The torch flame is nitric oxide-rich, because of its high temperature. The flame has a high velocity and is stable when a proper C_2H_2/O_2 mixture is supplied. This burner is used as a calibration flame when performing NO measurements (chapter 5) and for quantitative NO spectroscopy (chapter 3). Finally, we have at our disposal a H_2/O_2 glass welding torch. This flame is very OH-rich, but the main reason for using this burner is the fact that hydro-carbons are absent. When utilizing a monochromator in the second order reflection of its grating (because the grating is not blazed for the ultra-violet wavelength region), the emission of electronically excited radicals (OH^*, CH^*) in the flame dazes the photo-multiplier, unless gated. Extreme care should be taken when burning hydrogen with oxygen.

2. Adiabatic burner

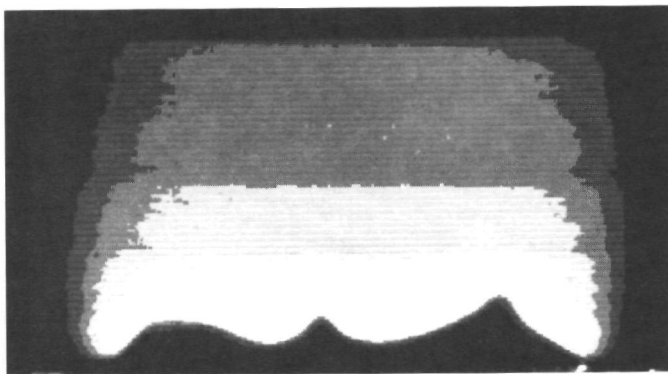


Figure 2.11 : Laser-induced fluorescence of OH observed from the adiabatic burner. The OH radicals are distributed in structured layers. The flame is shown in near blown-off conditions.

In cooperation with the Technical University of Eindhoven (TUE), the Netherlands, we have started experiments on quantitative temperature determinations. A special technical adiabatic burner is constructed. Theoretical calculations of the temperature distribution in the flame of the adiabatic burner can be performed. The flame burns at a level of adiabatic energy exchange. The

flame radiation and energy release to the cooling water are in equilibrium, which makes the flame reasonably easy to model. The burner uses methane as fuel. The circular burner head consists of approximately 2800 pinholes with a diameter of $400\ \mu\text{m}$ each. The flame is computer controlled. Both the stoichiometry and the gas mixture flow velocity are adjustable by computer-controlled mass flow controllers. Just below the burner plate a set of thermo-couples are installed. The thermo-couples check the temperature of the gas mixture before it is burned on the burner head. If a flat temperature profile is found, the flame burns adiabatically. With a one-dimensional laminar gas flame model [32], developed at the TUE, the flame temperature is calculated, given certain burner conditions. In figure 2.11 the OH distribution in this flame is given. Note the flat structure of the different OH concentrations. Some results of the experiments performed with the adiabatic burner are discussed in section 2.4. More details on the burner are found in ref. [33].

3 Ceramic burner

We have performed some preliminary experiments in a low NO_x ceramic burner, in cooperation with the Energy Research Centre of the Netherlands (ECN), Petten, the Netherlands. At ECN research is done to minimize exhaust of polluting species. The use of porous ceramics as a material for the burner plates in natural gas burner systems seems to be a solution for this problem because of the lower combustion temperatures. This new type of burner is, in principal, better to adjust if compared to conventional burners and has a much smaller exhaust of polluting species. The burner is utilized with a burner plate, made of ceramic foam with a dimension of approximately $11\ \text{cm} \times 11\ \text{cm}$, which from the bottom side is supplied with a premixed methane/air mixture. The gas is burned on the ceramic plate in the open air. Between $100\ \text{kW/m}^2$ and $2000\ \text{kW/m}^2$ a very low NO_x exhaust is achieved. The burner act as a radiation burner up to approximately $700\ \text{kW/m}^2$. At higher powers the burner plate acts as the burner head, with a flame on top. We have focused on the oxygen distributions in the burner.

4 Scaled 100 kW coal power plant burner (KFMV)

We have studied a down-scaled power plant burner, burning natural gas and air. The burner has a power of 100 kW. The flame is very turbulent and has a length of approximately 2 meters and a diameter ranging from 20 to 50 cm, depending on the stoichiometry of the gas mixture. Chapter 5 deals with the study of OH and NO distributions in this 100 kW flame.

5 Glass welding torches (Philips)

In cooperation with N.V. Philips we have made a preliminary study of the interaction of flames of glass welding torches, burning natural gas and air, on glass or quartz surfaces. An image is shown in figure 2.12. Here, a quartz rod is rotating around its axis and the flame

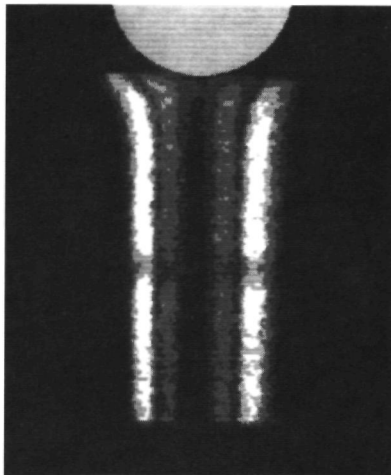


Figure 2.12 : Laser-induced fluorescence of OH observed from the flame of a glass welding torch of Philips. The flame heats a rotating quartz rod.

burns from the bottom side. The flame front is visible, surrounded with a mantle of OH. In the center photo-dissociated hydro-carbons, which are also fluorescing, are visible. The image is approximately 3×3 cm.

2.3 The molecular spectroscopy of transient combustion species studied with a tunable ArF and KrF excimer laser

1. Hydroxyl (OH)

The hydroxyl radical plays an important role in the intermediate chemical reactions occurring during combustion. It is present in large quantities, up to several Torr in atmospheric flames. The OH radical is distributed in a large area of the flame, which makes it an interesting molecule to use for temperature determinations. OH is detected with a tunable KrF laser at 248 nm. An energy level diagram is shown in figure 2.13.

The radicals are excited from the $X^2\Pi$ ($v''=0$) ground state to the first electronically excited $A^2\Sigma^+$ ($v'=3$) state. Different rotational states, ranging from $N = 6$ to $N = 15$ with a ground

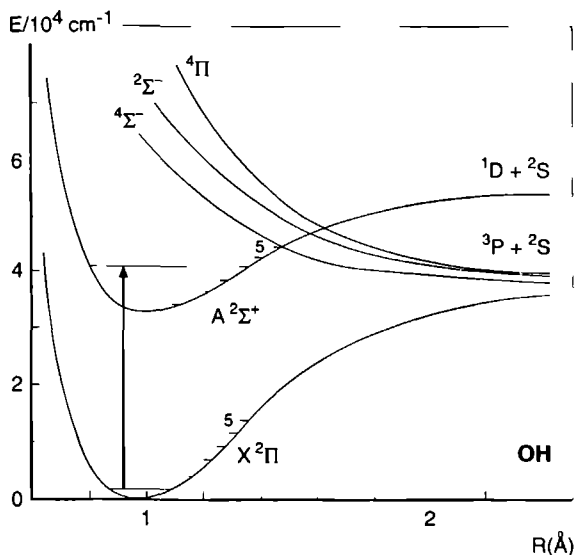


Figure 2.13 An energy level diagram for the hydroxyl radical [34]. The $X^2\Pi$ and $A^2\Sigma^+$ states are shown. The repulsive quartet states are also indicated.

state energy difference greater than 3000 cm^{-1} , are excited in the frequency range covered by the tunable KrF laser. The large energy difference allows for an accurate temperature determination, as discussed in section 1.4.3.

The $A^2\Sigma^+$ ($v'=3$) state of OH is a predissociating state with a predissociation lifetimes of 20 - 200 ps, depending on the rotational quantum number. The repulsive states responsible for the act of predissociation are indicated in figure 2.13. Because many states are involved in the process of dissociation it is difficult to calculate the expected lifetime of the $v' = 3$ state, not to speak of the rotational level dependence of the predissociation. The short lifetime allows for a quantitative determination of densities and temperatures as already discussed in section 1.4. In section 2.4 the rotational level dependence of the predissociation will be discussed in more detail. The fast predissociation leads to a large loss in fluorescence. Moreover, the $3 \leftarrow 0$ transition has a relatively small Frank-Condon factor. The high power of the KrF excimer laser compensates for the loss in fluorescence. The fluorescence is emitted to the $v''=1$ (270 nm), $v''=2$ (295 nm) and $v''=3$ (330 nm) states in the ground state of OH with an intensity ratio of 1 : 4 : 1, respectively. The off resonance fluorescence causes a high detection efficiency because

of the absence of straylight problems. In addition, the fluorescence is emitted to unpopulated levels in the ground state, eliminating fluorescence trapping.

The hydroxyl radical can be detected also by Raman shifting the KrF excimer laser [25, 20, 35]. The radicals are excited to the $A^2\Sigma^+$ ($v' = 2$) state. This state is only slightly predissociated resulting in a larger quantum efficiency, according to eq. 1.4. Especially when only qualitative data are requested, this option supplies the experimenter with high S/N ratio images. The tunable XeCl excimer laser, exciting the $v'=0 \leftarrow v''=0$ transition, can also be used for the detection of hydroxyl radicals.

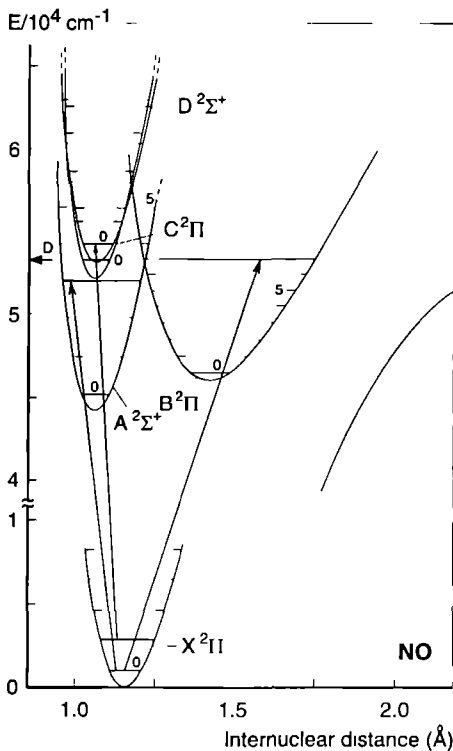


Figure 2.14: An energy level diagram of the nitric oxide radical. The bottom of the $X^2\Pi$ potential curve is drawn. The electronically excited potential curves reached by the tunable excimer laser are indicated.

2. Nitric Oxide (NO)

The visualization of nitric oxide in flames and combustion is important as NO has acidifying environmental effects. Once at higher altitudes in the atmosphere NO reacts with several chemical species producing acid rain. Nitric oxide emission should therefore be reduced as largely as possible. NO is measured with a tunable ArF excimer laser at 193 nm. An energy level diagram is shown in figure 2.14. Two transitions are easily accessible, one chooses according to application. The $B^2\Pi (v'=7) \leftarrow X^2\Pi (v''=0)$ transition is preferably excited when NO is contained in sub-atmospheric pressure cells. The electronically excited state has a lifetime of approximately 500 ns and the fluorescence from this state extends into the 450 nm region. When NO is monitored in a flame the $D^2\Sigma^+ (v'=0) \leftarrow X^2\Pi (v''=1)$ is preferred. The transition is strong with a fluorescence lifetime of approx. 20 ns, resulting in a much stronger fluorescence signal due to a large Stern-Vollmer factor. The $B \leftarrow X$ transition is not observed in a flame due to its relatively long lifetime. The $D^2\Sigma^+ (v'=0)$ level fluorescence is confined to the wavelength region near 210 nm, mainly emission down to the $v'=3$ level in the ground state of NO. The spectroscopy of nitric oxide at 193 nm is extensively discussed in chapter 3.

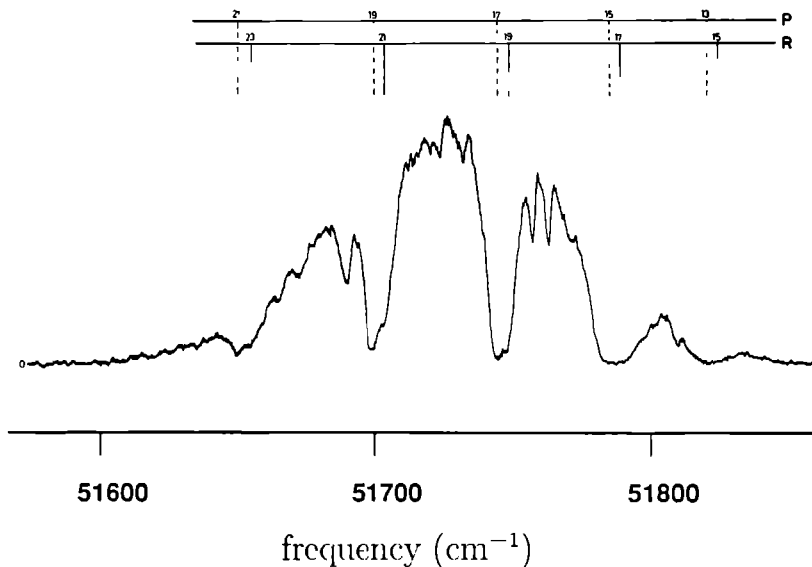


Figure 2.15 : The gain profile of the tunable ArF excimer laser when transmitted through air. The absorptions are due to the Schumann-Runge (4-0) transition.

3 Oxygen (O_2)

The most inevitable molecule in combustion, oxygen, is also monitored with a tunable excimer laser. Both ArF and KrF tunable excimer lasers are used. Oxygen has many transitions, the so-called Schumann-Runge bands, in the deep ultra-violet. The bands are discrete, but move closer and closer together in the wavelength region near 175 nm, where the continuous oxygen absorption band appears. The many absorption bands cause problems when the ArF laser radiation is transported through air, for instance. In figure 2.15 the gain profile of the ArF laser is shown. The $B^3\Sigma_u^- (v'=4) \leftarrow X^3\Sigma_g^- (v''=0)$ transition causes large absorptions in the gain profile of the excimer, as discussed in section 2.2. Vibrationally excited oxygen in flames is monitored with the tunable ArF laser. The strongest features observed using this laser are the $B^3\Sigma_u^- (v'=10,11) \leftarrow X^3\Sigma_g^- (v''=2)$ transition and the $B^3\Sigma_u^- (v'=14,15,16,17) \leftarrow X^3\Sigma_g^- (v''=3)$ transition. The fluorescence is observed to very high ground state vibrational quantum numbers (up to $v''=35$ in some cases). The fluorescence has an oscillating pattern caused by the vibrational overlap of the wave functions, the Franck-Condon factors.

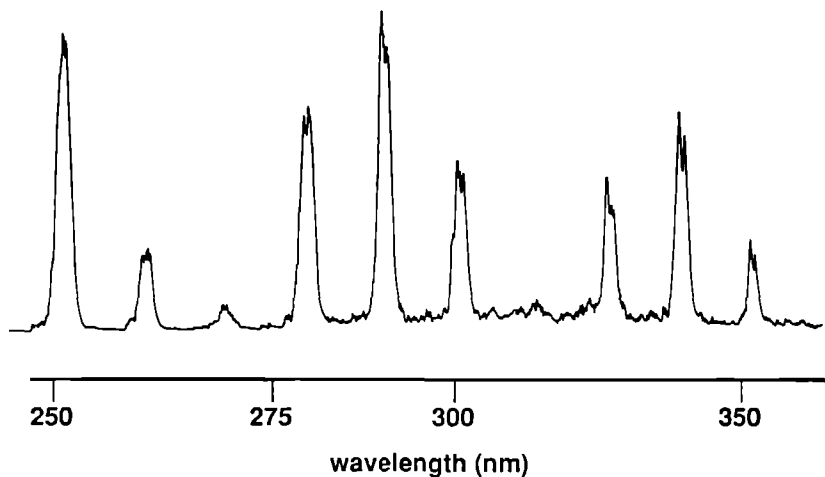


Figure 2.16 A dispersion spectrum of oxygen excited by a tunable ArF excimer laser at 193 nm. The Schumann-Runge (4,0) transition is excited.

A dispersion spectrum is shown in figure 2.16. The oxygen molecule is also detected with the tunable KrF excimer laser at 248 nm. The $B^3\Sigma_u^- (v'=0,1) \leftarrow X^3\Sigma_g^- (v''=6)$ and $B^3\Sigma_u^- (v'=2) \leftarrow X^3\Sigma_g^- (v''=7)$ Schumann-Runge band transitions are excited. The oxygen molecules are

vibrationally hot and originating from molecular reactions rather than thermal heating. More specific details on the spectroscopy of the oxygen molecule can be found in ref [17, 19, 18]

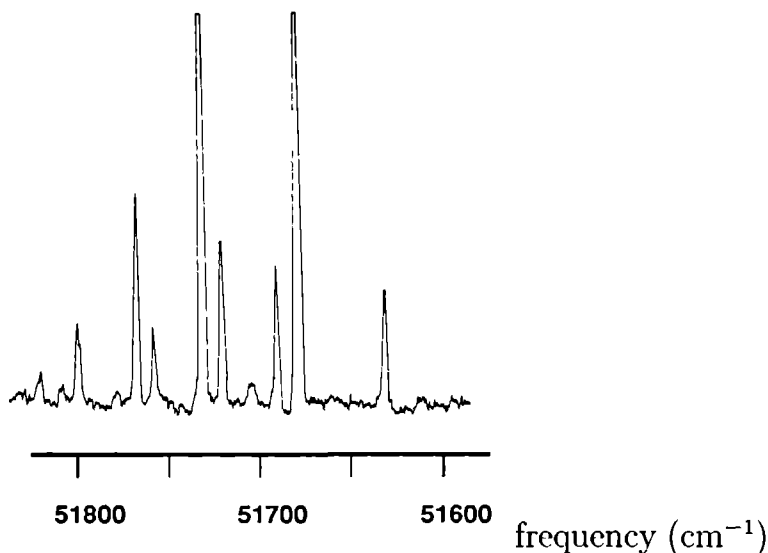


Figure 2.17 An excitation spectrum of the unidentified transition of oxygen. Oxygen molecules are excited by a sharply focussed tunable ArF laser at 193 nm

We have observed new features when focusing the tunable ArF excimer laser in air. An excitation spectrum is shown in figure 2.17. These resonances can not be assigned to the Schumann-Runge band transitions. The spectrum is also observed in a cell containing pure oxygen. The fluorescence is very strong and can be observed by eye when the room lights are dimmed out. A white laser beam is observed. The fluorescence has been observed before by Huo et al [36]. We did not succeed in assigning the observed features, despite the many different experiments we performed. The limited tuning range of the excimer laser complicates a clear spectroscopic assignment. We speculate that the resonances belong to a transition in the quartet system of the oxygen ion. By focussing the laser beam tightly oxygen ions are formed, either by direct three-photon ionization or by secondary reactions with reactive species. Many transitions of O_2^+ lie within the tuning range of the ArF laser (e.g. $c^4\Sigma \leftarrow b^4\Sigma$ at 51700 cm^{-1}). The strong lines in the spectrum of figure 2.17 have a splitting of 0.9 cm^{-1} , which is also observed in emission spectra of the $c \rightarrow b$ transition. Little spectroscopic information is available, however, for the high-lying quartet states of the O_2^+ ion. The preceding explanation is most speculative and

is not supported by a constructive experimental evidence. An excitation spectrum, measured over several nanometers (with a dye laser e.g.), would help to assign the spectrum discussed above.

4 Carbon Monoxide (CO)

Carbon monoxide, though not present in a flame at large quantities, plays an important role in combustion by its reaction with the hydroxyl radical. Carbon monoxide is poisonous and odorless, therefore an originator of many deaths from asphyxiation when emitted by badly tuned up geysers and stoves. Carbon monoxide is detected with the tunable ArF excimer laser via its spin-forbidden $a^3\Pi (v'=2) \leftarrow X^1\Sigma_g^+ (v''=0)$ transition. The metastable CO molecules absorb two additional 193 nm photons to end up in a dissociative continuum to produce metastable C atoms, which fluoresce at 247.9 nm. Chapter 4 of this thesis will deal in greater detail with the multiphoton laser-induced fluorescence scheme discussed above.

Carbon monoxide can also be detected via the two-photon $B^1\Sigma_g^+ \leftarrow X^1\Sigma_g^+$ transition at 87000 cm^{-1} . The tunable ArF excimer laser is Raman shifted and the second Stokes order is used to excite the molecules to the B state. A Q-branch with many overlapping rotational transitions is observed. S- and O-branch transitions are not observed because of their relatively weak transition probability [37].

5 Water (H₂O)

Water, one of the two major end products of combustion, is detected by laser-induced fluorescence with a tunable KrF excimer laser. The two-photon $\tilde{C}^1B_1 \leftarrow \tilde{X}^1A_1$ transition is excited. Different decay channels exist. A large part of the excited water molecules dissociate and form OH radicals in its first electronically excited $A^2\Sigma^+$ state, whereafter its fluorescence to the ground state at 308 nm is monitored. Many excited water molecules are transported further up in energy to produce water ions. Another important decay channel is the $\tilde{C}^1B_1 \rightarrow \tilde{A}^1B_1$ bound-free transition. Emission to the repulsive \tilde{A}^1B_1 state (similar to the excimer energy level diagram) occurs between 400 and 500 nm. The dynamics of the excited \tilde{C}^1B_1 is discussed in detail in ref [38].

6 Hydrogen (H₂)

The visualization of the hydrogen molecule shows its importance in numerous applications associated with aviation and space agencies. Hydrogen is a fuel for many (future) jet engines and is usually burned in supersonic combustors. The two-photon E,F \leftarrow X transition in H₂ is often used in a (2+1) REMPI experiment. A (2+1) REMPI spectrum is shown in figure 2.18. Here only 10^{-6} Torr of hydrogen gas is contained between the REMPI electrodes. The excited state fluoresces, too, in the near infrared region [39] at approximately 850 nm. A red-sensitive image intensifier has to be replaced by the UV-sensitive image intensifier of the electronic camera.

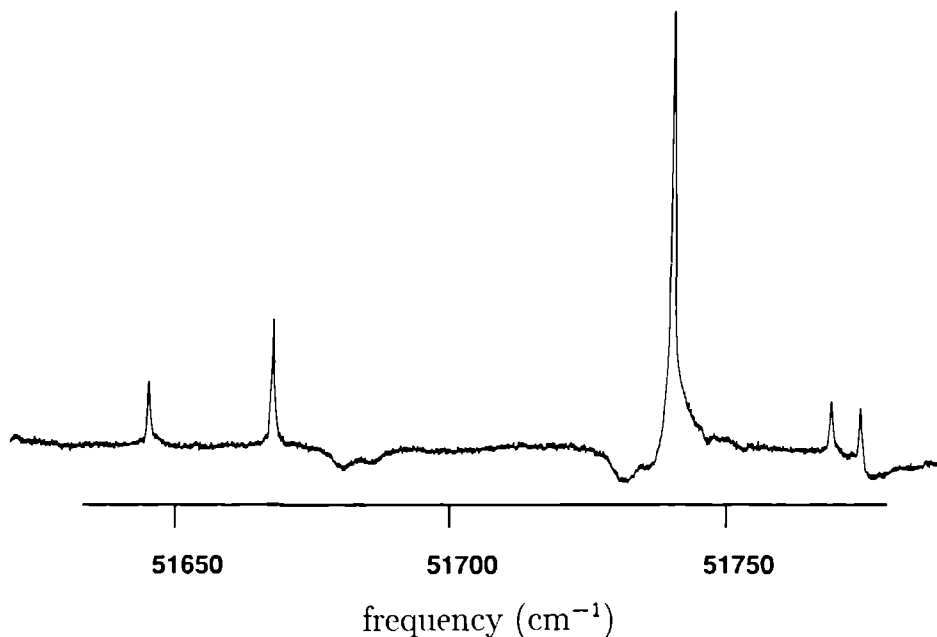


Figure 2.18 A (2+1) REMPI spectrum of hydrogen measured with a tunable ArF excimer laser at 193 nm. The $E, F^1\Sigma_g^+$ ($v'=6$) \leftarrow $X^1\Sigma_g^+$ ($v''=0$) transition is excited.

system

2.4 Temperature determinations via OH LIPF

When the state distributions of molecules are used as temperature indicators, a suitable molecule should be selected. Nitrogen, since it is most abundant in a flame, is a good candidate. However, it is difficult to excite and it hardly fluoresces. The nitrogen molecule is selected in CARS thermometry. The hydroxyl (OH) radical is another good candidate, since it covers a large region of the flame and is reasonably abundant (up to 1 %) for an intermediate species. The OH radical is easily monitored in fluorescence. When the $A^2\Sigma^+$ ($v'=3$) \leftarrow $X^2\Pi$ ($v''=0$) transition of OH is excited at 248 nm the fluorescence is collision-free which allows, in principle, quantitative density and temperature measurements. The excitation spectrum has numerous lines lying within the gain profile of the tunable KrF excimer laser. The ground state energy difference of these rotational lines is large, which implies a good temperature resolution up to 40 K. Oxygen seems to be another good candidate, since it has very fast predissociating states, with lifetimes down

to 2 picoseconds. Within the gain profiles of the excimers the rotational lines of the oxygen molecule lie too close together, however, for a good temperature resolution. The B constant of the $X^3\Sigma_g^-$ state is too small to see a difference in the ground state density distribution at flame temperatures.

We take a closer look at eqn. 1.7. The ratio of the state distributions n_1/n_2 is calculated from the fluorescence intensities F_i using eqn. 1.4. Eqn. 1.7 can now be written the following:

$$T = \frac{E_2 - E_1}{k \ln \left(\frac{S_2 I_2 P_1 I_1 (2J_2 + 1) F_1}{S_1 I_1 P_2 I_2 (2J_1 + 1) F_2} \right)} \quad (2.1)$$

with S_i , the line strength, including Franck-Condon and Honl-London factors and with A_i and P_i , the fluorescence and predissociation rates, respectively. I_i is the laser intensity. Here we assume the absorption cross section to be the same for the two rotational transitions. The values needed in eqn. 2.1 are known from spectroscopy. A problem arises when dealing with the terms for the predissociation, because it is known that it has a rotational level dependence [40]. Recently, Gray and Farrow [41] and Heard et al. [42] have investigated this problem experimentally. They indeed found a rotational level dependence, but the values are not in agreement with each other. Gray and Farrow's values are not measured for high rotational quantum numbers and seem to be non-applicable when using LIF of OH in the KrF excimer laser tuning range. We have also checked the values of the Crosley group in an adiabatic flame on which theoretical temperature calculations are also performed. Up to now we have not yet successfully measured absolute temperatures quantitatively. We did, however, learn the difficulties associated with the experiments with a tunable KrF laser and these will be discussed in this section.

2.4.1 Required information

1 Spectroscopic information

Applying eqn. 2.1 a list of spectroscopic information is needed. Not only the spectroscopy of the OH radical must be known. The oxygen molecule has many rotational lines in the tuning range of the KrF laser. When selecting an OH line for temperature measurements, one has to be sure that the line is free of other OH or O_2 excitation lines. Of the OH lines selected for temperature measurements, one has to know the ground state energies. These are listed in ref. [43]. Furthermore, the ground state quantum number J and the excited state electronic radiative decay rate A are asked for. The Franck-Condon factors and electronic transition moment are fixed, because we deal with transitions between states with the same quantum number. The Honl-London factors are taken from ref. [43] or [38].

Care should be taken in choosing the way of fluorescence filtering. When a single line is excited, a set of P, Q and R lines are observed. The fluorescence lines lie several nanometers apart, easily resolved by a simple monochromator, due to the large B constant of the OH

molecule. The fluorescence of different excitation lines lies apart also, because of the difference in B constants in the $^2\Pi$ and $^2\Sigma^+$ states. Normally, broadband fluorescence filtering with a UG-11 glass filter is applied. Here the fluorescence from 275 to 350 nm is transmitted. Fluorescence from levels other than $v'=3$ are transmitted as well. These levels are populated through vibrational energy transfer (VET) in the electronically excited state. Although only a very small fraction is transferred the detected fluorescence from these levels is strong, because of the large Franck-Condon factors, which are typically 2 orders of magnitude larger than for the $v'=3 \rightarrow v''$ transition. The fluorescence of the levels populated by VET is quenched, because of the longer lifetimes of the levels. The total fraction of VET-induced fluorescence amounts up to 20 to 40 %, depending on the type of flame [17]. Narrowband interference filters (5 nm) are used to select only the $v'=3 \rightarrow v''=2$ fluorescence. Then, the detected fluorescence is free of VET, but since this fluorescence is spread over several nanometers, one should be aware of the fact that some fluorescence is not detected in this setup. This of course affects the temperature measured from the line intensities. In our temperature determinations so far we have only used a 2 mm thick UG-11 filter in front of the camera system.

2. Excitation conditions

It is important to check the excitation conditions of the fluorescence observed. The fluorescence is proportional to the density in the probed state only when the transition is linearly excited. The intensity of the laser light at different excitation frequencies must be known, as it is appears in eqn. 2.1. We measure our fluorescence data digitally with the camera system. We automatically normalize our fluorescence intensities by dividing it by the corresponding laser light intensity. The intensity is measured in the following way. A part of the laser beam is extracted by means of a MgF_2 beam splitter. This reflected part is passed through a set of grey filters and is focused onto the surface of a quartz fiber. The opposite end of the fiber is placed just next to the flame under investigation in the field of view of the electronic camera. In a single laser shot, the camera detects both the laser-induced fluorescence of the OH radicals in the flame and the part of the laser beam transmitted through the fiber. With the option *Spectrum*, described in section 2.2.3(6), two rectangles are selected and read out when scanning the laser frequency. In this way a normalized excitation spectrum is measured. Note, that only the narrowband laser light induces the fluorescence of the single lines observed and that consequently only the narrowband part of the laser output should be monitored. When the laser operates in the mode using Cassegrain optics, especially on the sides of the tuning range, the output of the laser contains both broadband and narrowband radiation. Therefore, when temperature measurements are performed the laser must work in the amplified oscillator mode in order to be able to monitor the laser light intensity correctly.

As mentioned before, the excitation must be linear, i.e. the fluorescence must be proportional to the laser intensity. The product of the absorption cross section σ and the laser intensity I

should be much smaller than unity in this case. If not, upper state molecules are pumped down by stimulated emission. This causes the molecules to be divided among the two states and saturation of the fluorescence is observed. At the 0-0 transition of OH, when increasing the laser intensity, this is very quickly the case (at several μJ 's), because of the high absorption cross section of the transition. For the 3-0 transition the Franck-Condon factor is 30000 times smaller and saturation of the fluorescence intensity is observed only at very intense and focused laser pulses. Here, we must bear in mind that this transition has a fast predissociation and most molecules disappear before they are pumped down by the laser again. A large fraction of the molecules are pumped away from the ground state however, leaving behind a deep hole in the Boltzmann distribution. Collisions in the ground state are fast and the probed level is repopulated from neighboring rotational levels during the laser pulse. This rotational energy transfer (RET) increases the number of fluorescence photons, consequently falsifying the experimental results. When the population of the probed level is kept at comparable number with respect to the neighboring levels, refilling of the probed level is more or less avoided. From ref. [41] and [42], 5 to 10 MW/cm^2 can be considered to be the upper limit to use when exciting OH in an atmospheric flame. This implies the use of not more than 5 mJ in a normal sheet with a tunable KrF excimer laser when depletion of the ground state levels is to be avoided.

2.4.2 Rotational-level dependent predissociation

It was already known for several years that the $v'=3$ level of OH has a rotational level dependence of its predissociation. Sink et al. [40] made theoretical calculations on different vibrations of the $A^2\Sigma^+$ state. Three repulsive states disturb the bound potential curve of the $A^2\Sigma^+$ state, as shown in figure 2.13. Recent measurements by Copeland et al. [44] support earlier theoretical speculations that the predissociation of the higher vibrational levels ($v' > 5$) is dominated by the 4Π state. The lower levels ($v' < 2$) are most likely predissociated due to a mixing with the repulsive $4\Sigma^-$ state. The predissociation of the $v'=3$ and 4 levels is caused by a combination of mixing of the bound state and the repulsive states.

Very recently, Gray and Farrow [41] measured absolute predissociation rates in the $A^2\Sigma^+$ $v'=3$ level using linewidths from a Doppler free double-resonance technique in a flow tube. Heard et al. [42] made measurements of the relative predissociation rates as a function of rotational level using LIF excitation scans in low pressure flames. Gray et al.'s experiment gives absolute rates up to $N'=9$, Heard et al. give relative rates for $N'=0$ through 14 within the $v'=3$ level. When the two studies are compared some data points indeed overlap. However, large deviations, up to a factor of three, are found for other data points. Such large deviations cause temperature differences of 3000 K, which are of course out of proportion. In the next section we compare the predissociation rates with our own preliminary results obtained from a calibrated atmospheric methane/air flame.

The predissociation rates of the OH $A^2\Sigma^+$ ($v'=3$) level from ref. [41] and [42] are given in

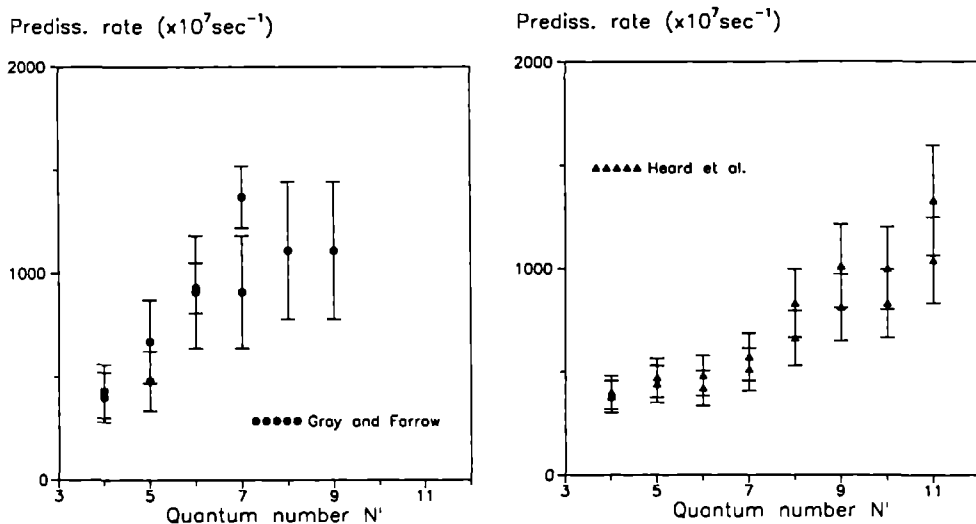


Figure 2.19 Excited state predissociation rates plotted as a function of rotational quantum number N' . Left Data obtained from optical-optical double-resonance linewidth measurements [11] Right Data obtained from laser-induced fluorescence detection in a low-pressure flame [12]

figure 2.19 Both F_1 and F_2 levels from $N'=4$ to $N'=11$ are shown. The data from Gray and Farrow are absolute rates, the relative rates of Heard et al. are calibrated by equalizing the values of $N'=4$. A discrepancy at $N'=6$ and 7 complicates a unique assignment of the predissociation rates. We have tried to determine temperatures using either one of these data sets in a calibrated adiabatic flame using a tunable KrF excimer laser. We did not obtain a reliable value for the flame temperature. Gray and Farrow's data are not measured for the higher rotational quantum numbers, which appear in the KrF laser tuning range. Only four lines are selected and this number is too small to determine a temperature with enough accuracy. Using Heard et al.'s data set eleven lines are selected. However, a proper Boltzmann plot was never measured from these experiments.

The adiabatic flame is well calibrated and temperatures are calculated for different stoichiometries and gas flow velocities. We have measured OH excitation spectra in a $0.8 \text{ mm} \times 0.6 \text{ mm}$ area at about 2 mm above the flame front. A temperature of $2000 \text{ K} \pm 150 \text{ K}$ is calculated using a one-dimensional flame model [32]. The line intensities in the excitation spectrum are

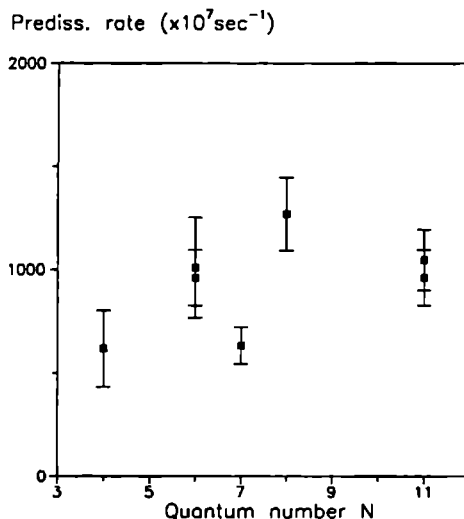


Figure 2.20 Predissociation rates, plotted as a function of rotational quantum number N' , obtained from a calibrated adiabatic flame using laser induced predissociative fluorescence of OH with a tunable KrF excimer laser

normalized and relative predissociation rates are calculated using eqn. 2.1. The rate for radiative decay is fixed. The results are shown in figure 2.20. Eight lines are not included due to too small line intensities or due to interfering O_2 resonances. The error in the rates is in the 15 to 20 % range, mostly determined by the inaccuracy of the flame temperature calculation. The relative values are given an absolute scale to best match the absolute rates measured by Gray and Farrow. In principal, this experiment is not different of that of Heard et al. The difference lies in the way of calibrating the flame temperature to start with. Our data show an agreement with the linewidth measurements of Gray et al. whereas only little overlap is found for the rates of the SRI group (as expected, because our Boltzmann plots never fitted a temperature). Using our data set temperatures are determined with an accuracy of 13%.

2.4.3 Comparison of predissociation rates

The three different experiments show clearly the rotational-level dependent predissociation predicted theoretically. Also the expected increase with increasing rotational quantum number is observed in all three studies. Apart from these crude similarities, large deviations, non-tolerable

for temperature determinations, are observed. As far as our own experiment is concerned, some reasons, already indicated in the previous section, can be given. In our experiment we use an atmospheric flame and the fluorescence signal, transmitted through a UG-11 filter, contains collision-induced VET. It is not clear what fraction of the fluorescence signal is due to VET, nor is it known how these collisional energy transfer processes deteriorate the signal observed or the temperatures determined from them. This must be checked in the near future. Filtering by narrowband filters would eliminate the detection of VET, but, as discussed above, care should be taken in selecting a proper center wavelength of the filter. In addition, problems arise with polarization effects when single P, Q or R lines are detected in fluorescence. In all three experiments the spectral density of the laser is reduced to minimize or exclude depletion of the probed ground state level. At atmospheric pressures the rotational energy transfer in the ground state of the molecule can become large, but to our knowledge no experimental data are yet available. This also needs more detailed investigations. The crucial point in the experiment by Heard et al is their flame temperature determination using the $0 \leftarrow 0$ transition. A possible problem in the experiment by Gray and Farrow lies in complexity of the Voigt profile line shape fitting and in the extrapolation to zero laser intensity of the homogeneous linewidths from the OODR spectra.

We have learned many new aspects of quantitative temperature determinations in flames using laser-induced predissociative fluorescence. At this stage little is yet known on vibrational energy transfer in the electronically excited state and on rotational energy transfer in the ground state of the molecule. Both processes will be studied in more detail for quantitative temperature determinations at atmospheric pressures.

Frequency calibration in the ArF laser tuning range using laser-induced fluorescence of NO

Michel Versluis, Maarten Ebben, Marcel Drabbels and J. J. ter Meulen

University of Nijmegen, Department of Molecular and Laser Physics
Toernooiveld, NL-6525 ED Nijmegen, the Netherlands

A frequency calibration in the tuning range of the ArF excimer laser near 193 nm is performed. Different electronic spectra of nitric oxide are measured by laser-induced fluorescence (LIF) detection in a cell and in an oxy-acetylene flame. Excitation spectra are measured with a frequency doubled and Raman shifted dye laser system and with a tunable ArF excimer laser with a modified configuration. A list of absolute frequencies of the $B^2\Pi(v'=7) \leftarrow X^2\Pi(v''=0)$ and $D^2\Sigma^+(v'=0) \leftarrow X^2\Pi(v''=1)$ transition in this spectral region is given, including a more comprehensive assignment of the latter excitation spectrum.

3.1 Introduction

In the past few years there has been a growing interest in the application of tunable excimer lasers in combustion [17, 18, 24] and flow diagnostics [14]. Because of its high power, high repetition rate and high spectral brightness the laser allows for density and temperature field measurements at atmospheric, or even higher, pressures [1, 47]. In addition, new spectroscopic information on diatomic molecules [18, 20, 21] is gathered in the tuning range of the ArF excimer laser, a frequency region that is accessible to conventional dye lasers only with a great effort. For spectroscopic reasons the need for a frequency calibration is evident. This can be achieved by absorption, fluorescence or ionization in a gas sample contained in a calibration cell. Several stable molecules, like e.g. O_2 , H_2 , CO or NO , have electronic one- or two-photon transitions in this frequency region. Both resonance-enhanced multiphoton ionization (REMPI) [15] and laser-induced fluorescence (LIF) [39] can be applied as detection techniques for H_2 . Five rotational lines of the $E,F \leftarrow X$ transition lie within the gain profile of the ArF excimer laser. The $B^3\Sigma_u^-(v'=4)$ state of O_2 , reached by excitation in the Schumann-Runge band, is a predissociating state. Consequently, the lines are broadened to several wave numbers, making them less suitable for calibration. CO , as Meijer et al. [20] pointed out, is well suited for frequency calibration, because the transitions of this molecule are accurately measured and well tabulated. Typically, 30 mJ of laser output however, is required for measurement of LIF of the forbidden $a^3\Pi(v'=2) \leftarrow X^1\Sigma^+(v''=0)$ transition.

NO has three different electronic transitions ($A^2\Sigma^+(v'=3) \leftarrow X^2\Pi(v''=0)$, $D^2\Sigma^+(v'=0) \leftarrow X^2\Pi(v''=1)$, $B^2\Pi(v'=7) \leftarrow X^2\Pi(v''=0)$) lying within the wavelength region near 193 nm. Both LIF [19] and resonant two-photon ionization (R2PI) [26] can be applied in a cell experiment. Recently, Robie et al. [26] measured the R2PI spectrum of NO for frequency calibration and determination of the bandwidth of the laser. The accuracy of the line positions is, however, limited to $\pm 0.5 \text{ cm}^{-1}$ because of the alinearity of their frequency scales. The assignment is confusing because of the high density of lines in the spectrum. The ionization from the A and D state is efficient, but the ground-state levels are not well populated at room temperature. The transitions that can be excited by the ArF laser start from $J = 30.5$ for the $A \leftarrow X$ band and from a vibrationally excited level for the $D \leftarrow X$ transition. Consequently, the overall ion yield is low in both cases. LIF spectroscopy of these states is difficult for the same reason. The ionization cross section from the B state is rather small [48], making laser-induced fluorescence from this state most preferable in a cell experiment. The $D \leftarrow X$ transition can also be used for calibration if the NO molecules are measured in a flame. The $B \leftarrow X$ and $A \leftarrow X$ transitions are not observed in the flame experiment, because of quenching of the fluorescence, which is due to the relatively long lifetime of the excited states and the low abundance of NO in the flame. We choose to apply laser-induced fluorescence in the flame experiment. For both the $B \leftarrow X$ and $D \leftarrow X$ transitions we calibrate the line positions. A new assignment of the rotational lines belonging to the $D \leftarrow X$ transition is obtained.

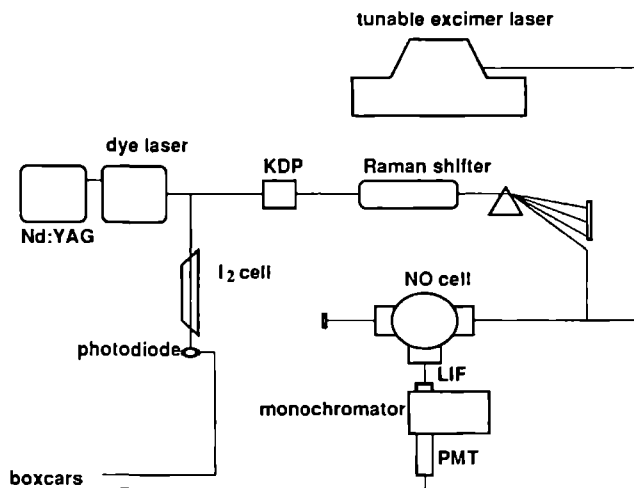


Figure 3.1 The experimental setup for a frequency calibration near 193 nm

3.2 Experimental Setup

The calibration cell consists of a stainless steel vacuum chamber equipped with two Suprasil I windows (diameter 50 mm \times 5 mm). A diaphragm and light baffles control the size of the laser beam and reduce stray light in the cell. NO is made to flow continuously through the cell. The flow is controlled by a needle valve. The pressure in the cell is 100 mTorr. The fluorescence is dispersed by a 1/8 m monochromator (Oriel 77250, 1200 g/mm) with a maximum resolution of 1 nm. The transmitted photons are measured with a photomultiplier (EMI 9863 B 350 AC) and the signals are time averaged with a boxcar integrator (SRS 250). Light can be detected for wavelengths above approximately 280 nm, so no interference of resonant laser light influences the measurements.

Flame spectra were measured in an oxy-acetylene welding torch. The laser-induced fluorescence of abundant NO is collected from a region 1-2 cm above the flame front by means of a Suprasil I lens. The fluorescence is focused onto the entrance slit of a 0.25-m-focal-length monochromator (Jobin Yvon M25, 610 g/mm, 1 nm resolution) and is detected by a photomultiplier (EMI 9635 QB). The signals are time averaged with a second boxcar integrator (SRS 250). The flame and the cell spectra are recorded simultaneously on a strip chart recorder.

The spectra are recorded by using two laser systems. The actual calibration spectra are taken by Raman shifting a frequency-doubled tunable dye laser. The output of a Nd:YAG laser (Quintel

681-10C) is doubled to pump a dye laser (Continuum TDL 60) operating on Rhodamine 6G. The dye laser beam is frequency doubled in a KDP crystal delivering typically 30 mJ of pulse energy. This UV light is then focused with an $f = 150$ mm Suprasil I lens into a stainless-steel cell containing 15 bars of hydrogen, generating several Stokes and Anti-Stokes beams. The fourth Anti-Stokes is directed to the calibration cell by a Suprasil I prism. Less than $50 \mu\text{J}$ of tunable 193 nm radiation is used to irradiate the gas sample contained in the calibration cell. A part of the fundamental dye laser beam is used for I_2 absorption measurements. In this way the frequency of the VUV laser light is calibrated by using iodine frequency tables [49]. Because we want to calibrate our spectra to an accuracy of 0.1 cm^{-1} the H_2 Raman shift has to be accurate within 0.02 cm^{-1} . The value of the Raman shift shows a pressure dependence [50]. We adopted the value of 4155.21 cm^{-1} , in agreement with the constants given in reference [50]. Five lines of the $\text{B} \leftarrow \text{X}$ transition, three at the blue end and two at the red end of the spectrum, are measured together with the iodine lines.

The spectra are also taken with a tunable ArF excimer laser (Lambda Physik EMG 150 MSCT). The laser consists of two discharge cavities. In the normal setup one cavity is used as an oscillator. In combination with beam-expanding prisms and a diffraction grating, a diaphragm and a circular aperture of 2 mm diameter in the resonator cavity are used for the generation of narrowband radiation. By tilting the grating and moving its reflection along the aperture the oscillator, we can tune the frequency of the oscillator within the gain profile of the laser. The other discharge cavity is used as an amplifier. The relatively small oscillator beam is expanded and amplified by means of unstable resonator (or Cassegrain) optics. Typically 100 mJ per pulse tunable narrowband radiation is achieved for ArF-optimized excimer lasers. The laser is tunable over 200 cm^{-1} with a bandwidth of 0.4 cm^{-1} . The use of unstable resonator optics results in a beam divergence of less than 0.2 mrad .

The amplification stage has some disadvantages, however, for two dimensional fluorescence imaging and for spectroscopic reasons. In the first place the application of Cassegrain optics results in a circular (diameter 2.5 mm) intensity dip in the middle of the beam cross section. The spatially inhomogeneous distribution of pulse energy in a laser sheet, produced by cylindrical lenses, will result in misleading planar fluorescence images. Second, the amplifier discharge cavity equipped with unstable resonator optics is a lasing medium on its own, typically delivering 50 mJ per pulse broadband energy when not injected by narrow-band oscillator radiation. If, because of decreasing oscillator power, the amplifier is not completely locked to the oscillator, the laser output will be a combination of narrowband and broadband radiation making spectroscopy, both LIF and REMPI, more complicated. This artifact occurs on both red and blue ends of the tuning range and every time the oscillator hits an oxygen absorption line belonging to the Schumann-Runge $\text{B}^3\Sigma_u^-(v'=4) \leftarrow \text{X}^3\Sigma_g^-(v''=0)$ band. The spectral density of the broadband light is still 0.1 mJ/cm^{-1} , enough to induce a lot of additional (and therefore confusing) fluorescence. Removing the unstable resonator optics and guiding a wide oscillator beam in single pass through the amplifier discharge tube would eliminate this problem.

Research by Wodtke et al [18] describes insertion of rectangular apertures in the oscillator resonator of a Lambda Physik EMG 150 EST, where cylindrical lenses expand the oscillator beam before injection into the amplifier

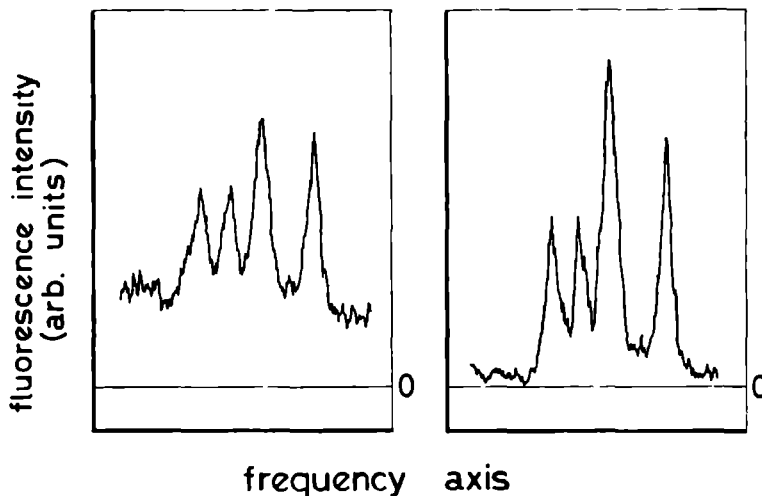


Figure 3.2 A part of the $\text{NO } D^2\Sigma^+ \leftarrow X^2\Pi$ spectrum measured with two different configurations of the excimer laser. The left excitation spectrum is measured with Cassegrain optics. The right spectrum is measured without the unstable resonator optics.

We find that removal of the diaphragm and the circular aperture does not influence the bandwidth of the oscillator. By using beam-expanding prisms of 30 mm height, one can generate an oscillator beam (dimensions 22 mm \times 4 mm) delivering 1 mJ per pulse with a bandwidth of 0.4 cm^{-1} . This beam is then passed through the amplifier discharge cavity yielding at maximum 40 mJ per pulse tunable narrowband radiation. The tuning range increases up to 300 cm^{-1} . In combination with the absence of broadband laser emission this modified set-up is more suited for spectroscopic measurements. This is demonstrated in figure 3.2, where the same rotational lines of the $\text{NO } D^2\Sigma^+(v'=0) \leftarrow X^2\Pi(v''=1)$ transition near 51650 cm^{-1} are measured with the two different configurations of the ArF laser. The left-hand spectrum is measured with Cassegrain (unstable resonator) optics, whereas the right-hand one is measured without the unstable resonator optics. Notice that the offset in the left-hand spectrum is due to excitation of the NO molecules by broadband radiation and therefore it depends on the pulse-to-pulse fluctuations of the power. Moreover, it depends on the fluctuating NO concentration in

the flame. Because the intensity dip originating from the unstable resonator optics is no longer present, one can generate laser sheets with a homogeneous energy distribution suited for planar fluorescence imaging.

3.3 Results and Discussion

All spectra in this experiment are measured without Cassegrain optics. A part of the $\text{NO } B^2\Pi(v=7) \leftarrow X^2\Pi(v=0)$ spectrum, measured with the tunable excimer laser, is shown in figure 3.3.

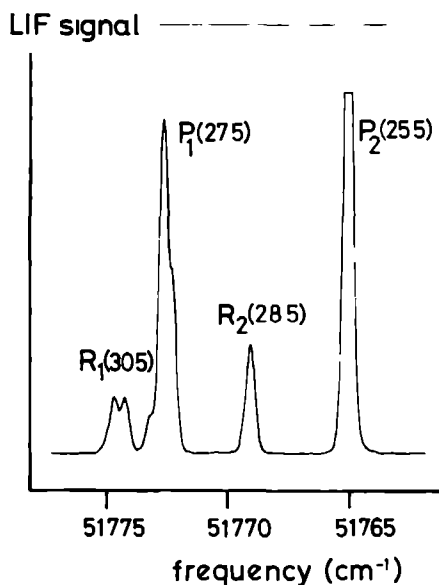


Figure 3.3 A part of the $\text{NO } B^2\Pi(v=7) \leftarrow X^2\Pi(v=0)$ spectrum near 51770 cm^{-1}

The linewidth of 0.38 cm^{-1} is determined by the bandwidth of the laser. The monochromator is set to transmit the fluorescence around 337 nm . The monochromator has a resolution of approximately 15 nm . The identification of the rotational lines is also indicated in the figure. The splitting of the $R_1(305)$ line at 51775 cm^{-1} is due to the Λ doublet splitting in the ground state. The splitting grows linearly with the quantum number J . No splitting is observed in the F_2 manifold because $^2\Pi_{3/2}$ states couple only weakly with the electronically excited Σ states.

The $B \leftarrow X$ (lower) and the $D \leftarrow X$ (upper) excitation spectra are shown in figure 3.4. These spectra are recorded simultaneously during the frequency scan. Notice the absence of the

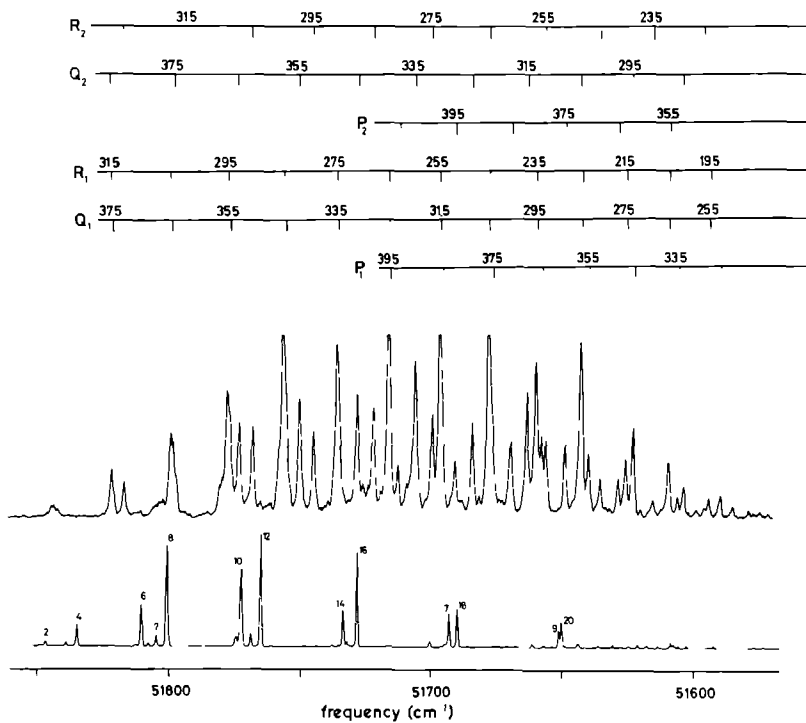


Figure 3.4 Upper part The excitation spectrum of the $D^2\Sigma^+(v'=0) \leftarrow X^2\Pi(v=1)$ transition of natural abundant nitric oxide measured in an oxy-acetylene flame. Four lines are truncated due to the limited dynamical range of the strip chart recorder. Lower part The excitation spectrum of the $B^2\Pi(v=7) \leftarrow X^2\Pi(v'=0)$ transition of NO measured in a cell at a pressure of 100 mTorr. The numbers of the labeled lines correspond to the tabulated frequencies in Table 3.1.

broadband 'wings' on the extreme sides of the tuning range. Because the linearities of both the grating stepper motor and the strip chart recorder are not known, the calibration lines are fitted to a polynomial function.

We find that the horizontal axis is linear with the frequency within the present accuracy. The lines of the $B \leftarrow X$ transition lying within the tuning range of the ArF laser are tabulated in Table 3.1. The observed error of the line positions is 0.2 cm^{-1} .

For the observation of the $\text{NO } D^2\Sigma^+(v'=0) \leftarrow X^2\Pi(v''=1)$ excitation spectrum the monochromator is set to transmit the $D(v'=0) \rightarrow X(v''=3)$ fluorescence at 208 nm only. The monochromator is set to the maximum resolution (1 nm) in order to prevent detection of O_2 fluorescence, which is induced in the same spectral region. All lines are assigned to P, Q and R lines of the $D(v'=0) \leftarrow X(v''=1)$ transition and are tabulated in Table 3.2 together with their assignments and calculated frequencies. It must be noted that reference [19] contains some misassigned lines. The calculation is performed in the following way. The energy values of the $D(v=0)$ state are given by the usual expression

$$F_1(N) = I_0 + B N(N+1) - D N^2(N+1)^2 + \frac{1}{2} \gamma N \quad (3.1)$$

$$I_2(N) = T_0 + B N(N+1) - D N^2(N+1)^2 - \frac{1}{2} \gamma(N+1) \quad (3.2)$$

where T_0 , B and D are taken from reference [51] and [52]. The ground state energy values in the $v''=1$ are taken from reference [53]. The N -doublet splitting is ignored. Frequencies are calculated by subtracting the energy values of both electronic states. The agreement between measured and calculated lines is good within the indicated error (0.2 cm^{-1}). Some lines are overlapping, which makes it difficult to determine the exact center of the line position.

3.4 Summary

We have performed a frequency calibration in the tuning range of the ArF excimer laser near 193 nm. A list of absolute frequencies of the $B^2\Pi(v'=7) \leftarrow X^2\Pi(v''=0)$ and the $D^2\Sigma^+(v'=0) \leftarrow X^2\Pi(v''=1)$ transitions in NO is given. Both electronic transitions can be used as a calibration in this spectral region. Whether a cell or a flame experiment is used depends on the application.

	Observed Frequency	Transition
1	51849 7	R ₁ (28 5)
2	51847 8	P ₁ (25 5)
3	51839 6	R ₂ (26 5)
4	51835 6	P ₂ (23 5)
5	51813 2	R ₁ (29 5)
6	51810 9	P ₁ (26 5)
7	51805 2	R ₂ (27 5)
8	51801 0	P ₂ (24 5)
9	51774 7	R ₁ (30 5)
10	51772 7	P ₁ (27 5)
11	51769 1	R ₂ (28 5)
12	51765 2	P ₂ (25 5)
13	51734 8	R ₁ (31 5)
14	51733 0	P ₁ (28 5)
15	51731 6	R ₂ (29 5)
16	51727 6	P ₂ (26 5)
17	51692 0	P ₁ (29 5)
18	51689 2	P ₂ (27 5)
19	51649 8	P ₁ (30 5)
20	51648 7	P ₂ (28 5)

Table 3.1 P and R lines of the $B^2\Pi (v'=7) \leftarrow \Lambda^2\Pi (v''=0)$ transition of NO observed within the tuning range of the Λ IF laser (in cm^{-1}). The numbers correspond to the labeled lines in figure 3.1. The observed error is 0.2 cm^{-1} . The notation is $\Delta J_{\Gamma} (J')$.

Table 3.2 (next page) Absolute frequencies of the $D^2\Sigma^+ \leftarrow \Lambda^2\Pi$ transition of NO observed in the tuning range of the ArF excimer laser (in cm^{-1})

a notation $\Delta J_F''(J'')$

b not observed because of absence of laser action due to an intra cavity C atom absorption

c not calculated because energy levels in ref [53] are not calculated for such high J values

Observed Frequency	Transition ^{a)}	Calculated Frequency
51819 5	R ₁ (31 5)	51819 7
819 5	Q ₂ (38 5)	819 6
819 5	Q ₁ (37 5)	818 9
815 1	R ₂ (32 5)	815 0
796 8	R ₁ (30 5)	797 0
796 8	Q ₁ (36 5)	796 3
51795 3	Q ₂ (37 5)	794 9
not obs ^{b)}	R ₂ (31 5)	790 0
51775 1	R ₁ (29 5)	775 0
775 1	Q ₁ (35 5)	774 4
771 0	Q ₂ (36 5)	770 8
766 0	R ₂ (30 5)	765 6
753 5	R ₁ (28 5)	753 6
753 5	Q ₁ (34 5)	753 1
747 8	Q ₂ (35 5)	747 4
741 9	R ₂ (29 5)	741 8
732 5	R ₁ (27 5)	732 8
732 5	Q ₁ (33 5)	732 4
725 1	Q ₂ (34 5)	724 5
718 8	R ₂ (28 5)	718 6
712 5	R ₁ (26 5)	712 7
712 5	Q ₁ (32 5)	712 4
712 5	P ₁ (39 5)	51712 0
709 3	P ₂ (40 5)	not calc ^{c)}
702 5	Q ₂ (33 5)	51702 2
696 2	R ₂ (27 5)	696 0
692 8	R ₁ (25 5)	693 3
692 8	Q ₁ (31 5)	693 0
692 8	P ₁ (38 5)	51692 1
687 4	P ₂ (39 5)	not calc ^{c)}
51680 7	Q ₂ (32 5)	51680 5

Table 3.2

Observed Frequency	Transition ^{a)}	Calculated Frequency
51674 3	R ₁ (24 5)	51674 4
674 3	Q ₁ (30 5)	674 3
674 3	R ₂ (26 5)	674 0
673 0	P ₁ (37 5)	672 8
665 8	P ₂ (38 5)	665 7
659 6	Q ₂ (31 5)	659 5
656 2	R ₁ (23 5)	656 3
656 2	Q ₁ (29 5)	656 2
654 2	P ₁ (36 5)	654 1
652 6	R ₂ (25 5)	652 6
644 8	P ₂ (37 5)	644 9
638 9	Q ₂ (30 5)	639 0
638 9	R ₁ (22 5)	638 7
638 9	Q ₁ (28 5)	638 7
636 0	P ₁ (35 5)	636 1
631 6	R ₂ (24 5)	631 7
624 6	P ₂ (36 5)	624 7
621 6	Q ₁ (27 5)	621 9
621 6	R ₁ (21 5)	621 8
618 9	Q ₂ (29 5)	619 1
618 9	P ₁ (34 5)	618 7
611 4	R ₂ (23 5)	611 5
605 3	Q ₁ (26 5)	605 7
605 3	R ₁ (20 5)	605 6
605 3	P ₂ (35 5)	605 1
601 9	P ₁ (33 5)	601 9
599 6	Q ₂ (28 5)	599 8
591 7	R ₂ (22 5)	591 9
589 5	Q ₁ (25 5)	590 2
589 5	R ₁ (19 5)	590 0
51585 3	P ₁ (32 5)	51585 8

Table 3 2 (continued)

Intra-cavity C atom absorption in the ArF laser tuning range

Michel Versluis and Gerard Meijer

University of Nijmegen, Department of Molecular and Laser Physics
Toernooiveld, NL-6525 ED Nijmegen, the Netherlands

Our tunable ArF excimer laser has no laser action in a region around 51790 cm^{-1} due to an intra-cavity $3^1\text{P} \leftarrow 2^1\text{D}$ C atom absorption. This has a direct consequence for the interpretation of the photodissociation processes in CO at 193 nm.

The photodissociation of carbon monoxide at 193 nm has received great experimental interest in recent years [54, 55, 56, 57, 58, 20]. The resonant excitation of the spin-forbidden $a^3\Pi(v'=2) \leftarrow X^1\Sigma^+(v''=0)$ transition of CO by the ArF excimer laser at 193 nm, followed by absorption of at least two additional 193 nm photons, leads to the dissociative production of C(3^1P) atoms, which fluoresce at 247.9 nm to the C(2^1S) state. This is schematically indicated in figure 4.1. There are two possible dissociation channels leading to the production of 3^1P carbon atoms: (a) by a one-photon dissociation of the $a^3\Pi$ state, forming atomic carbon C(2^1D), followed by the resonant excitation to the C(3^1P) state at 193.1 nm or (b) by a two-photon dissociation of the $a^3\Pi$ state whereafter C(3^1P) atoms are directly formed. Many studies [54, 55, 56, 58] follow the pathway according to case (a), where the coincident overlap of the atomic carbon transition with the ArF gain profile is needed to produce 3^1P carbon atoms.

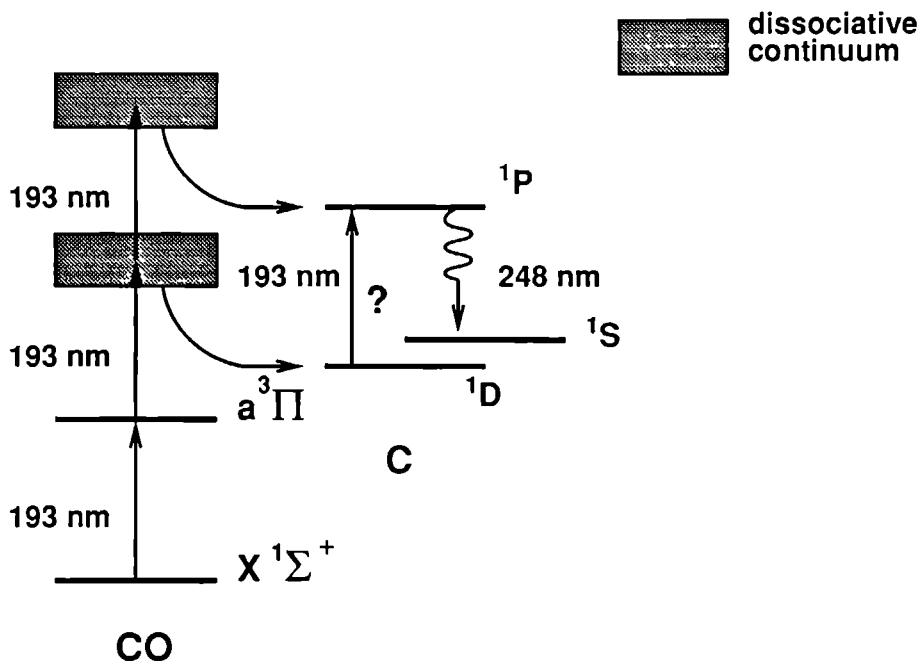


Figure 4.1 : The photodissociation process of carbon monoxide.

In this note we want to draw the reader's attention to the possible occurrence of an intra-cavity absorption in the discharge cavity of the ArF excimer laser at exactly the C: $3^1P \leftarrow 2^1D$ transition frequency. In our tunable ArF excimer laser (Lambda Physik EMG 150 MSCT) an intra-cavity absorption prevents laser action around 51790 cm^{-1} . The absorption line is as broad

as 2.5 to 10 cm^{-1} , depending on the quality of the laser filling. Lasing could never be achieved at the center frequency. By calibrating the laser against NO [59], the center frequency of the absorption was determined to be $51789.2 \pm 0.2 \text{ cm}^{-1}$. The absorption is located near two well known oxygen resonances ($\text{O}_2 \text{ B}^3\Sigma_u^-(v'=4) \leftarrow \text{X}^3\Sigma_g^-(v''=0)$ P(15) and R(17) at 51783.6 and 51788.3 cm^{-1} [60], respectively), and has previously been confused with these. The absorption is clearly seen only when the oscillator output is monitored directly, e.g. when the laser is used in the so-called amplified oscillator mode. In this mode the unstable resonator optics of the amplifier are removed and the oscillator beam is directed in a single pass through the amplifier cavity [59]. When the laser is used in the standard mode the cessation of laser action in the oscillator does not appear in the total output energy of the laser, because the amplifier itself delivers 50 mJ of broadband energy when not injected by sufficient oscillator power. In the amplified oscillator mode the power drops to zero when no oscillator power is available.

We believe that the absorption is due to the strong $3^1\text{P} \leftarrow 2^1\text{D}$ transition of the meta-stable carbon atom at 51789.18 cm^{-1} . This absorption line has been reported before under near lasing conditions of a broadband ArF excimer laser [61]. The $3^1\text{P} \leftarrow 2^1\text{D}$ transition is one of the strongest C atom transitions, with a transition probability of $3.7 \times 10^8 \text{ s}^{-1}$ [62]. Several ppb of meta-stable ^1D carbon atoms in the discharge cavity are therefore enough to defeat laser action at this frequency.

The output power of the tunable ArF excimer laser (bandwidth 0.4 cm^{-1}) near the C atom absorption line is shown in the upper part of figure 4.2. For this the beam path to the detector and the intra- and extra-cavity components of the laser are flushed with nitrogen to decrease the intensity of the oxygen absorption lines. The C atom absorption is clearly seen in the figure. The $\text{O}_2 \text{ B}^3\Sigma_u^-(v'=4) \leftarrow \text{X}^3\Sigma_g^-(v''=0)$ P(15) and R(17) transitions are indicated in the upper part of the figure. This plot is taken with a fresh gas filling. After 3×10^4 laser shots at 10 Hz the absorption line appears much broader as is seen in the lower part of figure 4.2. The carbon atoms may be formed in the discharge from impurities in the filling gas or from other materials in the discharge tube. The filling gas is composed of 90% Helium (gas purity 99.99%), which contains several ppm of CO, CO_2 and hydro-carbons. In the discharge these molecules can dissociate to produce $\text{C}(2^1\text{D})$ atoms which give rise to the absorption line. Contamination by oil, originating from the rotary pump used to evacuate the laser tubes, may be an additional source of the meta-stable C atoms.

Although not always recognized as such, the strong C atom absorption is reflected in excitation spectra measured with the tunable excimer laser [20, 21]. It should be explicitly noted that resonant $3^1\text{P} \leftarrow 2^1\text{D}$ excitation of meta-stable $\text{C}(2^1\text{D})$ atoms is not possible with our tunable excimer laser, since there are no ArF laser photons available at the transition frequency.

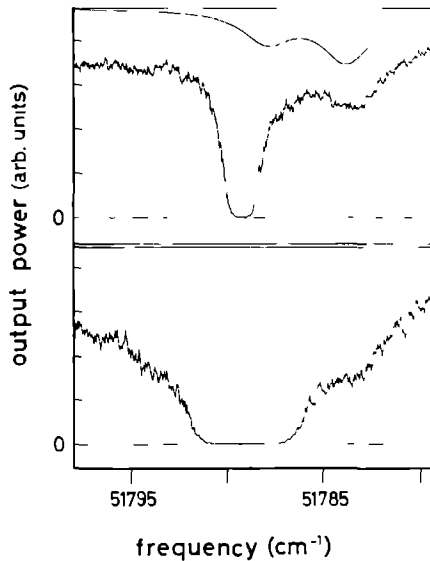


Figure 4.2 : Upper : The output power of the tunable ArF laser near 51790 cm^{-1} with a fresh gas filling. The strongest absorption, due to the carbon atom $3^1P \leftarrow 2^1D$ transition, has a linewidth of 2.6 cm^{-1} . The calculated line profile of the O_2 , $B^3\Sigma_u^- (\nu'=1) \leftarrow X^3\Sigma_g^- (\nu''=0)$ P(15) and R(17) absorption lines are indicated in the upper part of the figure. The linewidth of 3.9 cm^{-1} is determined by the predissociation lifetime of the $B^3\Sigma_u^- (\nu'=4)$ state. The linewidth of the ArF laser is 0.1 cm^{-1} . Lower : The output power after 3×10^4 laser shots. The absorption linewidth has increased to 8.2 cm^{-1} , due to an increased number of carbon atoms.

Laser-induced fluorescence imaging in a 100 kW natural gas flame

Michel Versluis, Maarten Boogaarts, Robert Klein-Douwel, J. J. ter Meulen, W. Leo Meerts and Gerard Meijer

University of Nijmegen, Department of Molecular and Laser Physics
Toernooiveld, NL-6525 ED Nijmegen, the Netherlands

Bert Thus, Wiggert de Jongh and Ad Braam

KEMA, Department of Applied Physics
Utrechtseweg 310, NL-6812 AR Arnhem, the Netherlands

A tunable excimer laser at 248 nm (KrF) and 193 nm (ArF) has been used to monitor two-dimensional OH and NO distributions in the turbulent flame of a 100 kW natural gas burner. Spatially resolved fluorescence (spatial resolution better than 1.0 mm) from a 20 cm × 20 cm area is collected under single shot conditions. We describe the problems encountered when laser-induced fluorescence imaging techniques are applied to large scale flames. Special experimental arrangements, imposed by the turbulent behavior of the flame we used, are also described.

5.1 Introduction

During the last three decades the reduction of pollutants in combustion processes has received great interest [63]. Different diagnostic methods, e.g. emission spectroscopy [2] and the line-reversal method [3], have been applied in order to characterize temperatures of flames and densities of combustion species. About 15 years ago laser diagnostics entered the field of combustion with techniques as Laser-Induced Fluorescence (LIF) [7] and Coherent Anti-Stokes Raman Scattering (CARS) [7]. Recently other non-linear techniques such as degenerate four-wave mixing [64, 65] have been added to this list. Rayleigh scattering [66] and spontaneous Raman scattering in combination with LIF [6] are promising spectroscopic tools for flame diagnostics. So far, most techniques have been well experimented on at laboratory scale flames. Less experience has been obtained with the application of these techniques to larger scale flames, as for instance to flames in utility boilers of power plants.

In the Netherlands all power plants together are responsible for 15% of the total NO_x release in the Dutch atmosphere [67]. The combustion process in a utility boiler of a power plant, and its almost inevitable exhaust of nitric and sulfuric oxides, is mainly determined by the characteristics of the flames, such as temperature, species concentration distributions and local stoichiometry. The visualization of nitric oxide formation in the combustion process is of utmost importance for determining the optimum condition of the burner parameters, such as swirl and stoichiometry in order to develop a better, that is to say a cleaner, low NO_x -burner [68].

Laser-Induced (Predissociative) Fluorescence (LI(P)F) is one of the most sensitive diagnostics techniques used in combustion, as has been demonstrated by various groups [17, 69, 24, 70, 71]. The detection of laser-induced predissociative fluorescence of OH [17] has an important advantage over detection of 'normal' LIF of OH, because of its lack of collisional quenching at atmospheric pressures. When saturation of the electronic transition is avoided [41], LIPF gives the possibility of measuring quantitative densities and temperatures, even in large two dimensional areas. When OH is excited to the $A^2\Sigma^+(v=3)$ state with a tunable KrF excimer laser at 248 nm, the off-resonant fluorescence to unoccupied states is monitored, so there are no problems of fluorescence reabsorption [17]. The excimer lasers can work at a repetition rate of 50 Hz and the imaging of fluorescence with highly sensitive UV cameras with gated image intensifiers yield the opportunity to perform on-line measurements, e.g. changes of the burner configuration or of the burner conditions on the NO distribution are directly observed on the video monitor.

In this article we present two-dimensional laser-induced fluorescence measurements in a 100 kW natural gas flame. We have successfully monitored the OH and NO distributions in a large area with a tunable excimer laser operating on KrF and ArF, respectively, in a single laser pulse. This article describes, from an application-oriented point of view, the problems encountered when laser-induced fluorescence imaging techniques are applied to large scale flames. The complicated experimental conditions, among others caused by the turbulent behavior of the flame we used,

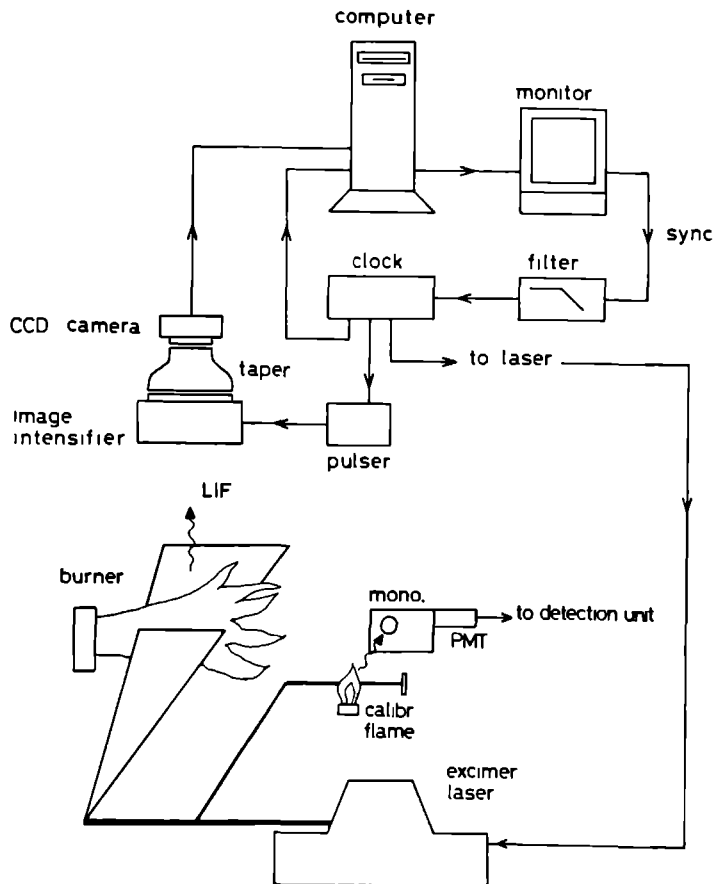


Figure 5.1 The experimental setup. See text for further details.

forced us to improvise and to improve our experimental apparatus. These special arrangements are also described.

5.2 Experimental Setup

The experimental setup is schematically given in fig. 5.1. The different parts will be discussed below.

5.2.1 100 kW burner

A photograph of the burner is shown in figure 5.2. The burner is a 1:100 down scaled model of a 10 MW burner used in natural gas fired utility boilers. The burner burns horizontally and is located in a furnace supplied with a chimney. The walls of the furnace are isolated with aluminum oxide. The internal dimensions of the furnace are $0.7 \times 0.7 \times 2.0$ meters. All experiments are done with a stretched natural gas flame. The flame has a typical diameter of 25 cm and its length is approximately 1.5 meters. The natural gas is composed of about 80% methane and 14% nitrogen, the remaining 6% consists of higher hydrocarbons, and also contains aromatic hydrocarbons like toluene and benzene [72].

The natural gas is injected in the primary combustion air flow via six small pipes, which have an effective opening of 4 mm^2 each. A secondary air flow is added to create a staged combustion [73]. The swirl of both air flows is adjustable in order to change the flame shape and to create an internal recirculation zone in the furnace. We have measured at different stoichiometries¹ ranging from 0.9 to 1.5. The diameter of the flame is varied from 15 to 50 cm. Depending on the stoichiometry, soot is formed in the flame. We tried to avoid soot formation in the detection region and adjusted the swirl and air supply accordingly. The furnace has optical access via quartz windows. There are two Suprasil I windows, a 100 mm diameter laser entrance window and a 200 mm \times 200 mm laser exit window. A 200 mm \times 200 mm air-cooled Dynasil window on top of the furnace is used to transmit laser-induced fluorescence. All windows are 3 mm thick. The windows have to be cleaned with alcohol after several hours of operation because of deposition of aluminum oxides from the inside. All windows heat up within 15 minutes of burner operation and start to radiate strongly. The detection window is cooled with air to prevent heating of the electronic camera system.

5.2.2 Laser system

A tunable excimer laser (Lambda Physik EMG 150 MSCT) is used to resonantly excite hydroxyl and nitric oxide radicals. The laser is operated on KrF (248 nm) for the OH measurements.

¹The stoichiometry is defined as the ratio of the actual oxygen concentration in the unburned mixture to the oxygen concentration at the stoichiometric point, i.e. for complete combustion of the fuel to CO_2 and H_2O [74].

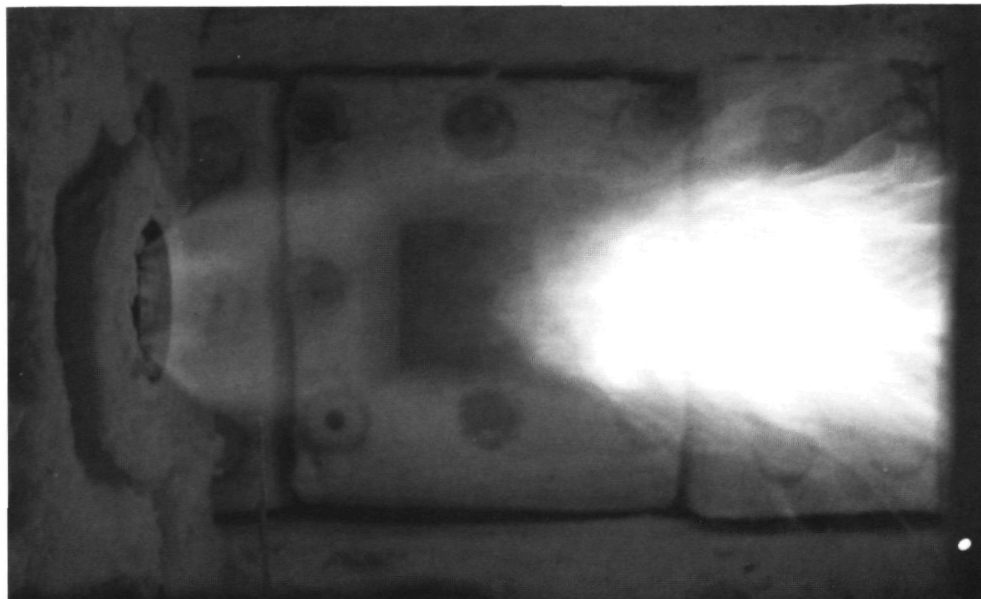


Figure 5.2 : Photograph of the natural gas flame. The natural gas is burned with air. The flame has a diameter of approximately 30 cm and a length of 1.5 m. The burner is located in a furnace with optical access via quartz windows. The laser exit window is visible behind the flame.

and on ArF (193 nm) for the NO measurements. The laser is grating-tunable over about 200 cm^{-1} within the gain profiles of the lasing transition of both exciplexes. The bandwidth of the laser is 0.4 cm^{-1} for KrF and 0.7 cm^{-1} for ArF. The laser is sometimes used in a modified setup without unstable resonator (or Cassegrain) optics to remove the fluorescence from species excited by the broadband background radiation of the laser [59]. However, often we need the full power of the laser and use Cassegrain optics in the amplifier. The output energy of the laser with unstable resonator optics is 250 mJ for KrF and 100 mJ for ArF. Tuning of the laser is performed by a stepper motor attached to a micrometer screw on the grating. To image a large part of the flame the rectangular laser output beam ($25\text{ mm} \times 5\text{ mm}$, divergence $< 0.2\text{ mrad}$) is transformed into a laser sheet of approximately 20 cm wide using a combination of spherical and cylindrical lenses. The thickness of the sheet depends on the imaging technique and the molecule under investigation ($500\text{ }\mu\text{m}$ for OH and 5 mm for NO).

5.2.3 Calibration flame

For calibration of the excitation wavelength, 10% of the laser beam is deflected by means of a MgF_2 beam splitter and directed into a small flame, where the excitation spectra of the species under investigation are recorded simultaneously. A monochromator-based system disperses the fluorescence and serves as a narrow-band filter. The monochromator (Jobin Yvon M25, 610 g/mm, resolution 1 nm) makes an unambiguous molecular assignment of the combustion species possible via detection of vibrationally resolved fluorescence [17]. A Bunsen burner (methane and air) is used as a calibration flame for the OH experiments, while an oxyacetylene welding torch is applied for the NO measurements. The laser passes through the flame approximately 2 cm above the flame front in both cases. The fluorescence of the specific molecules is collected with a $f = 100$ mm Suprasil I lens. The monochromator was set to transmit the OH $A^2\Sigma^+(v'=3) \rightarrow X^2\Pi(v''=2)$ off-resonant fluorescence at 295 nm in the OH experiment [17] and the NO $D^2\Sigma^+(v'=0) \rightarrow X^2\Pi(v''=3)$ off-resonant fluorescence at 208 nm in the NO experiment [19]. The transmitted photons are detected by a photomultiplier (EMI 9863 QB) and the signal is time averaged with a boxcar integrator with a gate width of approximately 50 ns. The averaged output of the integrator is recorded on a strip chart recorder.

5.2.4 Detection system

The fluorescence emitted in the direction of the top of the furnace is collected with either an $f = 105$ mm UV-transparent objective (Nikon, UV-Nikkor, $f/4.5$) or a 4" diameter $f = 100$ mm UV-graded fused silica lens. The fluorescence is focused on the photocathode of a gated image intensifier. Gating is performed with a modular gating unit suited for gating times down to 5 ns. Our gating time is typically 50 ns. The distance from the flame to the image intensifier is adjustable between 1.10 and 1.60 m. A CCD camera (Theta Electronic Systems) working in the European video rate mode (50 Hz) is attached to the phosphor screen of the image intensifier via a fiber optic taper. The video signal is digitized in a frame grabber (Matrox PIP-1024) installed in an IBM-compatible personal computer, equipped with an Intel 80386 microprocessor. Data processing and data acquisition is accomplished by home-written software. The video signal is simultaneously recorded on a VHS video recorder. Images are displayed on-line in a false color representation on a RGB color monitor. Processed images can be plotted on a color printer (HP-Printjet).

5.2.5 Triggering

The CCD-camera is a free running unit which can not be triggered externally. Therefore we choose the camera to trigger the experiment. The imaging board can be externally triggered by the synchronization pulse delivered by the camera. The output sync pulse of the board, attached also to the RGB monitor, is a 15 kHz pulse with a 'restart' pulse every 20 ms. The

latter pulse forces the monitor to start at the left-hand upper corner of the screen for a new image. This 50 Hz pulse is filtered from the 15 kHz sync pulse of the image processing board by means of a 500 Hz low-pass filter. The output of the filter is used to trigger a pulse/delay generator (SRS DG535). The pulse generator down converts the repetition rate to 10 Hz, a rate for optimum performance of the excimer laser. The output signals of the pulse generator are set to trigger the laser, the gating unit of the image intensifier and a serial port (RS-232) in the computer, which activates the software to process images for averaging and recording of spectra. This configuration allows to take synchronized snapshots from the camera²

5.3 Results

5.3.1 Small scale burner experiments

The results of the measurements in the 100 kW flame are better understood if compared to the results from smaller flames. Therefore we started our studies with 248 nm and 193 nm radiation in a Bunsen burner burning natural gas with air. The laser-induced fluorescence is monitored with the Nikon objective in front of the above described camera system. Bandpass filters are placed in front of the objective. A laser sheet of 200 μm thickness and 25 mm height is used for these measurements.

OH

Hydroxyl radicals (OH) are excited in a flame by inducing the $A^2\Sigma^+(v'=3) \leftarrow X^2\Pi(v''=0)$ transition at 248 nm with a tunable KrF excimer laser [17]. The off-resonant fluorescence from the excited state to, predominantly, the $v''=2$ in the ground state near 295 nm is monitored. Rayleigh and Mie scattered laser light is filtered with a 2 mm thick Schott UG-11 glass filter. If a sheet of a tunable KrF laser passes through a Bunsen burner several laser-induced processes occur as indicated in figure 5.3.

First, if the KrF laser is tuned to an OH resonance, fluorescence is induced on the outer sides of the flame. In addition, we observe the fluorescence of, so far, unidentified radicals produced shortly beyond the flame front. This fluorescence is not resonant with respect to the excitation laser wavelength and it is always present in the images. Furthermore, photodissociation of (aromatic) hydrocarbons, present in the natural gas, is detected via the fluorescence of the dissociation products. This fluorescence is located below the flame front where the gas has not burned yet. Between the radicals produced on the flame front and the OH radicals in the flame, a region without fluorescence is present. This fluorescence pattern, from the burner head, where we have unburned fuel, to the location where the combustion is completed, is seen back

²Due to the synchronization the frame transfer beat images have now also disappeared

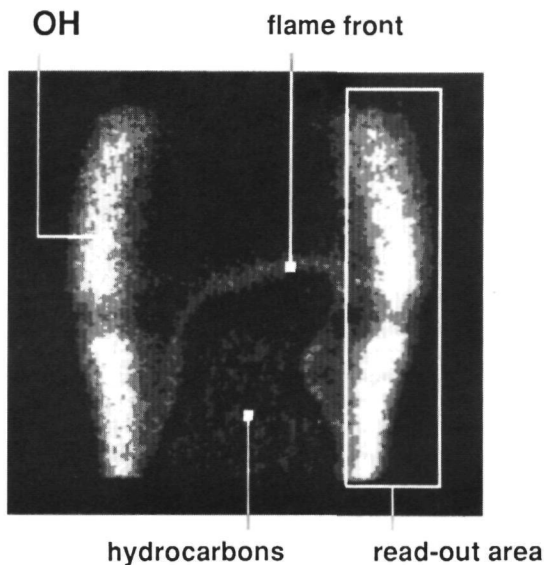


Figure 5.3 : A two dimensional KrF laser-induced fluorescence image from a Bunsen burner. The laser is tuned to the $P_2(8)$ resonance line of the OH: $A^2\Sigma^+(v'=3) \leftarrow X^2\Pi(v''=0)$ transition. Due to a hole in the beam profile of the KrF laser, less fluorescence is observed in the middle of the image. Further details are discussed in the text.

in every natural gas combustion process. Due to a hole in the beam profile of the KrF laser, less fluorescence is observed in the middle of the image.

With our software a rectangular area can be selected in the viewing region of the camera. The computer adds up all grey values within this specific region, and the sum value, if wanted averaged over several pictures, is plotted on the computer monitor or on a plotter. The laser can be tuned within its gain profile and an excitation spectrum of a molecule that is spatially separated from other molecules in the flame can be recorded this way. This is demonstrated in figure 5.4 where the intensity in the white rectangle indicated in figure 5.3 is measured as the laser is scanned. All lines can be assigned to the well-known OH transitions [17]. Laser-induced fluorescence of $O_2(v''=6)$ [17] is also seen in the figure, since vibrationally hot oxygen is located at the same position in the flame. This option turned out to be important to recognize which species fluoresce in more complex flame types. Two dimensional pictures of OH excited from different rotational energy levels in the ground state can be processed to give a two dimensional temperature profile of the flame. For a quantitative interpretation of absolute temperature mea-

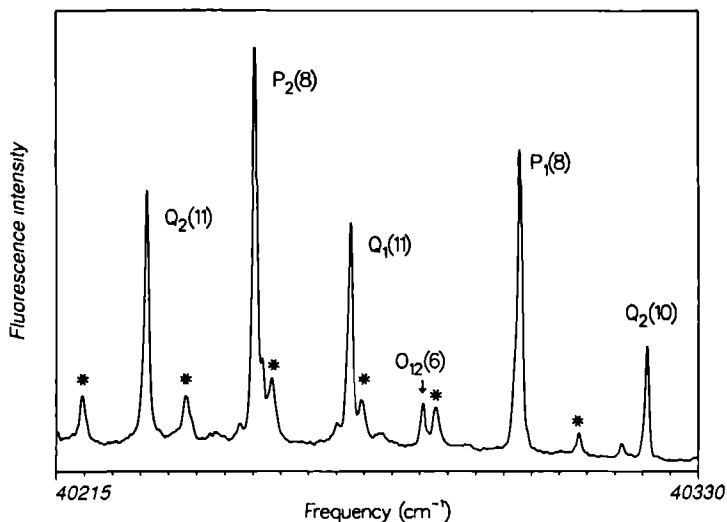


Figure 5.4 The $\text{OH } A^2\Sigma^+(v'=3) \leftarrow X^2\Pi(v''=0)$ excitation spectrum measured with the camera as described in the text. Laser induced fluorescence of $\text{O}_2(v''=6)$, denoted with asterisks, is also seen in the figure since vibrationally hot oxygen is located at the same position in the flame

measurements one should be aware of inherent difficulties, such as the variation of the predissociation lifetime with rotational quantum number [40]. In addition, the depletion of the ground state level population might complicate a quantitative analysis. The refilling through collisions of the probed level from neighboring levels during the laser pulse causes an undesired enhancement of the fluorescence signal. Saturation of the electronic transition should therefore be avoided. Calibration measurements, using recently measured absolute predissociation lifetimes of the excited rotational states of OH [41, 42], are in progress to determine the absolute temperature distributions.

NO

The NO molecules are detected in a flame by exciting the $\text{D}^2\Sigma^+(v'=0) \leftarrow X^2\Pi(v''=1)$ transition at 193 nm with a tunable ArF excimer laser [59, 19]. Off-resonant fluorescence from the excited state to the $v''=2,3,4$ in the ground state near 210 nm is monitored. Rayleigh and Mie scattered laser light is filtered with a highly reflective 193 nm/0° ArF laser mirror, transmitting

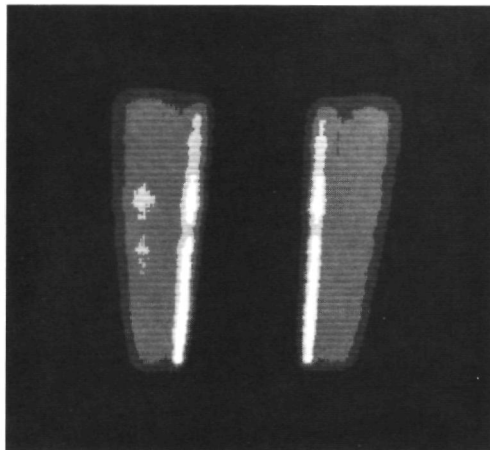


Figure 5.5 : A two dimensional ArF laser-induced fluorescence image from a Bunsen burner. The laser is tuned to the $R_1(26.5)$ and $Q_1(32.5)$ resonance line of the NO: $D^2\Sigma^+(v'=0) \leftarrow X^2\Pi(v''=1)$ transition. Nitric oxide is distributed homogeneously on both sides of the flame front.

$\lambda > 210$ nm. The non-resonant excitation of radicals on the flame front is more intense than the NO fluorescence. This can be seen in figure 5.5. The burner conditions are altered with respect to the OH measurements. The NO is distributed homogeneously on both sides of the flame front. The $D \leftarrow X$ transition of NO is saturated if the full power of the ArF laser is used to excite the molecules. The sheet can therefore be widened to excite more molecules, and hence, to increase the signal level.

5.3.2 100 kW burner experiments

OH

In the left-hand side of figure 5.6 a single laser shot image is shown when the laser is tuned to the $P_2(8)$ resonance line of the OH: $A^2\Sigma^+(v'=3) \leftarrow X^2\Pi(v''=0)$ transition. A laser sheet of $500 \mu\text{m}$ thickness and 20 cm width is used. The energy of the KrF laser is 100 mJ per pulse, leading to an excitation condition near saturation. The OH radicals are distributed in a narrow line along the flame front. The fluorescence is collected from a region as big as $16 \text{ cm} \times 14 \text{ cm}$ at about 8 cm from the burner head. Most prominent, however, is the broadband non-resonant fluorescence of the photodissociated hydrocarbons under the flame front as seen before in the

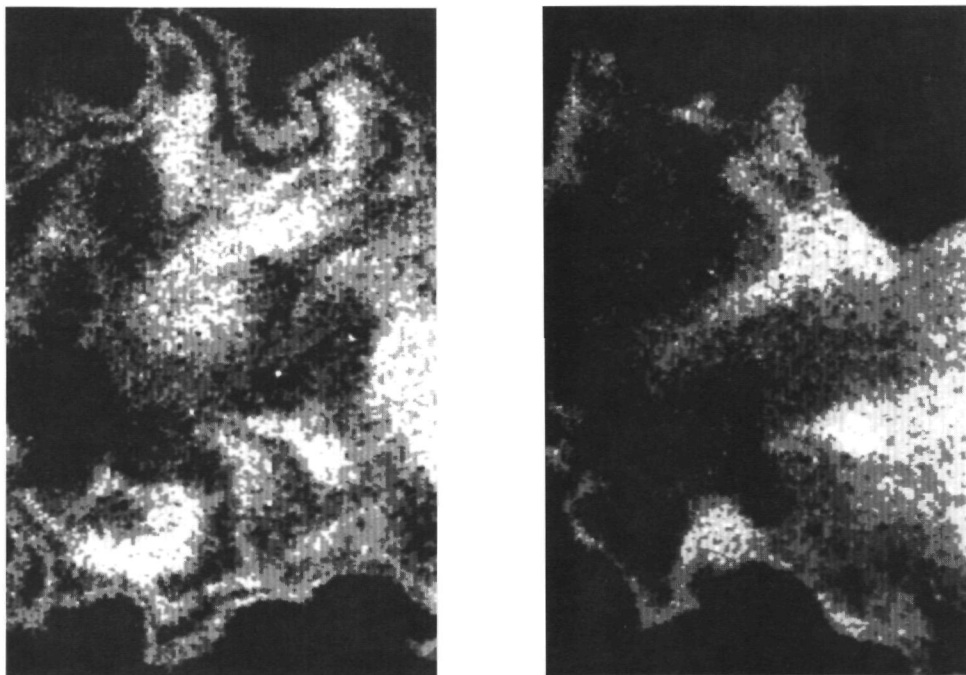


Figure 5.6 : The OH distribution in the 100 kW flame. Left-hand image on the $P_2(8)$ resonance, right-hand image off resonance. The OH radicals are distributed along a small line around the flame. No special filtering is applied to remove the broadband fluorescence of the hydrocarbons

Bunsen burner It will be possible to suppress this emission light to a great extent by applying special fluorescence filtering The right-hand side of figure 5.6 shows a single laser shot spatial distribution while the laser is tuned off the OH resonance The photodissociated hydrocarbon fluorescence remains, while the slim line along the flame front disappears It is important to use a high-quality objective in front of the camera to detect the spatially confined OH fluorescence Using normal lenses the image is blurred and dominated by the emission of the hydrocarbons The flame is extremely turbulent The OH contour can, however, be followed all around the flame at every laser shot The signal-to-noise ratio for OH detection in a single-shot image is approximately 40 Temperature fields can not be measured under such turbulent conditions, unless one has access to two laser systems and two camera systems Even then only moderate information is gained on the temperature distribution in such flames, since only a small area is covered by the OH molecules

NO

The OH signals were strong and easily measured compared with our work in this burner concerning nitric oxide field distributions We encountered problems due to absorption of the 193 nm laser radiation The total integrated absorption of the flame and its surroundings amounts up to 70 percent In air oxygen strongly absorbs due to the $O_2 \text{ B}^3\Sigma_u^-(v'-4) \leftarrow X^3\Sigma_g^-(v''=0)$ transition [75], which gives rise to reduced laser action at five frequencies in the tuning range of the ArF laser The O_2 absorption lines are broadened due to predissociation of the vibrational levels in the $B^3\Sigma_u^-$ state The problem of absorption can be solved by flushing the laser beam path with nitrogen A more serious problem is the absorption of laser radiation in and around the flame and successive disturbing fluorescence due to O_2 resonances starting from the vibrational levels $v''=2$ and 3 in the $X^3\Sigma_g^-$ ground state [18, 75] The hot surroundings of the flame contain vibrationally excited ground state oxygen molecules, especially when the flame is situated in a closed environment From the 50 transitions in NO in the tuning range of the ArF laser the $R_1(26.5)$ and $Q_1(32.5)$, which lie both at a frequency of 51712.5 cm^{-1} [59], can be excited having the smallest effect of the O_2 resonances The transition frequencies and absorption intensities of the vibrationally hot oxygen resonances in the tuning range of the ArF excimer laser have been carefully examined by Lee *et al* [76] The two aforementioned resonances of NO are the resonances we use to measure the NO distribution in the 100 kW flame The use of a 4" diameter fused silica lens turned out to be essential to collect enough photons onto the photocathode of our camera system As a result of this we could increase the thickness of our laser sheet to approximately 5 mm without losing our spatial information With high power densities the fluorescence is saturated, more molecules (in a bigger volume due to a thicker sheet) simply increase the signal level The energy of the ArF laser is 10 mJ per pulse The excitation condition for the fluorescence is therefore linear Excitation spectra measured with our special software option described in section 5.3.1 turned out to be essential too to find the location of

highest NO concentration in the flame. Several areas within the viewing region of the camera were scanned for NO presence. The use of the calibration flame, to check whether the laser is on a NO resonance, was very important because of the enormous additional fluorescence from $O_2(v''=2,3)$ in and around the 100 kW flame.

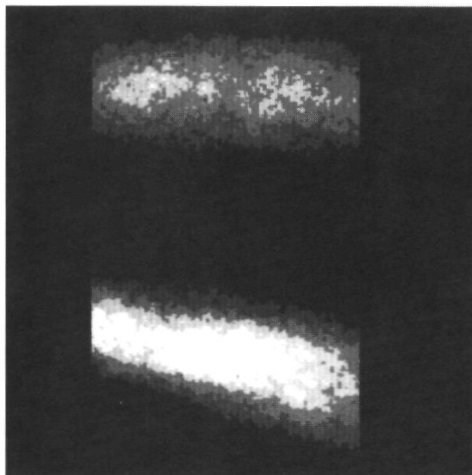


Figure 5.7 : The NO distribution in the 100 kW flame. The laser is tuned to the $R_1(26.5)$ and $Q_1(32.5)$ resonance line of the $D \leftarrow X$ transition. The image is averaged over 100 laser shots. The absorption of the laser radiation (from the bottom to the top) is clearly seen in the figure.

A typical NO field distribution is shown in figure 5.7. The image is averaged over 100 laser shots. The fluorescence is collected from a region as big as 16×14 cm at about 7 cm from the burner head. The absorption of laser radiation is clearly seen in the figure. The image is not corrected for this absorption, since it is almost impossible to determine the exact laser fluence at a given point in the flame. Single shot NO distributions are obtained too. Again the distribution is extremely turbulent. The signal-to-noise ratio for NO detection in a single shot image is 15. The Kolmogorov microscale of turbulence for this flame is calculated to be $400 \mu\text{m}$ [77]. Therefore, with a sheet thickness of 5 mm, the single shot images have lost their structural information concerning the smallest turbulent eddies in the flame. The results give only a qualitative view of the turbulences associated with this flame. From the number of photo-electrons a rough

estimate indicates a NO concentration in the 100 ppm range [29], in accordance with what is expected for these type of furnaces. We have changed the stoichiometry of the flame, which is known to lead to a variation of NO production, while simultaneously monitoring the on-line NO fluorescence in the flame and the NO_x emission in the chimney with a probe. We find a qualitative correlation between the probe data and the NO fluorescence data. Less NO in the flame corresponds to a smaller amount of NO_x emission in the chimney. As a first result of our experiments the design of the burner has been improved. The flame appears more stable and produces a remarkable smaller amount of NO_x, as was checked with the probe. To verify this, however, one would need quantitative NO concentration fields, requiring also instantaneous temperature fields, for the different burner designs and correlated exhaust data, which lie beyond our present experimental possibilities.

5.4 Summary

We have applied the technique of laser-induced fluorescence in a relatively large natural gas flame. Density field distributions of OH and NO have been measured. An attempt to measure temperature fields was unsuccessful due to the turbulent behavior of the flame and due to the small area in which the OH molecules are produced. More general, the OH and NO images show directly that care has to be taken with the interpretation of any type of temperature measurements due to the extreme turbulent character of the flame.

Degenerate four-wave mixing with a tunable excimer laser to detect combustion gases

Michel Versluis and Gerard Meijer

University of Nijmegen, Department of Molecular and Laser Physics
Toernooiveld, NL-6525 ED Nijmegen, the Netherlands

David W. Chandler

Combustion Research Facility, Sandia National Laboratories
Livermore, CA 94550, USA

We report the use of a simple, forward-geometry degenerate four-wave mixing (DFWM-FG) setup to monitor weak absorptions of various gas-phase molecules with a tunable excimer laser. With this technique state-selective detection of H_2 , CO , H_2O and O_2 is demonstrated. The dependence of the DFWM-FG signals on various experimental parameters (e.g. pressure, laser power) is determined. The application of this technique to flames and other combustion environments is discussed.

6.1 Introduction

Degenerate four-wave mixing (DFWM) has been demonstrated as a sensitive technique to monitor gas phase species [78, 79]. The technique has been applied to radicals such as OH and NH where transitions to electronic states are easily accessible. We demonstrate here a DFWM experiment using a tunable excimer laser to state-selectively detect weak gas-phase transitions in H_2 , CO, H_2O and O_2 . The ability to detect all of these species sensitively makes this technique an ideal diagnostic tool for many combustion environments. This technique is one of a host of gas-phase grating experiments that are being developed to measure "background free" gas-phase absorptions. Related grating based techniques have recently been demonstrated by Hayden et al [81] and Zhang et al [82]. Hayden's technique, termed CADLS, uses non-degenerate light pulses and requires multiple resonances in the molecule in order to work. Zhang's technique is also a double-resonant technique where an excitation laser precedes a degenerate four-wave mixing scheme, in order to carry out DFWM from the excited state. These DFWM and grating based techniques complement laser induced fluorescence, direct absorption, and ionization detection schemes. The techniques are quite sensitive and solely rely on the absorption process, the detected molecules do not have to radiate or ionize in order to be detected. Additionally, the signal comes out as a coherent light beam and can be detected in a "zero background" manner in a remote location from the interaction region. Similar techniques have been used to study optical phase conjugation [83, 84] and to detect transient absorptions in liquids [13, 85]. We report here the use of a simple, forward-geometry degenerate four wave mixing (DFWM-FG) setup [86, 87] to monitor weak absorptions of stable molecules in the gas-phase using a tunable excimer laser. In particular we demonstrate the detection of H_2 via the E,F $^1\Sigma_g^+$, $v' \leftarrow X^1\Sigma_g^+$, $v''=0$ two-photon transition and detection of CO via the one-photon spin-forbidden singlet-triplet transition $a^3\Pi(v'=2) \leftarrow X^1\Sigma^+(v''=0)$ detection of O_2 via the $B^3\Sigma_u^-(v'=4) \leftarrow X^3\Sigma_g^-(v''=0)$ (Schumann-Runge band) and detection of H_2O via the two-photon $\tilde{C}^1B_1 \leftarrow \tilde{X}^1A_1$ transition. These spectra demonstrate the sensitivity and utility of using the tunable excimer laser in the DFWM-FG setup to monitor these important combustion species. We have determined the dependencies of the DFWM-FG signals on both the pressure of the probed gas and the pressure of the foreign gas. Laser power dependencies are determined as well.

6.2 DFWM in forward geometry

The theory of degenerate four-wave mixing can be explained both in a non-linear optics picture, in terms of an induced non-linear polarization and the third-order susceptibility tensor $\chi^{(3)}$, or in a dynamic grating picture. Both pictures are being used concurrently [85, 88]. For reasons of clarity, the grating picture will be given here. The experimental evidence for the generation of density gratings, discussed in section 6.4.2, supports the choice of the more elucidating grating picture.

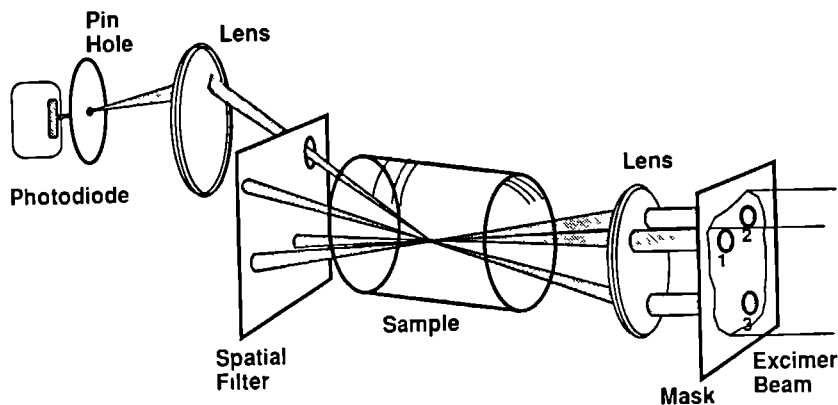


Figure 6.1 Schematic view of the experimental setup for a Degenerate Four-Wave Mixing with Forward Geometry (DFWM-FG) experiment

The degenerate four-wave mixing spectroscopy in forward geometry (DFWM-FG) technique described here is schematically represented in fig. 6.1. A mask is placed in the excimer laser beam, to define three parallel coherent laser beams, located at three corners of a rectangle. The three beams are crossed in a cell containing the sample by focusing through a single lens. If the wavelength of the beams is resonant with an absorption in the gas sample, interference of two of the beams creates a periodically varying spatial distribution of excited molecules, a grating. The grating period λ , equivalent to the grating fringe spacing, is determined by the wavelength λ_p of the coherent laser beams creating the grating and the angle θ between the interfering beams:

$$\lambda = \lambda_p / 2 \sin(\theta/2)$$

A third laser beam of wavelength λ_c , in this case degenerate with the pump beams, focused at the interaction region in the cell, is diffracted off the grating. The diffracted beam comes out of the sample at an angle α at the fourth corner of the rectangle (behind the focus). The diffraction of the probe beam can be described as a Bragg-reflection where the following condition holds:

$$\sin \alpha = m \lambda_c / 2 \lambda = m \sin(\theta/2) \quad \lambda_c / \lambda_p = m \sin(\theta/2) \quad m=1,2.$$

The deflected beam is degenerate in wavelength with the two beams setting up the grating ($\lambda_c = \lambda_p$) and is automatically phase-matched if the holes in the mask are chosen as described.

From the above equations it follows that the the grating can also be probed from an angle of incidence of higher order. This method of probing the grating is required if DFWM-FG is to be applied in a single plane or if DFWM-FG is planned along a line using cylindrical lenses. The reflectivity of the grating is determined by the total number of probed grooves, hence by the combination of the groove spacing and the spatial overlap of the beams. A long focal length lens makes large groove spacings, whereas a short focal length lens creates a small interaction region of the grating-generating beams.

It is important to note that gratings will be set up in the medium by various combinations of the incoming beams. Beams (2) and (3) will set up a grating to which beam (1) is phase-matched and thus part of beam (1) will be deflected through the spatial filter, onto the detector. Similarly, beam (1) and beam (2) will set up a grating off which part of beam (3) will deflect onto the detector, although the diffraction will not be as strong due to the larger angle of incidence. A third grating, set up by beam (1) and (3) is not detected in this geometry. Beam (2) takes part in the creation of both of the gratings that are detected.

6.3 Experimental

In the DFWM-FG experiments described here, a line-narrowed tunable excimer laser (Lambda Physik EMG 150 MSCT) is used as the radiation source. Operating on ArF at 193 nm the linewidth of the laser is about 1.0 cm^{-1} . The laser is tunable from 51600 cm^{-1} to 51850 cm^{-1} . The ArF laser output energy is approximately 50 mJ per pulse and this energy is homogeneously distributed in a 7 mm by 22 mm rectangular shaped beam. Running on KrF at 248 nm, the laser output is approximately 150 mJ, in a 0.5 cm^{-1} line, tunable from 40200 cm^{-1} to 40350 cm^{-1} . The beam dimensions of the KrF excimer laser are almost identical those of the ArF laser. The tunable excimer laser has a tuning range of approximately 1 nm, which is an obvious limitation for doing spectroscopy. This and previous articles show, however, that many important combustion species can be detected using these spectral bright lasers. The laser radiation is coherent enough over the whole beam cross-section that three parallel coherent beams can simply be formed by sending the main laser beam through a mask. The use of unstable resonator optics in the amplifier of the excimer laser is required to keep this coherence. No DFWM-FG signals have been recorded so far with the laser in the amplified oscillator mode [59]. Pulsed dye lasers are known to have rather incoherent properties over their beam cross section. Therefore, with a dye laser, generating and probing a grating in forward geometry can probably only be done efficiently by splitting the dye laser beam (and compensate for the optical path length) with beam splitters and by focussing the splitted beams separately. This again shows an important advantage of the application of tunable excimer lasers in this field of spectroscopy.

The mask, positioned 5 cm behind the amplifier's output coupler, consists of three 2.0 mm diameter holes in an aluminum plate. The holes are located on three corners of a rectangle, with sides of 4.0 and 10.0 mm. The position of the mask in the laser beam is adjusted such that

the energy per pulse of the constructed beams are equal for all the three beams. The energy of the individual laser beams is 1 mJ per pulse at maximum. In some experiments two or three masks are used to prevent straylight from the fundamental excimer laser beam to interfere with the signal beam. The three beams are focussed with a 50 mm diameter, 30 cm focal length lens, passing a quartz window of a stainless steel cell filled at sub-atmospheric pressures, typically between 10 and 300 mbar, with the gases under investigation. The experiments on O_2 and H_2O are partly performed in room air at a pressure of 1 bar. An iris diaphragm behind the cell spatially filters the DFWM-FG signal beam, located at the fourth (dark) corner of the rectangle, from the main laser beams. A lens-pinhole-lens arrangement is set up to minimize straylight effects. A 50 μm pinhole is used in most cases. The signal beam is detected with either a photo diode detector (Lambda Physik LF 302 UV) or with a photomultiplier tube detector (EMI 9635QB). With H_2O in ambient air (typical Dutch humidity) the DFWM-FG signal is intense enough to be traced by eye via its blue fluorescence on a piece of white paper, even with the room lights on! The signal from the photo-detector is fed into a boxcar integrator and the 10 or 30 shots averaged output is displayed on a strip chart recorder. None of the spectra shown here are normalized to laser power.

6.4 Results and Discussions

6.4.1 Molecular spectra

In the upper panel of fig. 6.2 the DFWM-FG spectrum of the spin-forbidden one-photon transition from the $X^1\Sigma^+(v''=0)$ state to the metastable $a^3\Pi(v'=2)$ state in CO is shown. Assignments of all the individual lines in the spectrum, as well as a simulation of the expected linestrengths, is given in reference [20]. A direct comparison of the observed and theoretically expected linestrengths is somewhat difficult. First, a spectral fluctuation in the intensity of the locked, i.e. narrow-band, laser power over the ArF gain profile exists. Around 51790 cm^{-1} , for instance, narrow bandwidth laser operation ceases completely due to an intracavity metastable C-atom absorption [89]. Second, some well known rotational lines in the $v'=4 \leftarrow v''=0$ band of the Schumann-Runge system of O_2 absorb the laser light between the laser head and the detector to a large extent [60]. Nevertheless, a comparison of the DFWM-FG spectrum shown here with the theoretically predicted spectrum for CO at 300 K [20] shows a more or less linear correspondence between observed and calculated line intensities. The CO spectrum shown here has been recorded with 300 mbar of CO in the cell, but even with the photo diode detector CO spectra could be measured at pressures down to 10 mbar.

In the lower panel of fig. 6.2 the DFWM-FG spectrum of the two-photon $E,F^1\Sigma_g^+, v' \leftarrow X^1\Sigma_g^+(v''=0)$ transition in 50 mbar of H_2 is shown. The four lowest Q-branch transitions to the $v'=6$ level, as well as the Q(2) transition to the $v'=7$ level, lie within the tuning range of the ArF laser [90, 91, 39]. Some non-resonant signal is visible in the spectrum, possibly produced

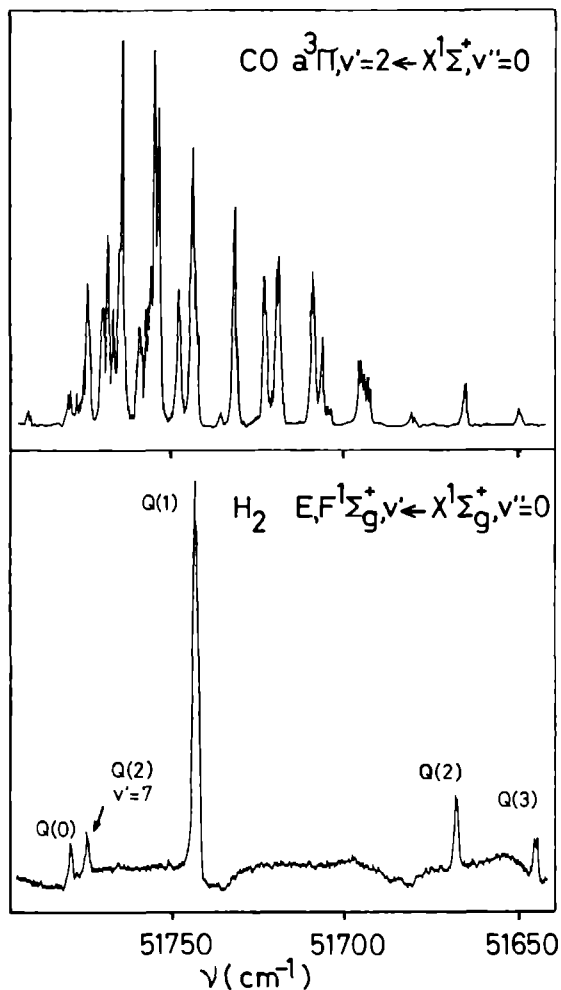


Figure 6.2 DFWM-FG spectra of the spin-forbidden $a^3\Pi(v'=2) \leftarrow X^1\Sigma^+(v''=0)$ transition in 300 mbar CO (upper) and of the two-photon $E, F^1\Sigma_g^+(v'=6,7) \leftarrow X^1\Sigma_g^+(v''=0)$ transition in 50 mbar H_2 (lower), measured with a tunable ArF excimer laser

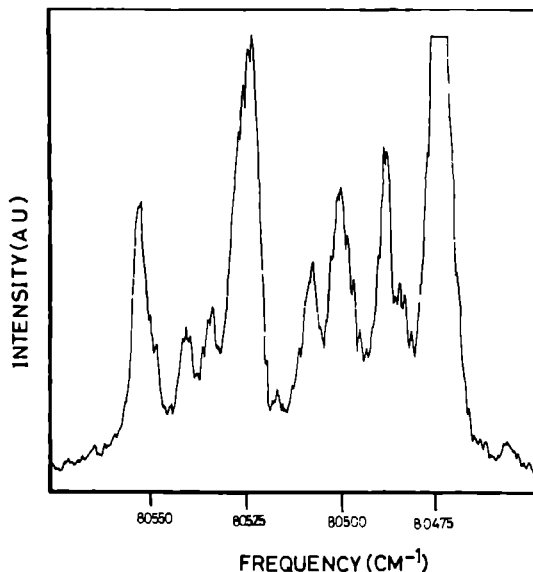


Figure 6.3 DFWM FG spectrum of the $\text{H}_2\text{O } \tilde{\text{C}}^1\text{B}_1 \leftarrow \text{A}^1\text{A}_1$ transition in ambient air taken with a tunable KrF excimer laser. The peaks are all assigned in ref [16]

by a three-photon direct ionization ion grating. The dips in this broad signal are due to the aforementioned O_2 resonances absorbing the laser light on its way to the detector. Identical spectra to the one shown here have been obtained using either (2+1)-REMPI with total ion current detection [90] or two-photon excited LIF [91]. For H_2 a second order deflection is also visible, even at a pressure of 50 mbar. The H_2 spectrum measured via this second order deflection shows more non-linear line intensities however. It is interesting to note that only beam (1) is deflected in second order. The physical origin of the second order deflected beam is still unclear to us.

We have obtained molecular spectra of O_2 and H_2O by focussing the three excimer laser beams in room air. The O_2 DFWM-FG signal is obtained by focusing the 193 nm ArF excimer laser beam in air. The predissociative $\text{B}^3\Sigma_u^-(v'=4) \leftarrow \text{X}^3\Sigma_g^-(v''=0)$ (Schumann-Runge band) transitions of O_2 [60] are detected. The line intensities in the observed spectrum are somewhat distorted as much of the laser light (including the signal beam) is absorbed on the oxygen resonances by O_2 in the beam path. Superimposed on the broad $\text{B} \leftarrow \text{X}$ O_2 transitions, unassigned sharp transitions of either O_2 or O_2^+ are observed. These resonances have also been observed

using laser induced fluorescence [36, 23]

Fig 6 3 shows the spectrum obtained when the KrF (248 nm) excimer laser is scanned over the $\text{H}_2\text{O } \tilde{\text{C}}^1\text{B}_1 \leftarrow \tilde{\text{X}}^1\text{A}_1$ transition This transition has been observed before using (2+1)-REMPI [16] as well as using two-photon excited fluorescence [28], and the individual rotational transitions have been assigned In reference [16] the photo-dynamics of the predissociation, ionization and fluorescence processes have been determined The OH photo-product spectra are clearly very different from our DFWM-FG spectra The spectrum we observe is nearly identical to the aforementioned (2+1)-REMPI spectrum and the parent molecular fluorescence excitation spectra This leads us to conclude that the grating probed in this experiment is a density grating, detectable through the difference in the total number of electronically excited H_2O molecules and/or H_2O^+ ions The probed grating is clearly not composed of regular population differences of the OH photo-products nor is it composed of differences in the total number of ground-state water molecules

6.4.2 DFWM-FG pressure dependence

In order to quantify the origin of the observed four-wave mixing processes the pressure dependencies of the DFWM-FG signals are determined Fig 6 4 shows the pressure dependence of the four-wave mixing signal of pure H_2 The pressure in the cell is varied between 10 and 200 mbar The curve in fig 6 4 corresponds to a cubic pressure dependence and it fits the data remarkably well The experiment is repeated for pure CO and also a cubic pressure dependence is found In the CO experiment the pressure is varied from 20 to 550 mbar

To check the influence of the background pressure on the signal, the cell is filled with 50 mbar of H_2 Helium is added as a foreign gas and the total pressure is varied whilst monitoring the DFWM-FG signal The measured dependence is shown in fig 6 5, where a clear linear behavior is observed, indicating the presence of a collision induced density grating The line does not fit to the lowest pressure data point, since in fact the total number of collisions should be plotted on the horizontal axis The aforementioned data point needs a correction since only $\text{H}_2\text{-H}_2$ collisions are relevant here The data point has not been included in the fit From the two experiments above we can conclude that a density grating is generated by the two pump beams and by successive collisions in the sample More collisions generate a better defined grating In addition, the DFWM signal grows quadratically with the density of the probed molecule, as is the case in every four wave mixing process like DFWM and CARS One should be aware of the fact that DFWM-FG is different from earlier DFWM experiments, since it is not a $t = 0$ type of experiment Collisions are needed to generate a proper grating

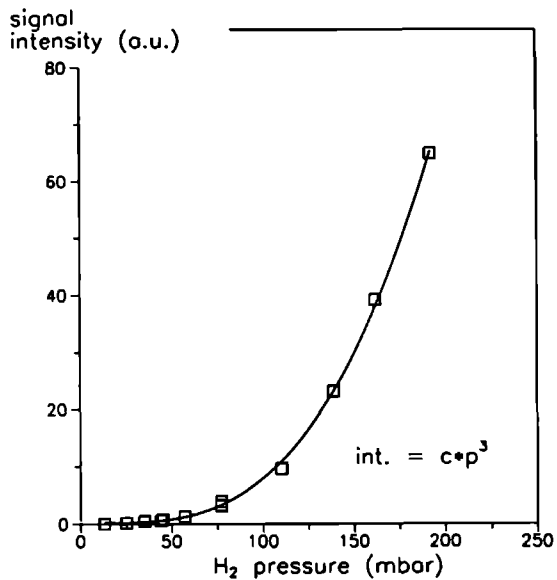
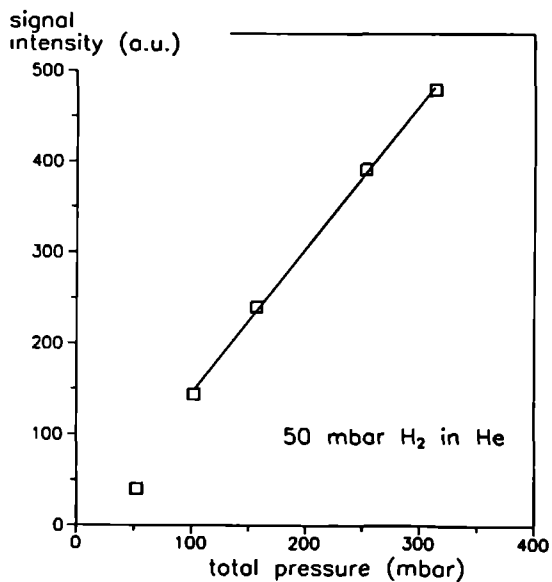


Figure 6.1 The H₂ pressure dependence of the DIWM-FG signal. A smooth cubic dependence is found.

Figure 6.5 The pressure dependence of the DIWM-FG signal if He added as a foreign gas. A linear dependence is found.



The fact that the DFWM-FG signal increases with pressure makes the technique complementary to existing diagnostic techniques, such as LIF and REMPI, which work better at lower pressures due to collisional quenching of the fluorescence the reduction of the mean free path of the electrons and ions at atmospheric pressures, respectively

6.4.3 DFWM-FG laser power dependence

Curious enough, the intensity patterns observed for the two-photon absorption in H_2 and H_2O appear to have very similar relative intensities compared with the $(2+1)$ -resonance enhanced multi-photon ionization (REMPI) spectra of the same transitions. The spin-forbidden one-photon transition in CO has approximately the intensity of the calculated transition strengths. We measured the DFWM-FG signal dependence on the total laser power and found a linear dependence over one order of magnitude, which is in agreement with the aforementioned similarities

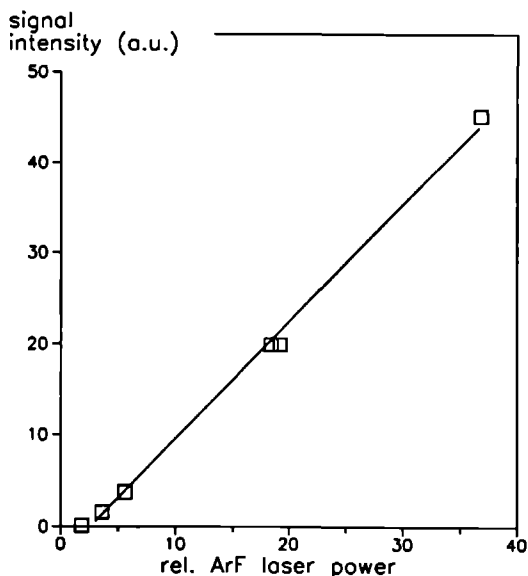


Figure 6.6 The laser power dependence of the DFWM-FG signal. The power of the three beams are attenuated simultaneously.

The dissociation of the molecule, either through predissociation of the resonant state or by further absorption of photons creates a larger density of species at the parts of the grating where a constructive interference between the laser beams exists than at those parts exhibiting a

destructive interference. This grating is then proportional to the transition strength of the weak first step and we obtain spectra that have well behaved linear spectral intensity patterns

6.4.4 Application to combustion environments

Earlier degenerate four-wave mixing experiments [78, 79] show the applicability of the DFWM technique in flames and combustion environments. These experiments were done using the backward geometry detection scheme. Phase-conjugate mirrors can then be used to maintain the coherence properties of the grating-generating beams, even in turbulent environments. Our forward-geometry detection scheme does not possess this phase-conjugate property. Recent experiments by Fourkas et al. [92] have shown that transient grating experiments in flames can be performed with an experimental geometry similar to the one we use.

6.5 Summary

We have shown here that the DFWM-FG technique can be used to detect local densities of H_2 , CO, H_2O and O_2 . This work complements work by others on the detection of radicals using similar techniques. We have determined the pressure and power dependencies of the DFWM-FG signals. We conclude that the grating we form are density gratings, formed after collisions. The DFWM-FG technique works better at higher pressures, which makes this single laser technique complementary to existing diagnostic tools.

Future outlook

Laser-based spectroscopic techniques now cover a fast growing field of applications not only in specific areas of combustion diagnostics, but also in atmospheric environmental sensing and wind tunnel experiments, for example. The tunable excimer laser proves to be a suitable piece of equipment and Rayleigh scattering, laser-induced fluorescence and degenerate four-wave mixing in forward geometry are relatively straightforward techniques used with it. Many aspects need further investigation. For instance, the origin of the presumed O_2^+ spectra, appearing every time when sharp focussing in flames is applied and complicating other spectroscopy. Effort has to be directed to find ways to quantitatively measure state distributions of specific molecules. For instance, will fluorescence depletion by ionization be a way to perform quantitative measurements?

A large field of unexplored spectroscopic information awaits discovery. Can intermediate combustion species, such as CH_2 , CH_3 and C_2H , be traced in a flame efficiently? We have always detected fluorescence of intermediates near the flame front, but apart from the fact that their absorption is rather broadband little spectroscopic information is yet gathered from these species.

New and faster camera techniques will certainly help to clarify aspects of molecular spectroscopic research. The developments of camera techniques and image processing units are very fast. 18-bits cameras are commonly used in imaging and spectroscopy. In our setup the image intensifiers are still the limiting factor because of their 10-bits, at maximum, resolution. Image processing gives the possibility of very fast data acquisition with 50 MHz Intel 486-based systems. Digitally recorded images grabbed in a memory frame of the computer can be actively supplemented with numerous experimental information, such as the dispersive spectroscopic data of the image grabbed or information on the pressure in the cell or internal combustion engine. Optical multichannel analyzers (OMA's) reduce the experimental measuring time to the duration of a single laser scan. The dispersed fluorescence of the molecules under investigation is recorded after every laser shot and stored in a row of the frame buffer of the image processing

board. The spectroscopic information of dispersion spectra (in the rows) or excitation spectra (in the columns) can now be analyzed by special software. The simultaneous measurement of excitation and dispersion spectra gives much more insight in the spectroscopy of the molecules, as many information is undetected in the conventional setup. Some fundamental problems are still to be solved. In section 2.4 we have discussed the problems of rotational level dependent predissociation of the hydroxyl radical in respect to quantitative measurements of densities and temperatures.

Combustion diagnostics using laser-based techniques has, and will have, many applications in the near future. We have measured the OH and NO field distributions in a large natural gas flame and more detailed experiments in this direction will follow. The interaction between flames and surfaces, for instance diamond deposition with C_2H_2 /air welding torches, is now investigated. Turbulent combustion processes in both petrol and diesel-fired internal combustion engines is studied. As a net effect, we believe the laser-based molecular spectroscopic techniques will help to understand the complex chemical physics of combustion processes and, as a result of this, it will contribute to the reduction of excessive fuel consumption and to a cleaner and more healthy environment.

References

- [1] P Andresen, G Meijer, H Schluter, H Voges A Koch, W Hentschel W Oppermann and E Rothe
Appl Opt 29, 2392 (1990)
- [2] A G Gaydon
The spectroscopy of flames, 182
(Chapman & Hall, London) (1974)
- [3] A G Gaydon and H G Wolfhart
Flames, their structure, radiation and temperature, 239
(Chapman & Hall, London) (1970)
- C TH J Alkemade, Tj Hollander, W Snelleman, and P J Th Zeegers,
Metal vapours in flames, 315
(Pergamon Press Oxford) (1982)
- [4] A Koch
Ph D Thesis, Georg August University Gottingen (1992) (in German)
- [5] J A Shirley
Appl Phys B 51, 45 (1991)
- [6] T S Cheng, J A Wehrmeyer and R W Pitz
NASA contractor report no 189544 (1991)
- [7] A C Eckbreth
Laser diagnostics for combustion temperature and species
(Abacus, Cambridge, Mass) (1988)

- [8] T Dreier and J Wolfrum
J Chem Phys **80**, 957 (1984)
- [9] A C Eckbreth and T J Anderson
SPIE **742** Laser Applications to Chemical Dynamics, 34 (1987)
- [10] C R Vidal
in *Topics in applied physics* **59**, *Tunable lasers*
ed L F Mollenauer and J C White
Springer, Berlin p 57 (1987)
- [11] D J Rakestraw, private communication
- [12] G Meijer and D W Chandler
Chem Phys Lett **192**, 1 (1992)
- [13] M D Fayer
Ann Rev Phys Chem **33**, 63 (1982)
- [14] G Laufer and R L McKenzie
AIAA-88-4679-CP AIAA/NASA/AFWAL Conference on Sensors and Measurements for
Aeronautical Applications, Atlanta (September 7-9, 1988)
- [15] E W Rothe, G S Ondrey and P Andresen
Opt Commun **58**, 113 (1986)
- [16] G Meijer, J J ter Meulen, P Andresen and A Bath
J Chem Phys **85**, 6914 (1986)
- [17] P Andresen, A Bath, W Groger H Lulf, G Meijer and J J ter Meulen
Appl Opt **27**, 365 (1988)
- [18] A M Wodtke, L Huwel, H Schluter H Voges, G Meijer and P Andresen
J Chem Phys **89**, 1929 (1988)
- [19] A M Wodtke L Huwel, H Schluter G Meijer, P Andresen and H Voges
Opt Lett **13**, 910 (1988)
- [20] G Meijer, A M Wodtke, H Voges, H Schluter and P Andresen
J Chem Phys **89**, 2588 (1988)
- [21] M Ebben, M Versluis and J J ter Meulen
J Mol Spectrosc **149**, 329 (1991)

-
- [22] X Yang, C A Rogaski and A M Wodtke
J Opt Soc Am B 7, 1835 (1990)
- [23] The excitation spectra of O₂ or O₂⁺ resonances have been observed using laser-induced fluorescence with a tunable excimer laser at 193 nm M Versluis, R Klein-Douwel, A Koch and G Meijer (unpublished)
- [24] R Suntz, H Becker, P Monkhouse and J Wolfrum
Appl Phys B 47, 287 (1988)
- [25] W Ketterle M Schafer, A Arnold and J Wolfrum
Appl Phys B 54, 109 (1992)
- [26] D C Robie, J D Buck and W K Bischel
Appl Opt 29, 3961 (1990)
- [27] G S Kim, L M Hitchcock, E W Rothe and G P Reck
Appl Phys B 53, 180 (1991)
- [28] A Hodgson, J P Simons, M N R Ashfold, J M Bayley and R N Dixon
Mol Phys 54, 35 (1985)
- [29] M Boogaarts
Internal report Dept of Molecular and Laser Physics
University of Nijmegen (1991) (in Dutch)
- [30] H Schluter
Internal report Dept of Atomic Physics
Max Planck Institut for Flow Research Gottingen (1990) (in German)
- [31] R Klein-Douwel
Internal report Dept of Molecular and Laser Physics
University of Nijmegen (1992)
- [32] L P H de Goey and H C de Lange
Internal report Dept of Mechanical Engineering
Technical University Eindhoven, the Netherlands (1989)
- [33] R Quax
Internal report Dept of Mechanical Engineering
Technical University Eindhoven, the Netherlands (1992) (in Dutch)

- [34] H. Lefebvre-Brion and R W. Field
Perturbations in the spectra of diatomic molecules
(Academic,Orlando) (1986)
- [35] H Voges, private communication
- [36] G Laufer, R L. McKenzie and W M. Huo
Opt. Lett. **13**, 99 (1988)
- [37] J.M. Seitzman, J Haumann and R K Hanson
Appl Opt. **14**, 2892 (1987)
- [38] G. Meijer
Ph.D. Thesis, University of Nijmegen (1988)
- [39] D.J. Kliger and C K Rhodes
Phys Rev Lett **40**, 309 (1978)
- [40] M L Sink, A.D Bandrauk and R. Lefebvre
J. Chem Phys **73**, 4451 (1980)
- [41] J.A. Gray and R L Farrow
J. Chem Phys **95**, 7054 (1991)
- [42] D E. Heard, D.R. Crosley, J B Jeffries, G P Smith, and A. Hirano
J. Chem. Phys. **96**, 4366 (1992)
- [43] G.H. Diecke and H M Crosswhite
J. Quant Spectrosc Radiat Transfer **2**, 97 (1962)
- [44] R.A. Copeland, J B Jeffries and D R Crosley
J Mol Spectrosc **143**, 183 (1990)
- [45] M Versluis, M. Boogaarts, R Klein-Douwel, B. Thus, W de Jongh, A Braam
J J. ter Meulen, W L. Meerts and G Meijer
Appl Phys B **55** (1992)
- [46] M. Versluis, G Meijer and D W. Chandler
submitted
- [47] A. Chryssostomou, H Voges, W Reckers, P Andresen
P. Krogmann, K A Butefisch and H. Wolfrum
Two dimensional Laser Diagnostic Experiments at the RWG wind tunnel, DLR Göttingen,
Laser Laboratorium Göttingen Report 1/340/1990

-
- [48] H. Rottke and H. Zacharias
J. Chem. Phys. **83**, 4831 (1985)
- [49] S Gerstenkorn and P. Luc
Atlas du spectroscopie d'absorption de la molecule d'iode (Centre National de la Reserche Scientifique) (1978)
- S. Gerstenkorn and P. Luc
Rev. Phys. Appl. **14**, 791 (1979)
- [50] J.V. Foltz, D H Rank and T A. Wiggins
J Mol Spectrosc **21**, 203 (1966)
- [51] C Amiot and J. Verges
Chem. Phys. Lett **66**, 570 (1979)
- [52] C. Amiot and J Verges
Phys. Scripta **26**, 422 (1982)
- [53] A. Hinz, J S. Wells and A G Maki
J Mol. Spectrosc **119**, 120 (1986)
- [54] J. Bokor, J Zavelovich, and C K Rhodes
J. Chem Phys. **72**, 965 (1980)
- [55] R C. Sausa, A.J Alfano and A W Miziolek
Appl. Optics **26**, 3588 (1987)
- [56] W.T. Hill III, B P Turner, H Lefebvre-Brion, S Yang, and J Zhu
J. Chem Phys **92**, 4272 (1990)
- [57] C.N. Merrow, and B E Forch
J. Chem. Phys **93**, 4791 (1990)
- [58] B.E. Forch, and C N Merrow
J. Chem Phys **95**, 3252 (1991)
- [59] M Versluis, M Ebben, M Drabbels, and J J ter Meulen
Appl. Opt. **30**, 5229 (1991)
- [60] D.M. Creek and R W Nicholls
Proc. R. Soc Lond. A **341**, 517 (1975)
- [61] M. Shimauchi, T Miura, and S Karasawa
J Chem Phys **71**, 3538 (1979)

- [62] Ed R C Weast, and M J Astle,
Handbook of Chemistry and Physics, E-355
60th edition (1980)
- [63] I Glassman
Combustion
(Academic Press, London 1987), p 318
- M L Elder and J D Wineforder
Proc Analyt Atom Spectrosc 6, 292 (1983)
- [64] T Dreier and D J Rakestraw
Opt Lett 15, 71 (1990)
- [65] P Ewart and M Kaczmarek
Appl Opt 30, 3996 (1991)
- [66] M B Long, B F Weber R K Chang
Appl Phys Lett 34 22 (1979)
- R Miles and W Lempert
Appl Phys B 51, 1 (1990)
- [67] The Dutch National Environmental Policy Plan, Part II
National Institute for Public Health and Environmental Protection (RIVM)(1990)
- [68] A Braam H Hulshof W de Jongh, and B Thus
Proceedings of the First Conference on Combustion and Environment
(Vilamoura, Portugal) 19 (1991)
- [69] R K Hanson, J M Seitzman, and P H Paul
Appl Phys B 50, 441 (1990)
- [70] An overview of recent LIF applications is found in *Appl Phys B* 50(6) (1990) and
Appl Phys B 51(1) (1990)
- [71] A Koch, A Chrysostomou, P Andresen and W Bornscheuer
(submitted 1991)
- [72] Gasunie, the Netherlands private communication
- [73] D Mormile
*Proceedings of the EPA and EPRI Symposium on
Stationary Combustion NO_x-control*
(New Orleans) Ch 42, 1 (1987)

-
- [74] A G Gaydon
The spectroscopy of flames, 159
2nd ed (Chapman & Hall, London) (1974)
- [75] K Yoshino, D E Freeman, and W H Parkinson
J Phys Chem Ref Data **13**, 207 (1984)
- [76] M P Lee and R K Hanson
J Quant Spectrosc Radiat Transfer **36**, 425 (1986)
- [77] H Tennekes and J L Lumley
First course in turbulence
3d ed (Mass Institute of Technology Boston) (1974)
- [78] P Ewart and S V O'Leary
Opt Lett **11**, 279 (1986)
- [79] T Dreier and D J Rakestraw
Appl Phys B **50**, 479 (1990)
- [80] D J Rakestraw, R L Farrow and T Dreier
Opt Lett **15**, 709 (1990)
- [81] M A Buntine, D W Chandler and C Hayden
J Chem Phys **97**, 707 (1992)
- [82] Q Zhang, S A Kandel, T A W Wasserman and P H Vaccaro
J Chem Phys **96**, 1640 (1992)
- [83] R A Fisher, Ed
Optical Phase Conjugation
(Academic, New York) (1983)
- [84] D M Pepper
Opt Eng **21**, 155 (1982)
- [85] H J Eichler, D Pohl and P Gunter
Laser Induced Dynamic Gratings
Springer Series in Optical Sciences, **50**, (1986)
- [86] G M Carter
J Opt Soc Am B **4**, 1018 (1987)

- [87] W Du, X Zhang, K Chen, Z Lu, Y Zheng and J Wu
Opt Comm 84, 205 (1991)
- [88] Y R Shen
IEEE J Quant Electr QE-22, 1196 (1986)
- [89] M Versluis and G Meijer
J Chem Phys 96, 3350 (1992)
- [90] L M Hitchcock, G S Kim, E W Rothe and G P Reck
Appl Phys B 52, 27 (1991)
- [91] T Okada, M Maeda, Y Kajiki, K Muraoka and M Akazaki
Appl Phys B 43, 113 (1987)
- [92] J T Fourkas, T R Brewer, H Kim and M D Fayer
J Chem Phys 95, 5775 (1991)

Samenvatting

Diagnostiek aan verbrandingsprocessen bij atmosferische drukken met behulp van een afstembare excimeer laser

Dit proefschrift beschrijft de experimenten aan verbrandingsprocessen bij atmosferische drukken gebruikmakend van een afstembare excimeer laser opererend in het diepe UV. Moleculaire dichtheids- en vlamtemperatuursverdelingen worden twee dimensionaal zichtbaar gemaakt door gebruik te maken van laser geïnduceerde fluorescentie (LIF) van vlamradicalen en -moleculen. De spectraal heldere ArF of KrF excimeer laser bundel wordt omgevormd tot een laserlint, welke vervolgens door de te onderzoeken vlam snijdt. Daar waar de moleculen de laser-fotonen absorberen ontstaat fluorescentielicht dat op UV gevoelige elektronische videocamera's afgebeeld wordt. Zo kan een film gemaakt worden van de moleculaire dichtheidsverdeling van bijvoorbeeld stikstofdioxide (NO₂), een veroorzaker van zure regen, in de vlam. Naast de LIF techniek beschrijft dit proefschrift ook andere diagnostische technieken om verbrandingsprocessen te bestuderen. De opbouw en onderdelen van het experiment, zoals de laser en de camera, worden in detail beschreven. Een overzicht van de spectroscopie van moleculen in verbrandingsprocessen wordt gegeven. Een nieuwe techniek in verbrandingsonderzoek, degeneratieve four-wave mixing, wordt toegepast op verschillende moleculen die in vlammen voorkomen. De afstembare excimeer laser, zes jaar geleden commercieel geïntroduceerd, is in detail bestudeerd en verbeterd. Het inleidende hoofdstuk 1 beschrijft diagnostische technieken in verbrandingsonderzoek, variërend van thermokoppels tot geavanceerde lasertechnieken. Rayleigh en Raman verstrooiing worden beschreven en niet-lineaire optische processen zoals Degeneratieve Four-Wave Mixing (DFWM) en Coherent Anti-Stokes Raman Scattering (CARS) worden kort behandeld. In detail is gekeken naar laser geïnduceerde fluorescentie en de implicaties bij het meten bij atmosferische drukken. De methode van laser geïnduceerde predissociatieve fluorescentie (LIPF) om kwantitatief temperaturen en dichtheden te meten wordt verduidelijkt. In hoofdstuk 2 wordt de experimentele opstelling in detail beschreven. Hier vinden we gegevens over de afstembare excimeer laser en wordt de speciaal geconstrueerde camera en het bijbehorende beeldverwerkingssysteem beschreven. Een deel van dit hoofdstuk is gewijd aan de spectroscopie van vlamradicalen en moleculen gemeten met behulp van een afstembare excimeer laser. Hoofdstuk 2 wordt afgesloten met een beschrijving van het meten van vlamtemperaturen gebruikmakend van de LIPF meetmethode en de daaraan verbonden experimentele voorwaarden. Hoofdstuk 3 beschrijft de spectroscopie van het NO radicaal met een afstembare ArF excimeer

laser bij een golflengte van 193 nm. Gebruikmakend van deze informatie is het afstemgebied van de laser gecalibreerd. Absolute lijnposities van de $B \leftarrow X$ en $D \leftarrow X$ overgang worden gegeven. Een intra-cavity absorptie ten gevolge van metastabiele C atomen is gevonden in het afstemgebied van de ArF laser. De laser vertoont geen laserwerking over een gebied van 5 tot 10 cm^{-1} , afhankelijk van de kwaliteit van het gasmengsel in de ontlading. Het gebrek aan laserwerking in dit gebied heeft een direct gevolg voor de interpretatie van fotodissociatie experimenten van CO. Dit wordt kort beschreven in hoofdstuk 4.

Zijn de vorige hoofdstukken vrij fundamenteel van aard, in hoofdstuk 5 wordt een directe toepassing van de meetmethode gedemonstreerd. Hier wordt een grootschalig experiment beschreven aan een 100 kW aardgasvlam. De vlam is een geschaald model van een 10 MW vlam uit een kolengestookte energiecentrale. We hebben single-shot OH en NO dichtheidsverdelingen gemeten in gebieden van 20 bij 20 cm. Laserlicht absorptieproblemen zijn opgelost door de kennis van de fundamentele spectroscopie van het NO radicaal.

In hoofdstuk 6 wordt degenerate four-wave mixing in voorwaartse richting beschreven. In een relatief eenvoudige opstelling is zeer gevoelig aan zwakke twee-foton of spin-verboden overgangen van o.a. H_2 en CO gemeten. Met deze nieuwe meetmethode verrichten we absorptiespectroscopie tegen nul achtergrond. De signalen zijn sterk genoeg om met fotodioden te worden gemeten.

Hoofdstuk 7, tenslotte, beschrijft in het kort wat de toekomst mogelijk brengen zal. Met name op het gebied van de beeldverwerking verwachten we veel nieuwe en snellere systemen, die data acquisitie nog eenvoudiger zullen maken.

Curriculum Vitae

Andreas Michael Versluis

Op 6 september 1963 ben ik geboren in Amstelveen in de toenmalige gemeente Nieuwer Amstel. Na een verblijf van een jaar in Azrou, Marokko verhuisde ik op vier-jarige leeftijd naar Denpasar, Bali, Indonesië. Met goed gevolg doorliep ik de Sekolah Dasar op de C.I.P. school. Ook behaalde ik, begeleid door mijn moeder, het I.V.I.O. diploma. In de zomer van 1975 keerden we terug naar Nederland. Het brugklasjaar van de middelbare school doorliep ik op het Visser 't Hooft College te Leiden, waarna een verhuizing naar de Achterhoek volgde. Het VWO diploma haalde ik vijf jaar later op het St. Ludgercollege te Doetinchem.

In augustus 1981 startte ik de studie Natuurkunde aan de Katholieke Universiteit Nijmegen. Ik behaalde het kandidaats examen Natuurkunde en ook het kandidaats-examen Sterrenkunde in september 1985. In juli 1988 sloot ik mijn academische opleiding af met het doctoraal examen Natuurkunde met groot bijvak Astrofysica. Als student heb ik anderhalf jaar bij het college Sterrenkunde geassisteerd. Mijn afstudeer onderzoek verrichtte ik op de afdeling Molecuul- en Laserfysica van de Katholieke Universiteit Nijmegen en deels in samenwerking met de Stichting Ruimteonderzoek Nederland (SRON) te Groningen.

Aansluitend startte ik mijn promotie-onderzoek op de afdeling Molecuul- en Laserfysica aan de Katholieke Universiteit Nijmegen onder leiding van Prof. Jorg Reuss. Tijdens deze periode heb ik gedurende anderhalf jaar het Basiscolloquium en gedurende een jaar het Sterrenkunde college mede begeleid. Voor het onderzoek verbleef ik vaak op de afdeling van Prof. Peter Andresen op het Max Planck Institut für Stromungsforschung te Göttingen, Duitsland. Op 28 september 1992 hoop ik op dit proefschrift te promoveren.

Als duidelijk bewijs van mijn al levenslange drang tot reizen start ik in oktober 1992 een post-doc positie in de groep van Prof. Alan Knight op de Griffith Universiteit te Brisbane, Australië.

Publications

- Far infrared laser sideband spectroscopy of H_3O^+ the pure inversion spectrum around 55 cm^{-1}
P Verhoeve, M Versluis, J J ter Meulen, W L Meerts and A Dymanus
Chemical Physics Letters **161**, 195-201 (1989)
- A far infrared laser sideband spectrometer in the frequency region 550 - 2700 GHz
P Verhoeve, E Zwart, M Versluis, M Drabbels, J J ter Meulen, W L Meerts, A Dymanus and D B McLay
Review of Scientific Instruments **61**, 1612-1625 (1990)
- Frequency calibration in the ArF excimer laser tuning range using laser-induced fluorescence of NO
M Versluis, M Ebben, M Drabbels and J J ter Meulen
Applied Optics **30**, 5229-5234 (1991)
- The laser-induced fluorescence spectrum of SiF around 193 nm
M Ebben, M Versluis and J J ter Meulen
Journal of Molecular Spectroscopy **149**, 329-340 (1991)
- Verkennde LIF metingen aan een keramische brander met een afstembare ArF excimeer laser
M Versluis, G Meijer, W L Meerts, J J ter Meulen and J Hoornstra
Energie Onderzoek Centrum Nederland, Rapport ECN-I-91-061 (1991)
- Intra-cavity C atom absorption in the ArF excimer laser tuning range
M Versluis and G Meijer
Journal of Chemical Physics **96**, 3350-3351 (1992)

- Degenerate four-wave mixing with a tunable excimer laser to detect combustion gases
M Versluis, G Meijer and D W Chandler
submitted
- Laser-induced fluorescence imaging in a 100 kW natural gas flame
M Versluis, M Boogaarts, R Klein-Douwel, B Thus, W de Jongh, A Braam,
J J ter Meulen, W L Meerts and G Meijer
Applied Physics B (in press)

